



**Politecnico  
di Torino**

**MASTER DEGREE IN  
MECHANICAL ENGINEERING**

A.Y. 2020/2021

**Thesis**

Thermo-structural analysis and life-time evaluation of an  
heavy duty gas turbine rotor

**SUPERVISOR**

Prof. Daniela Misul

**CO-SUPERVISOR**

Prof. Simone Salvadori

Prof. Mirko Baratta

**Candidate**

Andrea Guarnieri

S267150

# Contents

<b>Abstract</b>	<b>1</b>
<b>Introduction</b>	<b>3</b>
<b>1 Heavy Duty Gas Turbines</b>	<b>5</b>
1.1 Introduction . . . . .	5
1.2 Brayton-Joule cycle . . . . .	6
1.2.1 Performances . . . . .	9
1.3 Thermo-Structural analysis fundamentals . . . . .	11
1.3.1 Plane Stress theory of Axisymmetric bodies . . . . .	11
1.3.2 Heat Transfer Theory . . . . .	14
1.3.3 Low Cycle Fatigue Analysis . . . . .	20
1.4 Fundamentals of FEM . . . . .	24
<b>2 Rotor Description</b>	<b>30</b>
2.1 Summary . . . . .	30
2.2 Compressor . . . . .	32
2.3 Turbine . . . . .	35
2.3.1 Cooling flow . . . . .	37

---

<b>3</b>	<b>Steady-State FEM Analysis</b>	<b>40</b>
3.1	Introduction . . . . .	40
3.2	2D model Analysis Setup . . . . .	41
3.2.1	Geometry validation and material properties characterization .	41
3.2.2	Meshing and connection control . . . . .	45
3.2.3	Mechanical and Thermal Boundary conditions . . . . .	47
3.3	Analysis results . . . . .	60
3.3.1	2D model entire rotor output . . . . .	60
3.3.2	2D Vs. 3D stress comparison on TWs WEB . . . . .	63
3.3.3	Turbine side . . . . .	70
3.3.4	Classification of stresses . . . . .	77
3.3.5	Neuber's rule . . . . .	79
3.4	Static structural verification . . . . .	81
3.4.1	Design criteria curves . . . . .	81
3.4.2	Post-processing results . . . . .	83
<b>4</b>	<b>Transient FEM Analysis</b>	<b>90</b>
4.1	Introduction . . . . .	90
4.2	Boundary conditions . . . . .	91
4.2.1	Mechanical . . . . .	93
4.2.2	Thermal . . . . .	95
4.3	Temperature map . . . . .	98
4.4	LCF analysis . . . . .	100
4.4.1	Notch sensitivity . . . . .	100
4.4.2	Compressor side . . . . .	101

4.4.3	Turbine side . . . . .	108
<b>5</b>	<b>Grammel's method</b>	<b>114</b>
5.1	Introduction . . . . .	114
5.2	Constant thickness solution . . . . .	115
5.3	The method and its implementation . . . . .	118
5.3.1	Procedure . . . . .	120
5.3.2	Inputs . . . . .	122
5.3.3	Versatility . . . . .	123
5.4	Design concept of rotating disks and FEM validation . . . . .	124
5.5	Limitations of the method . . . . .	129
<b>6</b>	<b>Conclusions and future developments</b>	<b>134</b>
	<b>Annex</b>	<b>137</b>
	<b>List of Figures</b>	<b>140</b>
	<b>Bibliography</b>	<b>144</b>

# Abstract

After many years of efficient application in the field of energy production, heavy-duty gas turbine are nowadays a mature technology that requires an intense control and maintenance program, typically referred to as Life Time Extension and Evaluation program (LTE). This routine involves multiple actors in several activities, of which this paper covers the numerical analysis of the FR1500 rotor to assess the reliability of old parts and find the opportunity of re-design new ones to make them longer-running. This work, in collaboration with Ethos Energy company, has the potential of bringing to a beneficial impact, because the outcome of the task is to provide more efficient solutions, exploiting all available resources. Finite Element Model (FEM) was adopted to simulate the rotor in multiple operating conditions, thanks to the knowledge of exhaustive performance data and machine parameter trends, coming from multiple sensors installed on a real operating rotor. Both steady-state and transient analysis have been run and robust design criteria approach was used to verify static-structural acceptability and to perform Low Cycle Fatigue (LCF) prediction, according to OEM-recommended Factored Fired Starts (FFS) and Factored Fired Hours (FFH). The Results found reveal multiple critical regions in some components, where stress intensification and concentration is caused by high thermal gradients and notch effects. In particular, turbine rotor wheels seem to be the most worrying components because, considering a safety margin for transients' intensification, LCF

evaluation estimates a low endurance limit for them. On account of this, re-design of critical areas and suggestions on further analysis have been proposed in the conclusions to this paper. Apart from localized issues, the entire review allowed to prove the general robustness of all the rotor components and ensures their creep resistance as well. Moreover, some of the investigated parts were believed to be promising candidates for life extension proposals, being the expected cumulated damage within the OEM specifications.

# Introduction

The case study of this paper deals with the thermo-structural analysis of the FR1500 gas turbine rotor to assess the lifetime of its components. The necessity of this research lies in the objective of reducing maintenance costs and especially those deriving from unexpected failures. The procedure followed initially aims to collect the notions necessary to understand the argument, embracing different areas of machine design literature and heat transfer theory. It combines them to develop a critical method of evaluating the solutions coming from numerical computation and to provide the data necessary for setting up the simulations. On account of this, the dissertation is divided in different parts ordered as much as possible according to the work flow. The first chapter gives an overview on Heavy duty gas turbines technology; it discusses its application and performances in the field of energy production and provides the theoretical fundamentals involved in the thermo-structural analysis. Specifically, the FR1500 rotor is presented in the second chapter, giving a description of the size of the machine and the different parts that compose it, explaining their geometry and their role within the general scheme. In addition, the cooling network of the turbine rotor is discussed in a separate paragraph, to explain how components interact with the secondary flow. The discussion about the experimental and analytical part is divided in the third and fourth chapter. In chapter 3 is addressed the steady-state analysis of the 2D rotor model and 3D sub-models of singular components, with particular

attention on the simulation setting. The different stresses, given as output of these simulations, are classified and verified according to the static-structural design criteria. Chapter 4 presents the transient analysis of the 2D model, explaining how to deal with variable boundary conditions, which depends on different parameters' trends of the machine. At the end of this chapter the Low Cycle Fatigue prediction of critical areas is provided and results are discussed according to the OEM-recommendations. Recalling plane stress theory introduced in the state of the art section, chapter 5 takes it up again in the implementation of the Grammel's method. This is done to introduce a sensitivity study on the effect of geometry and thermal gradients on principal stress distribution along the disk radius. Lastly, in the conclusive chapter major results are summarized to recap all findings and provide suggestion for future developments.

# Chapter 1

## Heavy Duty Gas Turbines

### 1.1 Introduction

Gas Turbines used in large thermoelectric power plants have nowadays a very important role in global electricity supply. In the last two decades this technology has experienced a fast grow up and today constitutes the core part of modern power plants. Most of the time heavy duty gas turbines are employed in combined cycle mode, showing an overall electrical efficiency of about 50-60 %. In this mode the high temperature exhaust gas flow is not wasted. Its energy is used to generate steam in a boiler. The latter is routed into a steam turbine where it expands while producing up to 50% more electricity than a traditional simple-cycle plant. The aim of this chapter is to provide a brief description of all theoretical fundamentals that are involved in this topic:

- it will be discussed the Brayton-Joule cycle, which represents the thermodynamic behaviour of the conversion energy process involved in the turbo-gas machine.
- A complete description of plane stress theory of axisymmetric bodies will be given in order to introduce the Structural analysis of rotor disks and other

components.

- It will be proposed a recall of heat transfer with a particular focus on convection theory, which find an important role in primary and secondary mass flow interaction with metal components of the rotor. Convective coefficient and film temperature are essential boundary conditions to be assigned in the Thermo-Structural analysis.
- Lastly a brief overview of Finite Element Analysis basics will be also given to introduce fundamentals of ANSYS software used in all simulations.

## 1.2 Brayton-Joule cycle

The Turbo Gas plant performs an Open cycle, because only external combustion plants, where the operating fluid works in a closed chain of thermodynamic transformations, can perform real closed cycle. The brayton-Joule is the thermodynamic cycle of reference for the Turbo Gas. From the thermodynamic cycle in Figure 1.1 we can follow all the phases involved in the conversion energy process:

- Air is sucked from the environment and it is compressed by the axial compressor 1-2 (1-2<sub>is</sub> ideally isotropic compression)
- Exhaust compressed air at the expected pressure ratio is then routed in the combustion chamber where a continuous fuel mass flow rate is injected at the right stoichiometric ratio between air mass flow and fuel " $\alpha$ ". Here is where continuous combustion process takes place 2-3. This transformation is not isobaric as in the ideal case, because of pressure losses concentrated and distributed ones

in the burner:

$$\eta_{\pi b} = \frac{P_3}{P_2} \quad \rightarrow \quad \beta_c = \frac{P_2}{P_1}; \quad \beta_t = \frac{P_3}{P_4} = \eta_{\pi b} * \beta_c \quad (1.2.1)$$

- High temperature Exhaust gasses from combustion process are now conveyed to expand in the Turbine. Here the enthalpy drop is used to generate useful work 3-4 (3-4<sub>is</sub> ideally isotropic expansion). The useful mechanical power is converted into electrical ones in the generator, located downstream to the turbine or upstream to the compressor.
- The isobaric line between point 4 and 1 is a fictitious transformation (indeed is not represented in bold) because we are talking about open cycles. Turbine Exhaust gasses are continually released in the environment or used to generate steam in combined cycle and new air at environmental pressure and temperature is continually sucked at point 1.

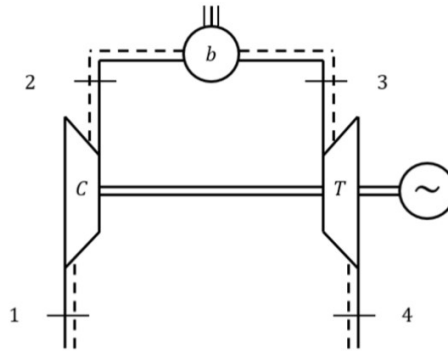


Figure 1.1: Schematic representation of the plant

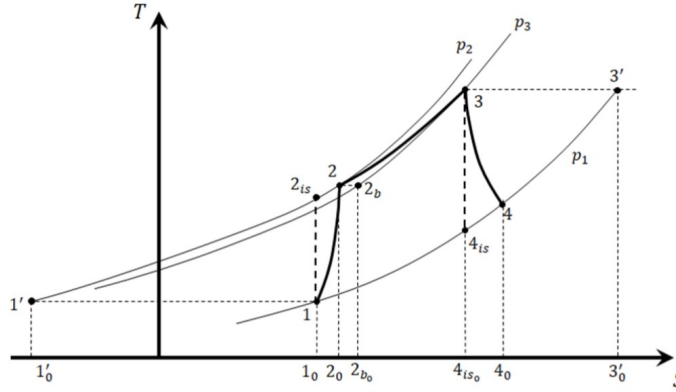


Figure 1.2: Thermodynamic cycle

As it can be seen from the T-S diagram in figure 1.2, the equivalent area, representative the compressor work, is the one bounded by  $1'_01'2_2_0$  that is composed by the isotropic work ( $1'_01'2_{is}1_0$ ) + the work against viscous losses ( $1_01_22_0$ ) + the Re-Heating effect ( $1_22_{is}2$ ). The equivalent area for the turbine performed work is equal to the isotropic work ( $4_{is_0}4_{is}3'3'_0$  area) - the work subtracted by viscous losses ( $4_{is_0}3_44_0$ ) + the Recovery Factor due to high temperature gas natural expansion ( $4_{is}3_4$ ). Here below are listed the equation for specific work calculation of both compressor and turbine, respectively  $l_c$  and  $l_t$ , that are represented by polytropic transformation in the T-S diagram  $Pv^m = const$ . The "m" exponent coeff. is different from the "k" one of the isotropic transformation, but from energy conservation equation is easy to find their analytical relation both for compression and expansion.

$$l_c = \frac{1}{\eta_{c,is}} c_p T_1 \left( \frac{\beta_c^{\frac{k-1}{k}}}{\beta_c} - 1 \right) = c_p T_1 \left( \frac{\beta_c^{\frac{m-1}{m}}}{\beta_c} \frac{1}{\eta_{y,c}} - 1 \right) \quad (1.2.2)$$

$$l_t = \eta_{t,is} c'_p T_3 \left( 1 - \frac{1}{(\eta_{\pi b} \beta_c)^{\frac{k-1}{k}}} \right) = c'_p T_3 \left( 1 - \frac{1}{(\eta_{\pi b} \beta_c)^{\frac{m-1}{m} \eta_{y,t}}} \right) \quad (1.2.3)$$

Where  $\eta_{is}$  and  $\eta_y$  are respectively the isotropic and polytropic efficiency. Notice that

$c_p$  is different from  $c'_p$  because the specific heat for compressor is related to air and the ones for the turbine to exhaust gasses.

### 1.2.1 Performances

Compressor, that is mechanically coupled with the turbine on the same axis, subtract power from the ones generated in the turbine side. the useful power is obtained as  $P_u = \eta_g G_b H_i$ . Where  $\eta_g$  is the Global Efficiency,  $G_b$  is the Fuel Mass Flow rate and  $H_i$  is the Low Heating Value of the Natural gas employed as fuel. From the previous definition of global efficiency, it is easy to find that:

$$\eta_g = \eta_m \eta_b \frac{\left[ \left( \frac{1 + \alpha}{\alpha} \right) l_t - l_c \right]}{Q_1} \quad (1.2.4)$$

where  $\eta_m$  is the Mechanical Efficiency and  $\eta_b$  is the burner efficiency. By definition  $Q_1$  is the introduced heat by fuel combustion and it can be also write as  $Q_1 = (G_b + G_a) * c'_p (T_3 - T_2)$ , where  $G_a$  is the mass flow of air. From that, knowing the expression for  $l_t$  and  $l_c$  by Eqs.1.2.2 and 1.2.3, assuming  $\left( \frac{1 + \alpha}{\alpha} \right) \sim 1$  and  $c'_p \sim c_p$ , we obtain [13]:

$$\eta_g = \eta_m \eta_b \eta_{t,is} \frac{\left[ \frac{T_3}{T_1} \frac{1}{(\eta_{\pi b} \beta)} \frac{1}{k} \frac{(\eta_{\pi b} \beta)^{\frac{k-1}{k}}}{\beta^{\frac{k-1}{k}}} - \frac{1}{\eta_{t,is} \eta_{c,is}} \right]}{\frac{\frac{T_3}{T_1} - \beta^{\frac{k-1}{k}}}{\beta^{\frac{k-1}{k}}} - \frac{1 - \eta_{c,is}}{\eta_{c,is}}} \quad (1.2.5)$$

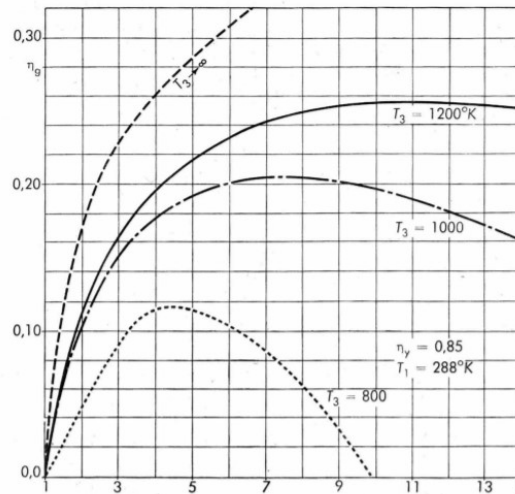


Figure 1.3: Global efficiency  $\eta_g$  plotted against  $\beta$  at different  $T_3$  temperatures

As it can be seen from the plot in Figure 1.3 the maximum global efficiency is influenced by the  $T_3$  temperature (If  $T_3 \uparrow \rightarrow \eta_{max} \uparrow$ ). The revolution in technology of high-efficient secondary flow cooling process and nickel super-alloy metals for rotor components make possible nowadays to reach a global efficiency of slightly more than 40 %. Anyway  $T_3$  represents a technological limit. That's why in thermoelectric plants they are usually employed in combined cycle. This configuration, compared to normal steam plant, has many advantages [1]:

- Higher electrical efficiency.
- Higher operating flexibility to support peak load of demand.
- Lower environmental impact.
- Lower costs of installation, maintenance and operating costs.
- High reliability

## 1.3 Thermo-Structural analysis fundamentals

### 1.3.1 Plane Stress theory of Axisymmetric bodies

The Plane Stress condition is applicable when a body has dimension in one direction that is much lower than the other two dimensions in the respective coordinates. When we talk about axisymmetric bodies the condition is true when the overall thickness of the body along the symmetric axis is much lower than the other dimensions. The theory that is discussed in this section has many applications in the evaluation of Principal Stresses of disks, which are undergoing mechanical and thermal load due to rotational speed (inertia) and thermal gradients [7]. Specifically to the case study it is proposed in Figure 1.4 a reference system in cylindrical coordinates to be consistent with the two Principal stress components in radial direction  $\sigma_r$  and in circumferential direction  $\sigma_\theta$ .

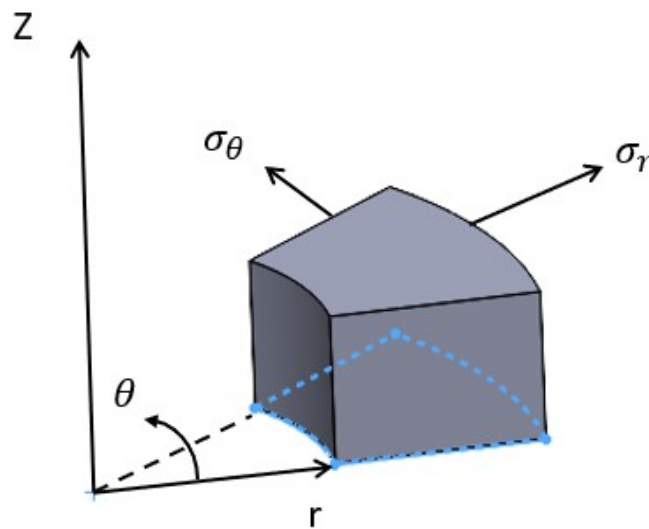


Figure 1.4: Sketch of reference system

$$\begin{bmatrix} \sigma_r & \tau_{r\theta} & \tau_{rz} \\ \tau_{\theta r} & \sigma_\theta & \tau_{\theta z} \\ \tau_{zr} & \tau_{z\theta} & \sigma_z \end{bmatrix} = \begin{bmatrix} \varepsilon_r & \varepsilon_{r\theta} & \varepsilon_{rz} \\ \varepsilon_{\theta r} & \varepsilon_\theta & \varepsilon_{\theta z} \\ \varepsilon_{zr} & \varepsilon_{z\theta} & \varepsilon_z \end{bmatrix} \quad (1.3.1)$$

In the above formulation 1.3.1 we have the resulting three dimensional Stress Tensor and Strain Tensor for the specified cylindrical reference system. If the disk is free on the lateral surfaces then we can correctly assume that on this faces:

$$\sigma_z = \tau_{zr} = \tau_{z\theta} = 0 \quad (1.3.2)$$

The plane stress assumption makes reasonable to assume that also inside the body is valid Eq. 1.3.2. Furthermore for the Stress tensor properties is also valid that:

$$\tau_{zr} = \tau_{\theta r} = 0 \quad (1.3.3)$$

Following the Hooke's law for the plane stress theory, the following relation for the deformation components is also true:

$$\gamma_{zr} = \gamma_{z\theta} = \gamma_{rz} = \gamma_{\theta z} = 0 \quad (1.3.4)$$

The  $\varepsilon_z$  deformation have no practical interest because it determines only a decrease in thickness in the symmetric z-axis direction without generating stresses. In our case the disk, which is an axysymmetric body, is loaded and constrained in an axysymmetric way. For these reasons it can be said that the body is subjected to a Plane Stress condition of axysymmetric type. As it was said at the beginning of the paragraph, The latter concept includes that the diagonal components  $\sigma_r$  and  $\sigma_\theta$  are principal component, so:

$$\tau_{r\theta} = \tau_{\theta r} = 0 \quad \gamma_{r\theta} = \gamma_{\theta r} = 0 \quad (1.3.5)$$

Finally, solving the Plane Stress problem means to find the four unknown function:  $U_r, \varepsilon_r, \varepsilon_\theta, \sigma_r, \sigma_\theta$ . Where  $U_r$  is the displacement components in radial direction which

is the only one unknown component of displacement [6]. In order to do it we can use one equilibrium equation in radial direction, two congruence equations and two equations for the constitutive links. The latter are:

$$\varepsilon_r = \frac{1}{E}(\sigma_r - \nu\sigma_\theta) + \alpha(T - T_0) \quad \varepsilon_\theta = \frac{1}{E}(\sigma_\theta - \nu\sigma_r) + \alpha(T - T_0) \quad (1.3.6)$$

where the term  $\alpha(T - T_0)$  is the initial component of deformation only due to thermal load effect.

Both Equilibrium and Congruence equations will be described in detail, later-on in a dedicated chapter.

### 1.3.2 Heat Transfer Theory

We defined *heat* as a transitional energy because it moves from one body to another as result of thermal potential, the difference in temperature between two systems. Heat transfer problems can be steady-state problems (temperature can vary among different points of the system, but at each point it cannot vary in time), or transient (Temperature can change among points and in time) [2]. Both problems are faced by any kind of system in thermal machinery and the Turbo Gas plant is not an exception. There are three modes of transferring heat:

- Conduction
- Convection
- Irradiation

In this chapter it will be discussed conduction and convection, because they are the two main mechanisms involved in the thermal load of the turbo gas machinery operation.

#### CONDUCTION

Conduction can take place in all the physical state of matter, but it is the main mechanism involved in heat transfer inside solids. The rate of heat conduction through a solid depends on specific material properties and temperature difference. In three dimensional medium, according to the phenomenological Fourier model [15], the rate of heat conduction at any point of the body can be expressed as:

$$\dot{Q}_n = -kA \frac{\partial T}{\partial n} \quad (1.3.7)$$

Where "n" is the normal versor to the isothermal surface "A" at the same point and "k" is called Thermal Conductivity of material, which is a "*measure of the ability of a material to conduct heat*" [2] in  $[W/m \cdot K]$ . On the other hand the ability of material to storage Energy is called Heat Capacity and it express as  $\rho c_p$ , where  $\rho$  is the density and  $c_p$  the specific heat capacity. In practise this term represents how much energy is necessary to enhance of 1 K the temperature of a unit volume body  $[J/m^3K]$ .

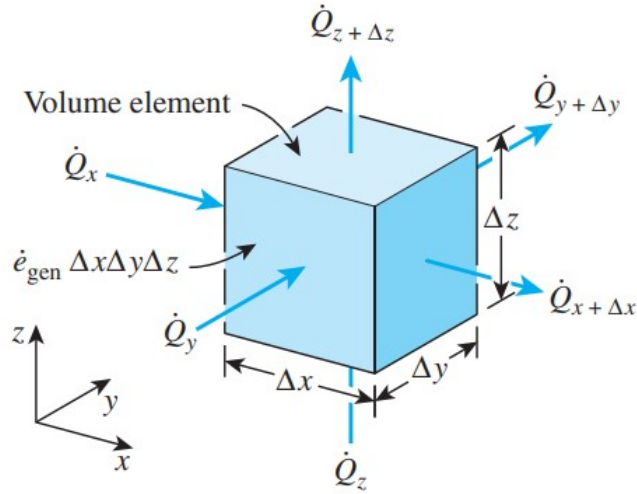


Figure 1.5: Volume element [2]

At the light of these definitions, taking as reference a rectangular volume in figure 1.3.1, whose dimensions ( $\Delta x$ ,  $\Delta y$ ,  $\Delta z$ ) lay on the Cartesian axis, if we perform an energy balance in this volume during a time interval, it will be obtained:

$$\dot{Q}_x + \dot{Q}_y + \dot{Q}_z - \dot{Q}_{x+\Delta x} - \dot{Q}_{y+\Delta y} - \dot{Q}_{z+\Delta z} = \frac{\Delta E}{\Delta T} \quad (1.3.8)$$

considering no source of energy inside the volume. Now considering equation 1.3.7 and taking the limit of  $\Delta x$ ,  $\Delta y$ ,  $\Delta z$ ,  $\Delta t \rightarrow 0$ , it is easy to demonstrate with a few

mathematical passages that 1.3.8 becomes:

$$\nabla \cdot (k \nabla T) = \rho c_p \frac{\partial T}{\partial t} \quad (1.3.9)$$

In the case of constant "k" and writing the expression in extended form, it will be obtained the Heat Conduction equation in Diffusion form:

$$\frac{\partial^2 T}{\partial x^2} + \frac{\partial^2 T}{\partial y^2} + \frac{\partial^2 T}{\partial z^2} = \frac{1}{\alpha} \frac{\partial T}{\partial t} \quad (1.3.10)$$

where  $\alpha = \frac{k}{\rho c_p}$  is the Thermal diffusivity.

## CONVECTION

The main difference of Convection Heat Transfer is that it happens always in presence of bulk fluid motion. The latter in combination with conduction is the way by which a fluid exchanges heat with a solid surface. Convection is a very complicated phenomena and it is still nowadays one of the most critical mechanisms to determine by analytical equations and empirical relations. Basically what Newton's law of cooling told us is that convection heat transfer is proportional to the difference in temperature between the solid surface  $T_s$  and the free stream undisturbed one  $T_\infty$  [2].

$$\dot{Q}_{conv} = hA(T_s - T_\infty) \quad (1.3.11)$$

Where A is the area of the surface and h is the Heat Transfer Coefficient (HTC), defined as the rate of heat transfer between a solid and a fluid per unit surface area, per unit of temperature difference [ $W/m^2 \cdot K$ ]. Despite the simple equation 1.3.11 the difficult tasks consists in determine this "h" coefficient and the experience told us that it is a big issue. Basically HTC is function of lots of parameters, more or less

difficult to be determined.

$$h = f(\mu, k, \rho, c_p, V, T_s, T_\infty, \text{Geometry of the solid, surface roughness, fluid flow regime}) \quad (1.3.12)$$

The variables, which have not already been described are:

- $\mu$ : Dynamic Viscosity coefficient [ $Kg/m \cdot s$ ]
- $V$ : Fluid free Stream velocity [ $m/s$ ]

Deriving a simple equation that described "h" as a function of all these variable would be grate, but it is still not possible today.

Taking as example the fluid motion over a flat plate, the velocity and the temperature distribution would be similar to the one in Figure 1.6. For both velocity and temperature it is possible to define a thickness of the velocity/thermal boundary layer as the distance between the the surface of the plate and the  $0.99V$  or  $T_s + 0.99(T_\infty - T_s)$  respectively, defined as  $\delta$  for velocity and  $\delta_t$  for temperature. The zero velocity condition of fluid in proximity of plate's surface is known as the "no-slip condition" and it suggest that at that point we don't have fluid motion, which means that heat transfer from solid surface to adjacent fluid layer is by pure conduction [2]. We can state that:

$$\dot{q}_{conv} = \dot{q}_{cond} = -k_{fluid} \frac{\partial T}{\partial y} \Big|_{y=0} \quad \longrightarrow \quad h = \frac{-k_{fluid} \frac{\partial T}{\partial y} \Big|_{y=0}}{T_s - T_\infty} \quad (1.3.13)$$

Where y-coordinate is in the vertical direction in figure 1.6. It means that if we are able to find the thermal distribution very close to the wall we can find the thermal gradient at  $y = 0$ . Anyway, apart from some particular experimental cases, this is not always possible.

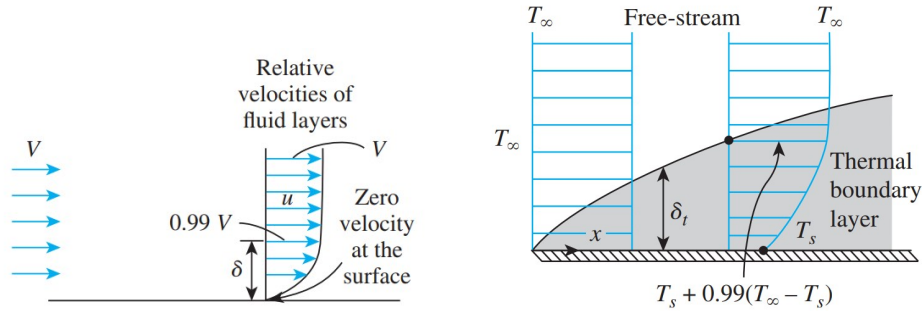


Figure 1.6: Velocity and Temperature distribution

### *Non-Dimensional Parameters*

In convective heat transfer, experience suggests that the best practice is to look for a set of similarity conditions. The latter are described by a series of non-dimensional parameters, which are in turn defined by groupings of HTC depending variables, Eq. 1.3.12.

- The **Nusselt Number** "Nu" is defined as the ratio between heat transfer by convection and heat transfer by conduction and it is expressed as  $Nu = \frac{hL_c}{k}$ , where  $L_c$  is the characteristic length of the problem. Better to say "Nu" is "*the enhancement of heat transfer through a fluid layer as result of convection relative to conduction across the same fluid layer*" [2]. From this definition is evident that Nusselt must be  $Nu > 1$ .
- The **Prandtl Number** "Pr" is defined as the ratio between the molecular diffusivity of momentum and molecular diffusivity of heat and it is expressed as  $Pr = \frac{\mu c_p}{k}$ . Velocity profile of the fluid depends on its viscosity, because fluid and its surrounding exchanges frictional forces that are kept into account in the momentum balance equation. In case of fluid over the flat plate the friction force per unit area is proportional to the velocity gradient  $\tau_w = \mu \frac{\partial u}{\partial y} \Big|_{y=0}$ . Fluid velocity have a strong influence on temperature profile, so the way in which

thickness of thermal and velocity boundary layers are related has a strong effect on HTC.

- The **Reynolds Number** "Re" is defined as the ratio between inertial forces and viscous forces and it is expressed as  $Re = \frac{\rho V L_c}{\mu}$ . This parameter is used to describe the flow regime and it is strongly related to the forced convection. Depending on the case study, knowing the membership range of Re, we can define if the flow is laminar rather than turbulent.

As it was just said, finding an analytical solution for HTC, is not an easy task. It has been done, for example, by Eng. H. Blasius in the case fluid over a flat plate.

We can think to numerically solve Navier Stokes Fourier NSF set of equations to derive at any point the temperature and velocity distribution and, by 1.3.13, the HTC. Engineering speaking, it is convenient to find a local average "h" coefficient in a portion of the domain of interest. In this case the empirical approach consist in exploiting the Buckingham Theorem, to find a relation between previously discussed non-dimensional parameters. Theorem states that if an equation is dimensionally homogeneous, it can be reduced in the form of a relation between a series of non-dimensional parameters, that are in number as the difference between the number of physical quantities that characterised the phenomena and the minimum number of fundamental entities (units of measure) involved [12].

The aim of this discussion is not to present all the analytical passages involved in this problem, that can be easily found in literature. Here below we present the resulting power-law relation in which the "Nu" is a function of "Re" and "Pr" numbers:

$$Nu = C Re^m Pr^n \quad (1.3.14)$$

where m, n and C constants can be determined experimentally. The good news is that

nowadays exists lots of empirical numbers for these constants that are suitable for a huge variety of engineering cases. another advantage of the non-dimensional nature is used to scale Nusselt number from known geometrically similar cases. From Nu, HTC can be easily derived by knowing the characteristic length of the problem.

### 1.3.3 Low Cycle Fatigue Analysis

Fatigue consists in a full set of phenomena by which a structural system, which is undergoing cyclic loading condition, shows a lower resistance compared to the one detected by static loading analysis.

This analysis is crucial for turbo-gas rotor components. Moreover experience with this machinery suggests that the highest levels of localized stresses occurs during transients (Start-up and Shut-down phases), where elastic and plastic deformations can occur together (see hysteresis  $\sigma - \varepsilon$  cycle in Fig. 1.7). In account of this, Low Cycle Fatigue (LCF) analysis is used to check for number of cycles to failure. Rotor components are expected to run without fails through all the OEM-recommended Factored Faired Starts (FFS) [9].

Multiple analytical approaches are available to perform LCF calculations. The plastic-strain contribution in LCF suggests to follow a strain-controlled approach, that is also well-known as the strain-life approach. Manson-Basquin-Coffin model is based on the total strain partitioning [5] in Elastic strain contribution  $\varepsilon_{pl}$  + Plastic strain one  $\varepsilon_{el}$  and the relative equation is:

$$\varepsilon_a = \frac{\Delta \varepsilon}{2} = \frac{\Delta \varepsilon_{el}}{2} + \frac{\Delta \varepsilon_{pl}}{2} \quad \longrightarrow \quad \varepsilon_a = \frac{\sigma'_f}{E} (2N_f)^b + \varepsilon'_f (2N_f)^c \quad (1.3.15)$$

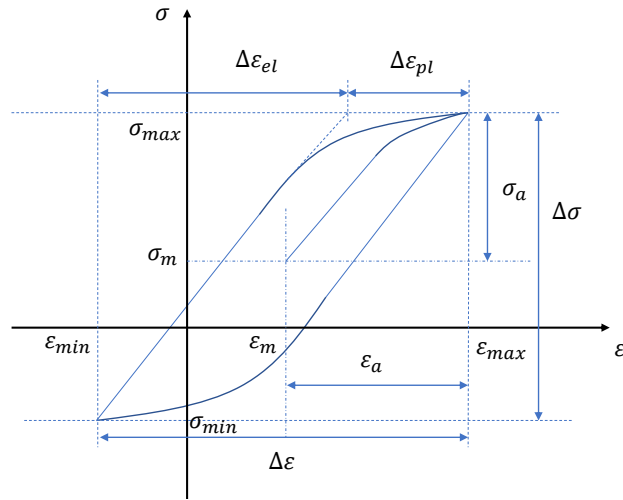


Figure 1.7: Hysteresis  $\sigma - \epsilon$  loop

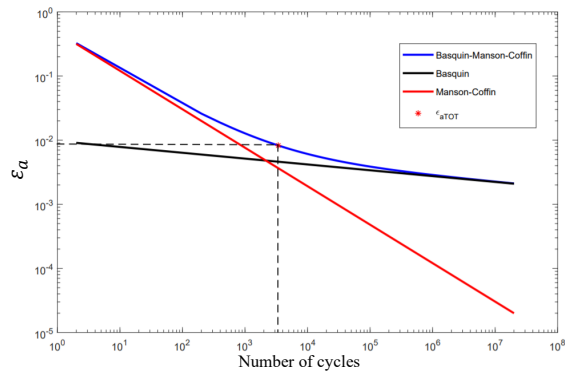


Figure 1.8: Manson-Basquin-Coffin log-log  $\epsilon - N_f$  plot

where:

- $\sigma'_f$  is the fatigue strength coefficient
- $\epsilon'_f$  is the fatigue ductility coefficient
- $b$  is the fatigue strength exponent
- $a$  is the fatigue ductility exponent
- $E$  is the elastic modulus

In figure 1.8 is evident how the resulting curve (blue one) is highly influenced by the plastic contribution, which is the Manson-Coffin second term of the relation 1.3.15, when  $N_f$  is lower than approximately  $10^4$  cycles.

In Eq. 1.3.15 The first term multiplied by  $E$  is  $\sigma'_f(2N_f)^b = \sigma_{ar}$ , which is the equivalent fully reversed (Stress ratio  $R = \frac{\sigma_{min}}{\sigma_{max}} = -1$ ) stress amplitude. The fully reversed condition means that this method is suitable only for zero mean stress  $\sigma_m = 0$ . As it can be seen in Figure 1.7 this is not always the case, especially for our case study. Anyway a real benefit of Strain-Life approach is that we can modify the previous expression in order to account for mean stress contribution [8]. The Smith-Watson-Topper model [16] is a way by which this can be done and it states that the product  $\sigma_{max}\varepsilon_a$ , at a given life, remains constant for different combinations of the maximum stress and the strain amplitude.

Given the fact that sigma alternating  $\sigma_a$  for a fully reversed case is equal to  $\sigma_{max}$ , then:

$$\sigma_{max}\varepsilon_a = \frac{\sigma_f'^2}{E}(2N_f)^{2b} + \varepsilon_f'\sigma_f'(2N_f)^{b+c} \quad (1.3.16)$$

The Smith-Watson-Topper stress  $\sigma_{SWT}$  used to build the fatigue curve can be computed using the following equation:

$$\sigma_{SWT} = \sqrt{\sigma_{max}\sigma_a} = \sqrt{\sigma_{max} \cdot E \cdot \varepsilon_a} = \sqrt{\sigma_{max} \frac{\sigma_{max} - \sigma_{min}}{2}} = 0.707\sigma_{max}\sqrt{1-R} \quad (1.3.17)$$

The procedure starts collecting material data test results for  $\sigma_{max}$  values at the corresponding  $N_f$  cycles to failure. The corresponding  $\sigma_{SWT}$  value is then computed from Eq. 1.3.17, accounting for the corresponding  $R$  value of each test. Now the computed points are somehow interpolated in order to find suitable coefficient to substitute in Eq. 1.3.16. Explaining a complete mathematical procedure to perform the necessary

interpolation, is not the aim of this section.

Once coefficient are known, Fatigue curves at different temperatures can be obtained with high reliability by employing the material physical and mechanical properties at the considered temperature instead of room temperature (RT). Most of the time test data are collected at RT, so this operation allows only considering the normal decay of the mechanical characteristics with the temperature increase. Clearly it is not inclusive of the further performances diminution caused by the mutual interactions between creep and fatigue. Anyway Palmgren-Miner's cumulative damage law can be used to keep into account the mutual action of creep and fatigue.

## 1.4 Fundamentals of FEM

The structural analysis of complex structures is the area in which Finite Element Analysis (FEA) stands out for its computing power and reliability. In many engineering fields FEA is intensively used and its results are accurately analysed and post-processed. The concept behind FEA is the necessity of discretize continuous thermal or/and mechanical problems. Essentially the method is used to solve in a discretized and approximated form systems of partial differential equations (PDEs). The first step of FEM consists in dividing the structural physical domain in lots of polygonal elements (2D case) or prismatic elements (3D case), called Elementary Elements. Polygons can share vertices and edges but they cannot overlap. Each vertex represents a Degree of Freedom of the whole system and it takes the name of Node. This operation is called "meshing" and, despite it is almost an automatic task carried out by modern FEM software (e.g. ANSYS SW), it requires lots of experience to create a well-done mesh in complex geometries. Type of mesh elements, their distribution and density have a huge impact in the numerical results of simulations. Experience we are talking about, involves multiple competences and a good engineering sense. Of course computational time increases as number of elements rises, so the correct behaviour is trying to find the right balance among coarse mesh and fine mesh, using the latter only when we expect to have big gradient in stress distribution, or where we want to have a better numerical control of the solution. The topic we are talking about has multiple years of history background in research and development, so the aim of this section is only to give some basics fundamentals and to discuss how the method manipulates some of the governing equations used for our purpose.

Let us consider a isotropic and homogeneous body and an infinitesimal parallelepiped volume inside it, whose corners lay on the three Cartesian axis  $x, y, z$ . For it we can write the undefined equilibrium equations, as follows:

$$\begin{cases} \frac{\partial \sigma_x}{\partial x} + \frac{\partial \tau_{xy}}{\partial y} + \frac{\partial \tau_{xz}}{\partial z} = f_x \\ \frac{\partial \tau_{yx}}{\partial x} + \frac{\partial \sigma_y}{\partial y} + \frac{\partial \tau_{yz}}{\partial z} = f_y \\ \frac{\partial \tau_{zx}}{\partial x} + \frac{\partial \tau_{zy}}{\partial y} + \frac{\partial \sigma_z}{\partial z} = f_z \end{cases} \quad (1.4.1)$$

Where  $f_x, f_y, f_z$  are the external forces per unit volume applied to the element. Now for sake of simplicity we take as example a membrane body  $\Omega$  (e.g. Figure 1.9), whose thickness is negligible, comparing to the other dimensions in the x-y plane. The contour of the body is called  $\partial\Omega$  and the normal-to-border vector is  $\hat{n}$  [3].

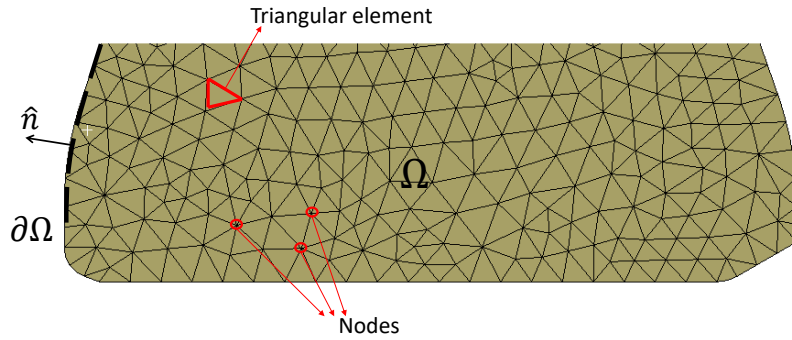


Figure 1.9: Example of a 2D domain mesh grid

If we consider for that particular case a force  $f$  per unit volume applied on the membrane surface in z-direction, then our equilibrium condition becomes:

$$\frac{\partial \tau_{zx}}{\partial x} + \frac{\partial \tau_{zy}}{\partial y} + f = 0 \quad (1.4.2)$$

Following the constitutive equation (Hooke's law), we can define stresses by mean of partial derivatives of displacement components.

$$\begin{aligned} \tau_{zx} &= \frac{E}{(1+\nu)(1-2\nu)} \cdot \frac{(1-2\nu)}{2} \gamma_{zx} = \mu \left( \frac{\partial u_x}{\partial z} + \frac{\partial u_z}{\partial x} \right) \\ \tau_{zy} &= \frac{E}{(1+\nu)(1-2\nu)} \cdot \frac{(1-2\nu)}{2} \gamma_{zy} = \mu \left( \frac{\partial u_y}{\partial z} + \frac{\partial u_z}{\partial y} \right) \end{aligned} \quad (1.4.3)$$

Where  $\mu$  is the elastic coefficient. Given the fact that we suppose to deal with little deformations, the  $u_y$  and  $u_x$  components can be considered negligible w.r.t  $u_z$  [3]. At that light, avoiding to use notation indices The equilibrium equation (1.4.2) becomes:

$$-\nabla \cdot (\mu \nabla u) = f \quad (1.4.4)$$

If we multiply the equilibrium equation by a generic admissible displacement  $v$  and we integrate the previous expression on the domain  $\Omega$ , we obtain:

$$-\int_{\Omega} \nabla \cdot (\mu \nabla u) v d\bar{x} = \int_{\Omega} f v d\bar{x} \quad (1.4.5)$$

Where  $\bar{x}$  is equal to the vector  $\begin{pmatrix} x \\ y \end{pmatrix}$ . Now, making usage of divergence theorem and exploiting integral properties the Eq. 1.4.5 becomes the following:

$$\int_{\Omega} \mu \nabla u \cdot \nabla v d\bar{x} - \int_{\partial\Omega} \mu \frac{\partial u}{\partial n} v dS = \int_{\Omega} f v d\bar{x} \quad (1.4.6)$$

Where  $S$  is the Boarder's abscissa. This equation from a physical point of view is equivalent to the Principal of Virtual Work.

In order to discretize the problem we can choose  $u_h$  and  $v_h$  admissible displacement at each node as result of a linear combination with a basis function, called  $\phi$ . This is a *piecewise polynomial* continuous function defined at each node [3].

$$u_h(\bar{x}) = \sum_{k=1}^N u_k \phi_k(\bar{x}) \quad (1.4.7)$$

For  $k = 1, 2, \dots, N$ . In order to simplify things let us suppose  $v = 0$  at the domain's border  $\partial\Omega$ . In such a way we obtain:

$$\int_{\Omega} \mu \nabla u_h \cdot \nabla v_h d\bar{x} = \int_{\Omega} f v_h d\bar{x} \quad (1.4.8)$$

Given the fact that  $v_h$  is a general displacement it can be considered  $v_h = \phi_j$  for  $j = 1, 2, \dots, N$ .

$$\int_{\Omega} \mu \nabla u_h \cdot \nabla \phi_j d\bar{x} = \int_{\Omega} f \phi_j d\bar{x} \quad \longrightarrow \quad \sum_{k=1}^N u_k \int_{\Omega} \mu \nabla \phi_k \cdot \nabla \phi_j d\bar{x} = \int_{\Omega} f \phi_j d\bar{x} \quad (1.4.9)$$

Without entering in details on how is defined  $\phi$  basis function, what is clear from Eq. 1.4.9 is that the problem was reduced to an algebraic system of  $N$  equations in  $N$  Unknowns  $u_k$ .

$$[A] \{u\} = \{F\} \quad (1.4.10)$$

Where components of  $[A]$  are  $a_{jk} = \int_{\Omega} \mu \nabla \phi_k \cdot \nabla \phi_j d\bar{x}$  and for  $\{F\}$ ,  $f_j = \int_{\Omega} f \phi_j d\bar{x}$ .

What we have described is a structural equilibrium problem. Note that in case of thermal problems, equilibrium equations are the same. If we take Eq. 1.3.9 in the steady state case:

$$-\nabla \cdot (k \nabla T) = 0 \quad (1.4.11)$$

Where it is not considered a rate of heat generation inside the element. The latter term would be the equivalent of  $f$  in the previous expression.

## BOUNDARY CONDITIONS

In order to find a solution for such problems it is necessary to impose boundary conditions. The latter are divided in three different type:

- **Dirichlet** boundary conditions
- **Neumann** boundary conditions
- **Robin** boundary conditions

Applying the first (Dirichlet) means to know the value of displacement or temperature at a specific border region; let us call that region  $\Gamma_D$ . This condition also means that each node along  $\Gamma_D$  is no more a d.o.f. of the system, so these nodes are not counted as unknown terms.

without being original, the border in which we have Neumann condition is called  $\Gamma_N$ . This condition means to apply the normal component of heat flux (in thermal model) or the normal stress component (in elastic model) [3]. Usually when we do not apply any condition at a border of the domain, modern software automatically applies Homogeneous Neumann condition, which means to put zero value for the previously mentioned quantities. In Thermal model that means to have an adiabatic wall, so a boarder in which the body does not exchange heat with the environment. If both conditions are applied to the body, it means to solve the following problem:

$$\begin{cases} -\nabla \cdot (\mu \nabla u) = f & \text{in } \Omega \\ u = g & \text{in } \Gamma_d \\ \mu \frac{\partial u}{\partial n} = \phi & \text{in } \Gamma_N \end{cases} \quad (1.4.12)$$

Now the second boarder integral of the first term of Eq. 1.4.6 is:

$$\int_{\partial\Omega} \mu \frac{\partial u}{\partial n} v dS = \int_{\Gamma_D} \mu \frac{\partial u}{\partial n} v dS + \int_{\Gamma_N} \mu \frac{\partial u}{\partial n} v dS \quad (1.4.13)$$

So that the discrete integral formulation bacomes:

$$\int_{\Omega} \mu \nabla u_h \cdot \nabla v_h d\bar{x} = \int_{\Omega} f v_h d\bar{x} + \int_{\Gamma_N} \phi v_h dS \quad (1.4.14)$$

The last boundary condition (Robin) is widely used in Thermal simulation of rotor components. The major part of rotor components surfaces are run-over by the air cooling flow, whose thermodynamic properties are provided by flow path simulations results. Following Eq. 1.3.13 in sub-section 1.3.2, on that surfaces (boarders in 2D case) it can be imposed that the heat flux is proportional to the difference between the free stream temperature and the unknown temperature of the wall.

$$K \frac{\partial T}{\partial n} = h(T_{\infty} - T) \quad (1.4.15)$$

In sub-section 1.3.2 we have just provided a brief explanation on how HTC "h" can

be estimated. Now, assuming  $\psi = hT_\infty$ , the new discrete integral formulation is:

$$\int_{\Omega} \mu \nabla u_h \cdot \nabla v_h d\bar{x} + \int_{\Gamma_N} h u_h v_h dS = \int_{\Omega} f v_h d\bar{x} + \int_{\Gamma_N} \psi v_h dS \quad (1.4.16)$$

Note that the presented equations can be reduced to a similar algebraic system of equations 1.4.10, but there will be new entries both for coefficient matrix  $[A]$  and known term vector  $f$ .

# Chapter 2

## Rotor Description

### 2.1 Summary

The subject of this paper is the FR1500 heavy duty gas turbine. This model belongs to the F-class turbines technology, which is now approaching more than 20 years of operating service life. The FR1500 is thought to serve an electricity grid with a line frequency of 60 Hz, typical of American's countries. In order to do it, its nominal velocity of rotation is 3600 RPM, so it is not connected to the grid by mean of a gear box, because it does not need a gear ratio. FR1500 is able to give as output a nominal power of around 170 MW, processing approximately 445  $Kg/s$  of total exhaust mass flow rate. The aim of this chapter is to give a brief description of FR1500 Turbogas machine. In particular the focus will be the rotor part, that is the object of our analysis. The machine is basically divided in two sides. The first one is the axial compressor section made up of 18 stages, counted from 0 to 17 as in Figure 2.1. Each of them is composed by a rotor followed by a stator. Air is progressively squeezed as it flows through stages, increasing pressure and temperature. It happens in diffusing channels among stator blades, by conversion of the kinetic energy gained through rotor blades. Before the turbine side, air is burned with injected natural gas fuel in the *reverse-flow* type combustor, made up of 10 combustion chambers. In axial

turbine section the exhaust gasses expand within three stages. In this case the rotor of the stage is anticipated by the stator, that is commonly known as Nozzle.

In that particular F-class turbine the generator is located upstream to the compressor. This implies that the produced mechanical torque is completely transferred from the turbine side to the compressor, through the marriage flange between the *Distance Piece* (DP) and the last (17-th) *Compressor wheel* (CW). The compressor consumes the 55-65% of the total power produced and the remaining is transferred to the generator, where it is converted into electrical power. The entire rotor is supported by mean of two bearings mounted one on the forward FWD *Stub-Shaft* and the other on the afterward AFT *Stub-Shaft*.

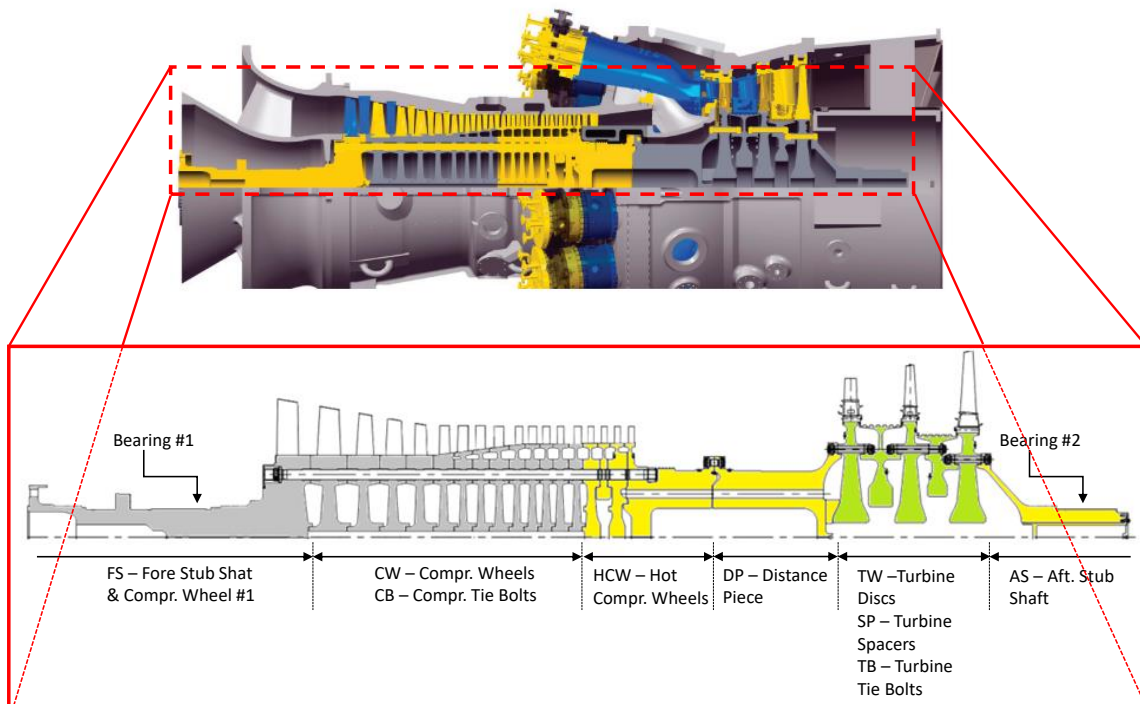


Figure 2.1: FR1500 3D model and rotor section representation

In the following pages it is proposed a deeper description of some rotor components to give a better understanding of the system geometry and assembly. In this way it will be clearer how parts of interest interact with each other.

## 2.2 Compressor

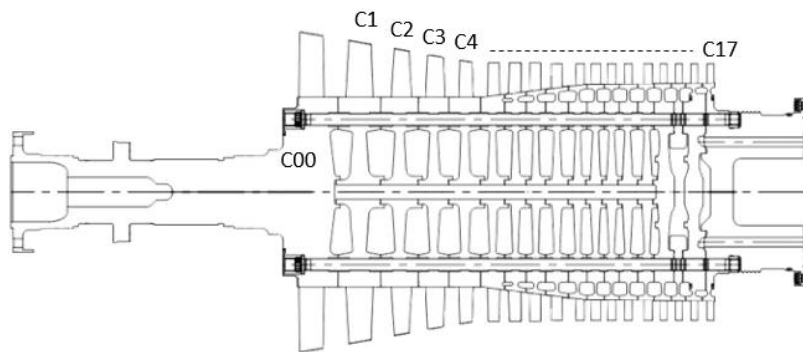


Figure 2.2: FR1500 section of compressor rotor assy

As it was anticipated in the summary, the compressor assy is made up of 18 stages. In Figure 2.2 it can be seen the cross section of the assembled rotor part from compressor wheel C00 to C17. From 2.2 it is clear that all of them are perforated disks (central hole called *Borehole*) except Hot Compressor Wheels (HCW) C14, C16, C17 and the first C00. The latter plays also the role of FWD *Stub Shaft*, because they belong to the same solid metal component. All CW are held together by mean of 15 tie bolts, which passes through all the wheels. Compressor wheels are not press fitted on a common solid axis, probably because of the maintenance program. Disks needs to be periodically inspected and even substituted if they are no more usable. This requires the capability of disassemble and reassemble them. About this, all the compressor wheel are centred with interference fit. Each disk is coupled with both the previous one and the subsequent one with male-female mechanical coupling. Re-

ferring to the sub-model picture to the right in Figure 2.3 , the male part is forward and the female part is afterward. Not all the disks are centred in *borehole* proximity, some of them (e.g. C15-C16-C17) are different for design requirements.

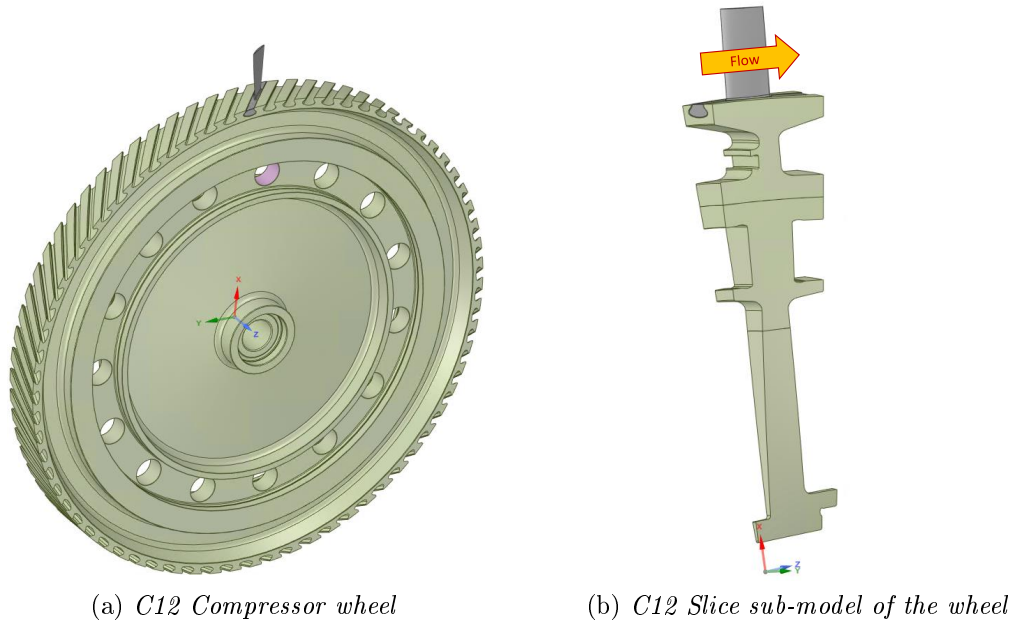


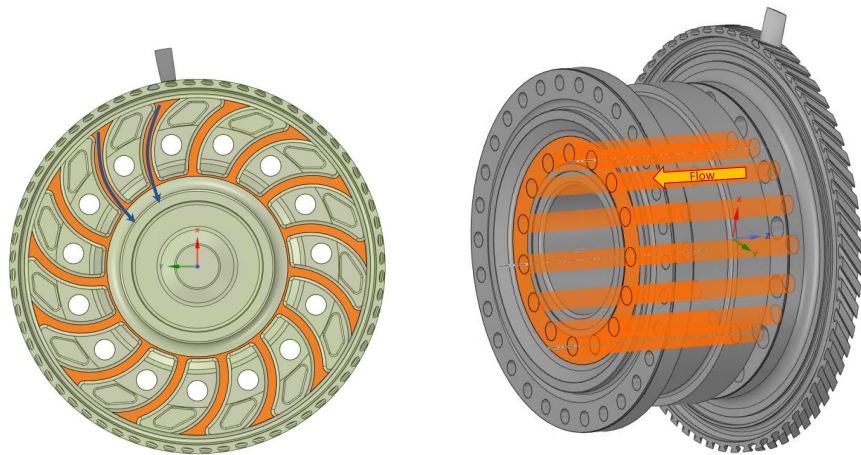
Figure 2.3: C12 compressor wheel

It can be also noted in 2.3 that blades are fixed to the disk with a *dovetail* slot. This seat shape is used to prevent blade from sliding away because of centrifugal forces acting during operating conditions.

Not all the compressed air, sucked from the environment, is burned in the combustion process. A little percentage of that air is used to cool down turbine disks and rotor blades. The entire cooling network will be described later on in this chapter. Currently we want to highlight how this air is shipped from the compressor to the turbine section, by-passing combustor.

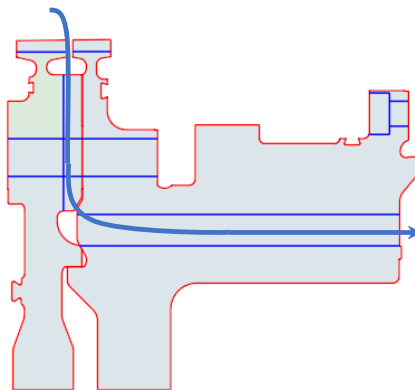
Referring to Figure 2.4 ,air is drawn off between C16 an C17 CW and then, thanks to a fan effect, it is routed inside the fifteen tubular channels through out all the C17

disk's width (b). The fan is created by the air slot channels of the impeller on the AFT side of C16 disk (a). The flow path of cooling flow is sketched in (c).



(a) C16 CW AFT side frontal view

(b) C17 CW AFT side lateral view



(c) C16-C17 CW 2D section

Figure 2.4: representation of C16 and C17 CW with cooling flow path sketch

Cooling air flow keeps going on the same number of tubular channels in the *Distance Piece* component (Figure 2.5 ) (a), which has also the role of separating the turbine section and it is connected to C17 compressor wheel by mean of a marriage flange (b). The latter holds the two sides with 27 tie bolts.

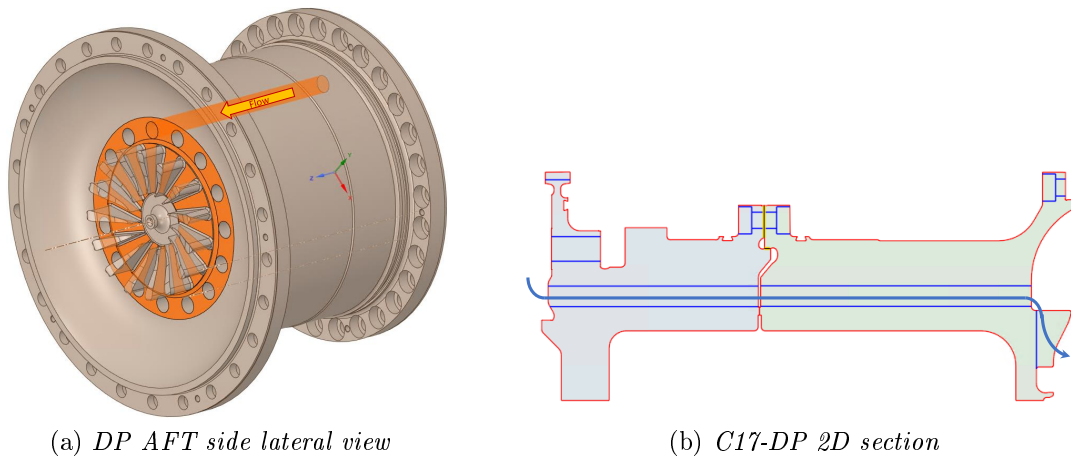


Figure 2.5: representation of DP with cooling flow path sketch

## 2.3 Turbine

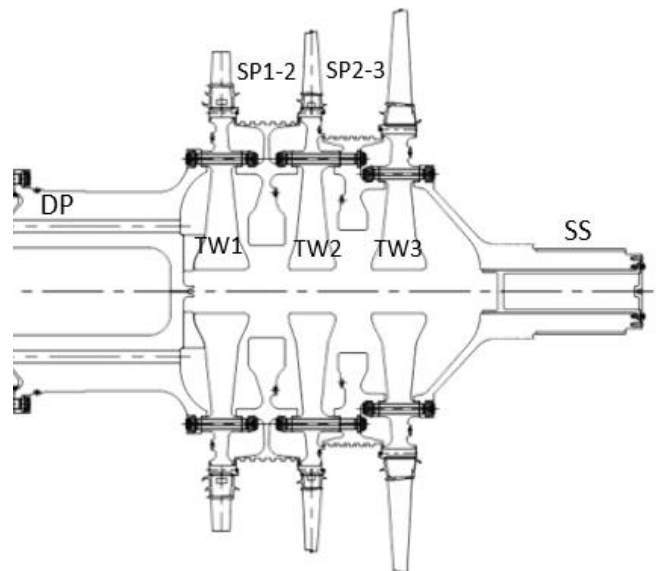


Figure 2.6: FR1500 section of turbine rotor assy

As it was anticipated in the summary, the turbine assy is made up of 3 stages. In Figure 2.6 it can be seen the cross section of the assembled rotor part from DP to AFT *Stub Shaft* (AS). The three Turbine Wheels (TW1, TW2, TW3) are separated by mean of two Spacers (SP1-2 , SP2-3) to guarantee the right distance between rotor blades an stator blades (vanes). The former are fitted on the external diameter of TWs thanks to *fir-tree* shape slot. This particular geometry is needed in order to assure a better grasp during severe operating condition loadings (high rotational velocity, high temperatures , aerodynamic loads). The *fir-tree* slots, in figure 2.7(b), are more difficult to be manufactured w.r.t. *dovetails* ones, but this design requirement is not an option.

All the turbine components are centred with male-female mechanical coupling with some amount of interference. Unlike the compressor, here the assembled rotor is not packed by a unique set of tie bolts. A set is used for each stage, holdings 3 components at a time as it is clearly visible in Figure 2.6 (DP $\longleftrightarrow$ TW1 $\longleftrightarrow$ SP1-2; SP1-2 $\longleftrightarrow$ TW2 $\longleftrightarrow$ SP2-3; SP2-3 $\longleftrightarrow$ TW3 $\longleftrightarrow$ AS). The bolts' material is the same of the disks and the number of them is 24 for the first two sets and 18 for the third set respectively. The holes for the bolts, called *Through Bolt Hole* (TBH), are in proximity of the central planes as in Figure 2.7(c), where TW2 sub-model section is taken as example. In order to give an idea of the whole turbine wheel, from which the sub-models were derived, the TW2 disk is proposed in Figure 2.7(a).

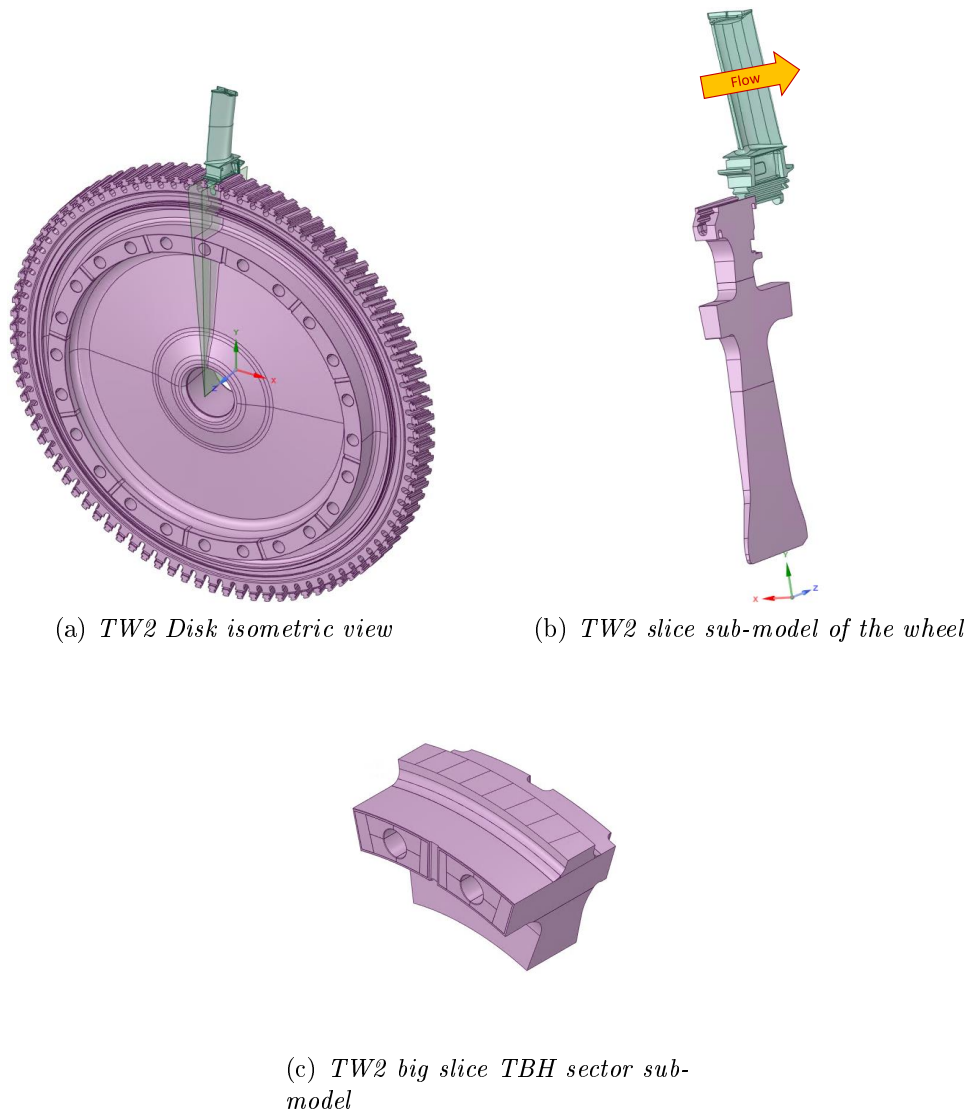


Figure 2.7: TW2 whole disk and sub-model geometries

### 2.3.1 Cooling flow

Following the scheme in figure 2.8, the cooling air coming from the compressor is forced to flow through the TW1 *borehole* by the fan on the AFT side of the DP (Figure 2.5). Then the flow is spread out over the free side surfaces of the disks. In this way evacuation of heat from metal components is guaranteed. The cool down

process is also very important for the first and second stage rotor blades, that are in direct contact with the main high-temperature exhaust gas flow. Air is conveyed inside the internal blade cooling circuit, passing through the air slot channels of the disks and spacer SP1-2, then penetrating the appropriate hole in the Blade root slot. Circuits inside rotor blades can follow a very complicated path. That is the case of TW1 blade, which has a very complex geometry named Serpentine Cooling, designed to enhance the convective heat transfer efficiency. Second stage blade channels are vertically straight, but they are turbulated for the same design reason and the third stage rotor blade is not internally cooled.

The cooling air is then reintroduced in the main flow by mean of micro-holes in proximity of the blade trailing edge (1<sup>st</sup> stage) or over the tip (2<sup>nd</sup> stage). Also stationary blades in the turbine side are in contact with high-temperature gasses so they need to be cooled down too. The cooling air, that flows inside the vanes, is not coming from the DP's hole channels. In this case the Compressor bleed air system plays a big role, because it serves two purposes:

- It manages the air flowing into the compressor for surge prevention
- It provides cooling airflow to turbine stationary vanes during normal operation

The first row of vanes is cooled by air that is routed through the combustor shell from the compressor discharge. Cooling air flows through the hollow blades and exits the cooling holes on the pressure sides surface, near the trailing edge. Air flow for the other vanes is drawn off by the compressor bleed of different stages, depending on the pressure level, but in this case it is not reintroduced in the main flow from the side of the blade. Indeed, air flows all the way to the root of the vane and then it is partially conveyed in the labyrinth seals designed on the external diameter of spacer

components SP. Here the vortices allow an efficient heat exchange but they do not prevent air from exiting and join the main flow path. In figure 2.9 (b) it is possible to see in detail the air slots on the SP1-2 wheel (a) and the labyrinth seals geometry.

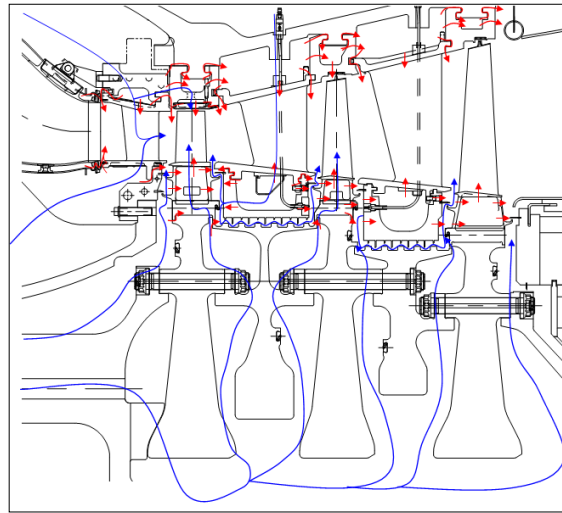
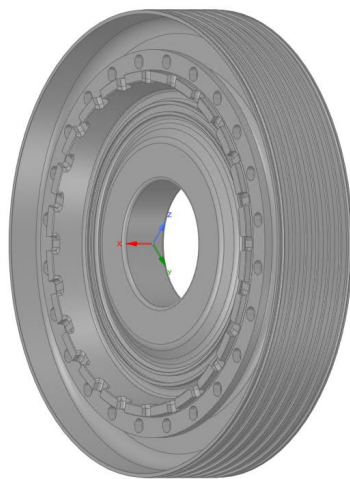
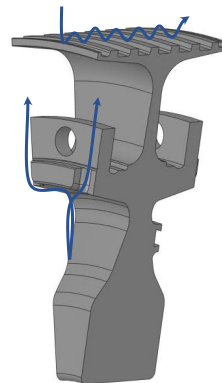


Figure 2.8: Cooling scheme of turbine disks and blades



(a) *SP1-2 disk isometric view*



(b) *SP1-2 slice sub-model with air flow path sketches*

Figure 2.9: SP1-2 Turbine spacer

# Chapter 3

## Steady-State FEM Analysis

### 3.1 Introduction

The Finite Element Analysis (FEA) is an essential component of a robust Lifetime Evaluation and Extension program (LTE) [9]. It includes 3D model steady-state simulations of the singular components and 2D model, both steady-state and transient, simulations of the entire rotor as a whole. In this chapter it will be analysed the behaviour of turbo gas during normal operating condition, thus covering the steady-state part. A spontaneous question could be why a 2D model should be kept into account in this type of analysis. Recalling section 1.4, every type of continuous system needs to be described by multiple elementary elements, connected by nodes, which represents the total number of degrees of freedom of the problem. A complete 3D model would require millions of d.o.f and, computationally speaking, it is not suitable for the purpose of a company routine analysis because it is time consuming and difficult to be properly prepared. Anyway mutual interaction within components must be taken into account and, in that light, a whole 2D model, if properly designed, could be an agile tool to produce as output a good approximation of reality. Indeed, a normal work-flow needs 2D simulation in order to estimate contact pressure in mechanical-couplings regions. This would become an important input data for the

3D simulation of the singular component. On such account, recalling chapter 2, ANSYS advanced tool allows to manipulate only a little slice of compressor/turbine disks that are representative of the whole geometry because of cycling symmetry. This operation consists of dividing the disk in slices with a certain cutting angle, that can be called pitch-angle. Cutting planes (e.g. Figure 2.7 (a)) can be misaligned with respect to the disk's axis in order to include the entire root blade slot (b). Some particular geometrical features (TBH and air slots) can be included only considering a bigger cutting-angle. This is why, in the case of compressor and turbine wheels, analysis are also carried out for a wider angle sector, called Big Slice model (e.g. Figure 2.7 (c)). The complete Geometry derivation of the 3D models is not the purpose of this paper. In this chapter will be presented the following points:

- 2D model simulation setup, that is also partially valid for the 3D case, apart from the constraints applied.
- Presentation and comparison of results from 3D and 2D Analysis outputs.
- Static structural acceptability verification.

## **3.2 2D model Analysis Setup**

### **3.2.1 Geometry validation and material properties characterization**

The very first step of each kind of thermo-structural analysis is the physical and mechanical properties assignment. A turbo-gas rotor is a set of different materials properly assigned to each component, depending on the design purpose. Collecting material data from literature or experimental tests is not an easy task. Often lots of effort in this field is spent in order to gain a competitive advantage. Once collected,

data needs to be correctly interpreted and processed in order to fully characterized a specific material.

The rotor assy is not made of perfectly axisymmetric bodies. Disks and shafts, as it was previously described in chapter 2, have a break in the material along the circumferential coordinate, like TBH, *blade root slots*, *air cooling channels* and *slots*. These particular geometrical features are not possible to be captured in a 2D representation and, giving the absence of material in these regions, they do not contribute in supporting loads. It translates in a localized lack of rigidity of the structure. On such account, for these specific portions of the domain, assumptions are needed for modelling in a proper way the overall component's behaviour under thermo-mechanical loads with a good approximation.

Experience in this practice suggests two main assumptions:

1. Plane stress behaviour assignment with a calculated average thickness.
2. Localized orthotropic material properties correction.

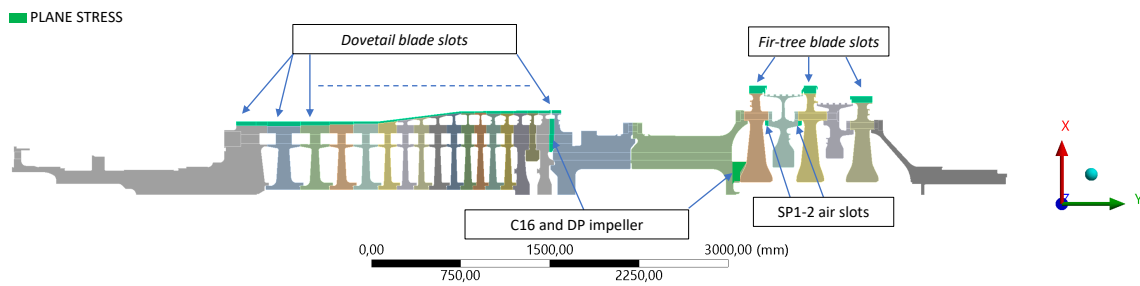
The first condition is imposed where the considered geometry has a free end. As you can see in Figure 3.1 (a), that is the case of:

- *dovetail* and *fir-tree* slots
- C16 and DP impeller geometry
- SP1-2 FWD and AFT air slots

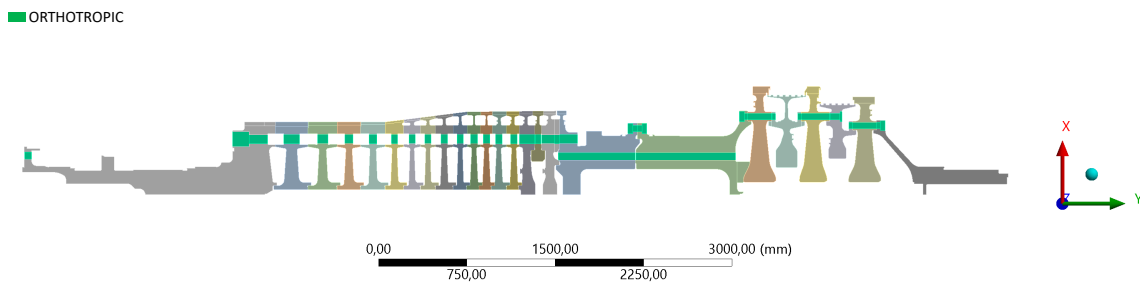
SP1-2 FWD and AFT air slots have a very big dimensions along the rotor axis coordinate, compared to other disks, so they cannot be neglected. For each of them a proper thickness "T" based on geometrical consideration have been assigned. As general rule

in this calculation is important to estimate the percentage of full surface/volume and empty surface/ volume along the average circumferential axis. Mathematical details for this process cannot be released, because of intellectual proprietary rights of the company.

The second condition is made for bolts' holes and relative nuts (TBH) as in Figure 3.1 (b). Material properties were reduced in these regions assuming an orthotropic condition. It means that the young modulus in the circumferential direction ( $z$ -axis)  $E_\theta$  was reduced, considering the ratio between the full area and the one depurated from holes contribution, averaged along the hole's diameter. Share modulus in the same direction is reduced consequently  $G_\theta = \frac{E_\theta}{2(1 + \nu)}$ .



(a) Plane stress assumption



(b) Orthotropic material properties assumption

Figure 3.1: Non-axisymmetric geometriacal features

The rest of the geometry is assumed to have an axisymmetric behaviour, which means that the software interprets that surface as it is the half-cross section of a rotational solid. Blades are the only rotor's element that cannot be treated in the 2D case. It means that we are not able to provide with a 2D model temperature map or stress distribution on blades. Only 3D submodels analysis can deal with this task, but in any case blades have not been analysed in this paper. Even if stress results in blades are not of interest, we need to keep them into account both for thermal boundaries and centrifugal load condition, because they affect the entire simulation. The thermal part will be discussed later on in boundary condition section. About the centrifugal load, it have been simulated using a lumped point-mass in the center of mass of blades or blades+wedges, which are devices designed to keep some rotor blades fixed on the compressor side. Once defined their coordinates and total weight, Point-mass are remotely attached on the *dovetail* or *fir-tree* slots. This operation, practically speaking, means to anchor the points-mass with infinitely rigid wires to the specified edge of the geometry. Another technique consists in estimating centrifugal forces of blades and directly apply them to the edges. In that way the pressure distribution is assumed to be homogeneous, so this approach is less efficient than the previous one. The first is a better approximation of real loading conditions. The correct coordinates of the centres of mass are crucial for real and good stress result. Experience shows that a little error in the positioning can result in a big intensification of stresses in localized regions. An exemplary image of turbine side in Figure 3.2 is provided to better understanding the concept.

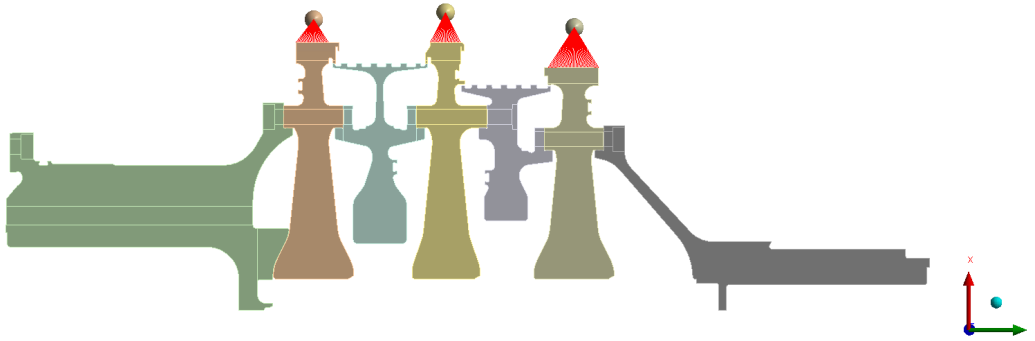


Figure 3.2: Point-mass sketch on turbine side

### 3.2.2 Meshing and connection control

As it was anticipated in section 1.4 the meshing operation is more than an art, that requires years of experience in FEA field. The technique used in the 2D model considers only triangular mesh elements, because they provide a good result saving up a bit of computational time.

As first approximation a mesh size was chosen for the overall surface. Afterwards, in proximity of specific geometrical features, it will be refined in order to better approximate real shape. Fillet radius, grooves and sharp edges are all examples of this regions, where machine design experience foresees stress concentration. An example of this geometries is provided as magnifications in figure 3.3, where it is clearly visible how the mesh was refined up to a certain deep inside the surface in order to capture the high stress gradients. Anyway the previous operation needs to be carefully managed, because the drawback is to consider to many elements than really necessary, which is time consuming and consequently costly for a firm.

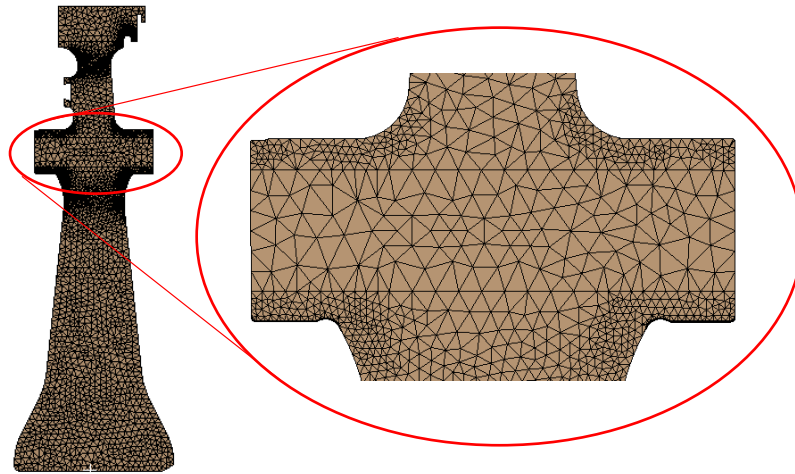


Figure 3.3: TW1 example of mesh distribution

Issues in meshing definition arises also in contacts among components. In central planes, where we have interference fit between the two bodies, it should be applied another tool called "inflation". As it can be seen in Figure 3.4, this command allow the software to create in both side thin layers of resized mesh that helps the contact resolution process. Interference is defined by an initial interpenetration size, called clearance fit  $\Delta$ . This condition is solved by the software, because no penetration is allowed at the end of the simulation. This is done in different ways depending on the algorithm that is used, but in any case the process is iterative. Contact forces are applied to push the parts apart until there is no more penetration.

In this process, as well as in real couplings, the parts may deform, develop compressive stresses, and create a contact pressure between the two parts. The software enables to define different kinds of contacts. By default the contact is set to be bonded and it does not allows rigid relative motion between parts. So in general is necessary to change it in frictionless or frictional type. The latter is difficult to treat when a certain grade interference is present, because of predominance of non-linearities phenomena. For that, load step solution could be a better choice, by which ANSYS applies forces step

by step proportionally to the contact stiffness  $k$  and residual amount of penetration  $F = k\Delta$ . A sketch is provided in Figure 3.4.

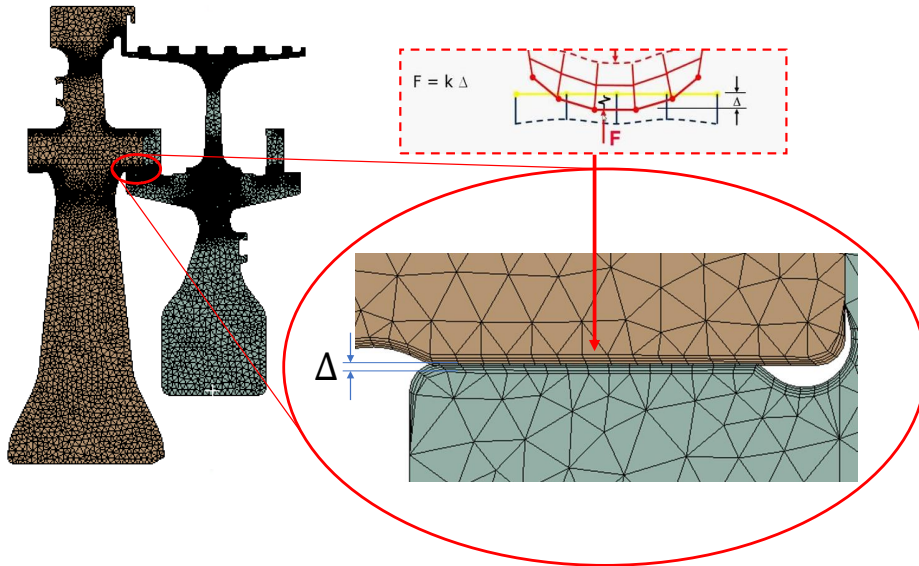


Figure 3.4: TW1-SP1-2 connection example

### 3.2.3 Mechanical and Thermal Boundary conditions

Boundary conditions must be applied to the model borders in order to fully define the thermal and mechanical problem. In this section it will be provide a complete explanation on how boundary conditions have been computed and defined, starting from mechanical ones and finishing with thermal boundaries.

#### MECHANICAL

The mechanical boundaries are all the constraints and forces applied to the structure. Referring to the 2D model, the only constraint applied is a "zero" displacement condition in y-direction, portrayed in figure 3.5. It behaves like a "rocker", so it admits displacement in x-direction and rotation in x-y plane. The condition is used to allow the rotor to move axially and vertically both for thermal expansion effect and

centrifugal loads. The latter is provided in the numerical model giving in input the nominal rotational speed of the rotor, as it is also indicated in Figure 3.5. The last

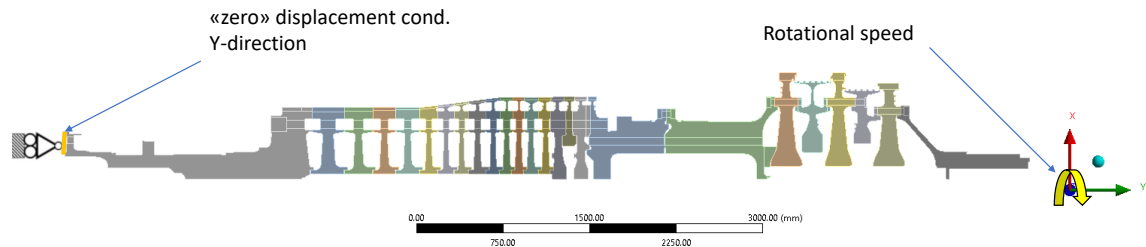


Figure 3.5: Rotor constraint and rotational speed

mechanical boundary condition is the Pre-tension of bolts. In this case FEA bolts are not considered as physical entities, but forces acting normally to the involved surface borders. As it has been described in in chapter 2, the FR1500 turbogas rotor is assembled by mean of 5 sets of tie bolts. One set of 15 units is used for the compressor side and another one of 27 units is used for the *marriage flange* between C17 and DP (see Figure 2.5 (b)). For these two sets total bolts pre-load was given by the company in steady-state operating conditions, as result of estimation based on similar machines available data. For the three sets of turbine tie bolts, instead, the pre-load value as been separately evaluated with a dedicated analysis.

This is divided in two phases of a cyclic process. The first one consists in an analytical approach, based on assembled bolt elongation and the second one is a 2D FEM analysis of the turbine rotor assy, used to evaluate compressed parts shortening.

Bolts can be seen as a cylindrical beam, whose task consist in holding two or more parts together preventing them from separate and sliding one on the other. By that definition is clear that held parts and bolts exchange equal forces in modulus in opposite direction,  $F_p$  and  $F_v$  respectively, in order to reach equilibrium condition. That is quite easy to appreciate, looking to the bolt and part characteristic curves force

Vs. displacement in Figure 3.6, where  $u_p$  and  $u_v$  are the displacements for part and bolt respectively. The slop of curves w.r.t. the vertical axis is the resilience. Having

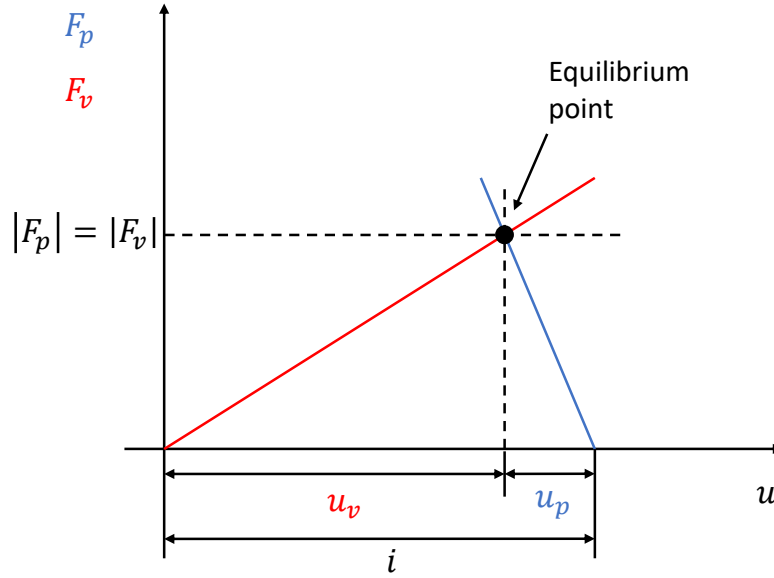


Figure 3.6: Bolt-Part characteristic curves

available assembled bolt elongations, the problem consists in evaluating the previously mentioned resilience of bolts to get the pre-load force for each turbine stage, by:

$$F = \frac{u_b}{\delta_b} \tag{3.2.1}$$

Where  $\delta_b$  is the bolt's overall resilience and  $u_b = u_v$ . That is obtained by the sum of all resiliences within the clamp length. These are the no-threaded stem resilience, the engaged thread one for both sides and the engaged thread of both nut and trap nut resiliences (see figure 3.7).

$$\delta_i = \frac{l_i}{EA_i} \tag{3.2.2}$$

Referring to de Saint Venant Eq. 3.2.2 is used to compute it, where "E" is the same for all the elements, because they are made of the same material. More details on this argument can be easily found in literature [4]. The entire process to compute bolt

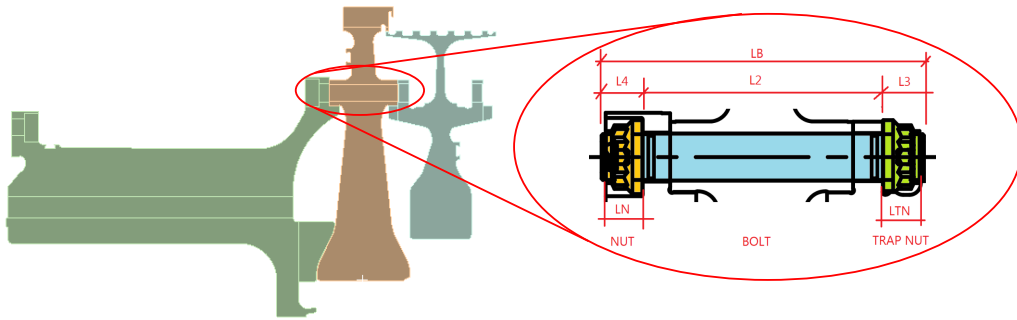


Figure 3.7: #1 stage bolt geometry example

pre-load can be abbreviate with the following schematic algorithm.



Figure 3.8: Pre-load algorithm calculation scheme

Anyway steady-state condition is different from the assembled one, because rotor is rotating at a constant angular velocity (3600 RPM) and operating temperature is higher than room temperature (RT). It means that the input data must change according to Poisson's effect, thermal expansion and properties temperature-dependence. In account of this, starting from No-load case (assembled condition), pre-load force estimation has been extended to different cases, hereunder listed.

1. No-load condition (just described)
2. Full speed, no thermal load (typical of power on phase, when rotor starts rotating until it reaches regime RPM condition, but it has not already reached the thermal base load)
3. Steady-State condition (regime rotational speed and stationary metal temperature)

4. No speed, full thermal load (typical of shut-down phase, when the rotor is "almost" fixed and metal temperature is still high)

**CASE 2**

Giving nominal rotation and no thermal load, we start from 2D steady-structural analysis of the rotor in ANSYS, assigning estimated pre-load forces of CASE 1 as first attempt. Looking to Figure 3.6, the sum of  $u_p$  and  $u_b$ , called interference  $i$  is constant as long as temperature is constant, because no rotating loose is allowed. Aware of this, we check for  $u_p$  value in simulation results and so we obtain a new value of bolt elongation, by  $u_b = i - u_p$ . Now following the scheme in Figure 3.8 we compute a new value of pre-load force, which is a second attempt input data for the 2D simulation. From now on the procedure continue as before until  $u_p$  value is stable and so  $u_b$ . In that way pre-load forces can be estimated with a good approximation. Iterative approach summarized in the following table.

<i>Interference <math>i=const.</math></i>								
Attempts	#1	#2	#3	...	...	...	...	#N
$u_p$	$u_p'$	$u_p''$	$u_p'''$	...	...	...	...	$u_p^N$
$u_v$	$u_v'$	$u_v''$	$u_v'''$	...	...	...	...	$u_v^N$
Pre-load force (F)	$F'$	$F''$	$F'''$	...	...	...	...	$F^N$
variation %								

**CASE 4**

In this case the procedure is the same of case 2, but interference  $i$  must change according to thermal expansion. At that light we compute the independent dilatation of bolts and parts of each stage. In this way we obtain a new interference value, based on the previous one + the difference between axial dilatation of bolts and parts. In order to estimate thermal expansion of bolt, a dedicate 2D FEM analysis was done for each stage assuming an axysymmetric behaviour. For completeness, an image of

second stage turbine 2D-meshed-surface is provided in Figure 3.9

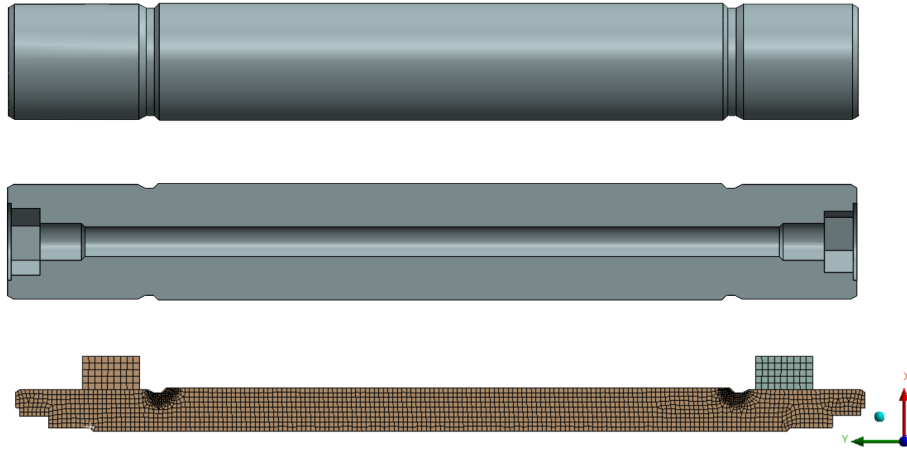


Figure 3.9: #2 stage Tie bolt 3D model and 2D meshed cross section surface

### CASE 3

In the Steady-State condition we start from interference  $i$  computed in case 4, but we need to iterate following same rational of previous cases to keep into account Poisson's effect.

In the following scheme in Figure 3.10 we provide a schematic loop to describe the common computational process of all cases.

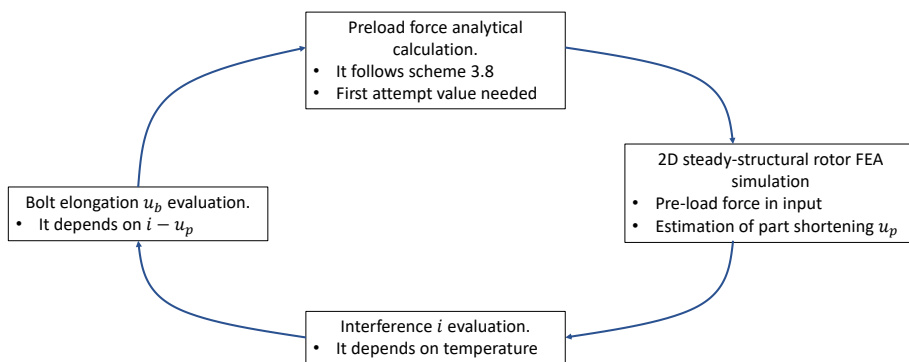


Figure 3.10: Iteration scheme

As result of this analysis we can conclude with useful informations that will be used also to describe transient analysis. For each bolt kit (# 1;# 2;# 3), in figure 3.11, plots of bolt-part equilibrium force are provided, at different operating conditions (1, 2, 3, 4). It is quite easy to notice the temperature effect on Young modulus "E". It decreases as long as temperature increases and, according to Eq. 3.2.2, resilience increases. Also interference  $i$  increases according to the rising in temperature. Equilibrium forces are expressed in percentage w.r.t. the case 1 pre-load force. Depending

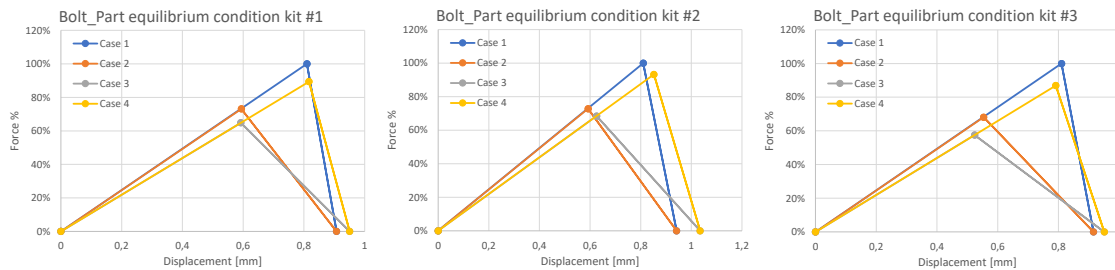
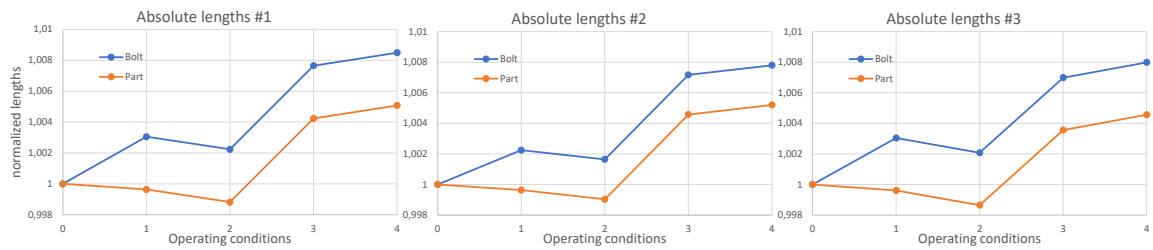


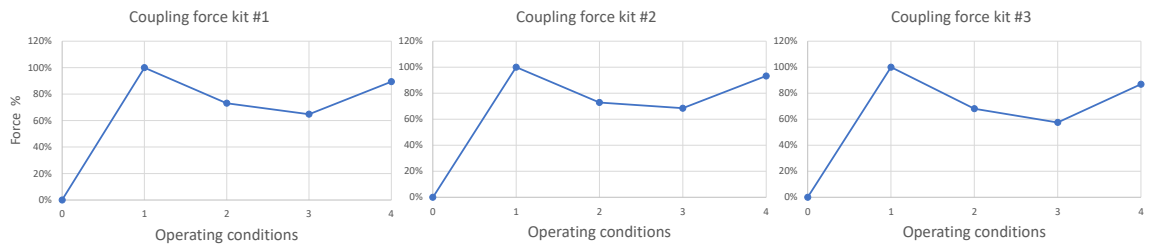
Figure 3.11: bolt-part characteristic curves for each stage

on bolt elongation and part shortening the absolute length of both them changes case by case. Looking at figure 3.12 (a), in case 1 it is clear that in assembled RT condition the Bolt stretches more than part shortens. The lengths are normalized with respect to the "zero" condition length, which means unloaded condition. In case 2 absolute lengths of both part and bolts decreases because of Poisson's effect. In case 3 the thermal expansion increases lengths more than case 1, despite Poisson's effect is still present. Quite intuitively the maximum lengths are reached in case 4 because centrifugal load is no more present, but thermal effect is still acting. At that light, it is quite easy to understand plots in Figure 3.12 (b), where coupling forces, in percentage w.r.t. case 1 force, are plotted case by case for each turbine stage. The latter are computed, multiplying pre-load forces for number of units per each set.

Not surprising, in case 2 coupling force decreases according to Poisson's effect. In case 3 the thermal expansion of both part and bolt almost compensate each other, so it determines a bolt elongation quite similar to case 2. Anyway high temperatures affect physical properties and in particular young modulus "E", decreasing it. This translates in a lack of rigidity and consequently coupling force decreases. In case 4 the absence of centrifugal load influences bolts elongation so much, that coupling force increases more than in case 2 for each turbine stage.



(a) Absolute lengths



(b) Coupling force

Figure 3.12: Bolt's lengths and total exerted coupling forces

2D and 3D analysis are not completely independent of each other. 2D structural simulation results are needed in order to define exchanged pressure in contact regions. This output data is a necessary input in the 3D sub-model analysis of singular components. If the simulation runs without those conditions, the resulting stress distribution won't represent real operating condition.

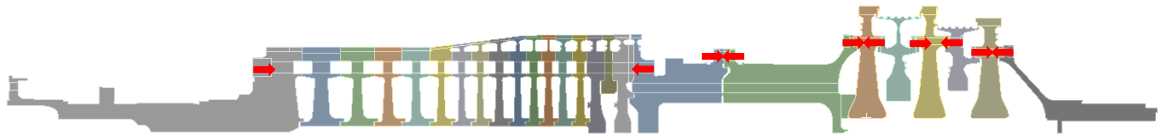


Figure 3.13: Vectors of bolt's pre-load forces

## THERMAL

In order to define the steady-state thermal problem, proper Robin and Dirichlet boundary conditions (described in section 1.4 ), needs to be assigned on the domain borders.

- Robin conditions has to be assigned to the borders in contact with the main or secondary flow (cooling flow)
- Dirichlet condition has to be assigned where metal temperature needs to be given

Regarding the former, the cooling flow, described in section 2.3.1, has to be previously studied. To that purpose *Ethos Energy* company uses a dedicated software, that is able to model the flow resorting to a 1-D assumption. The tool keeps into account multiple kind of losses and leakages to give as output thermodynamic variables (Temperature, pressure, mass flow rate,...) at any point of the given flow network. Input data comes from firm-proprietary performance file of the FR1500 turbogas. No further details will be given about this kind of analysis, whose useful results have been provided by the company.

Ones thermodynamic variables are known, the model domain can be divided in iso-condition regions. The goal consists in defining an average film temperature  $T_f$  and an average convective-heat-transfer coefficient  $h$  for each of them. By these informations Robin condition can be applied to the borders included in each region. they can be

seen, as highlighted edges, in the 2D-model surfaces in Figure 3.14.

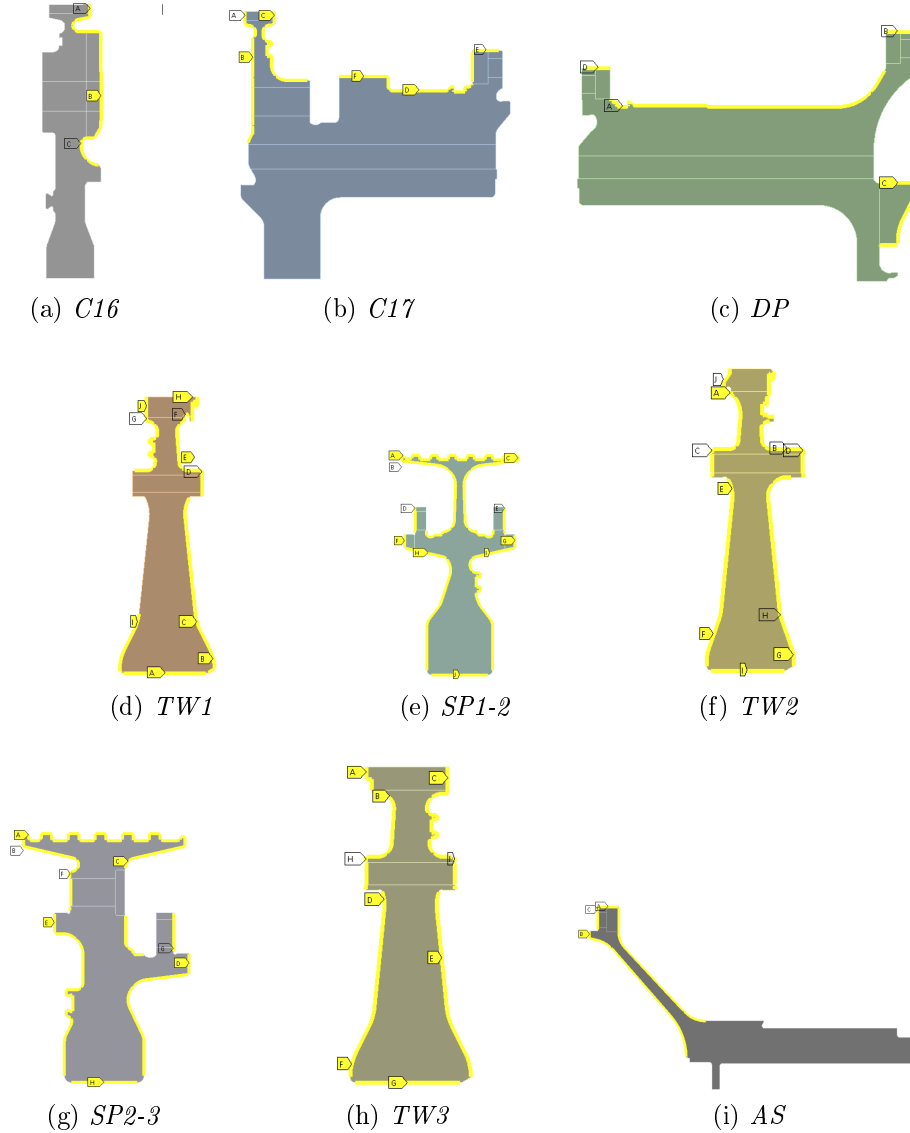


Figure 3.14: Highlighted edges of components in contact with air cooling flow

$h$  coefficient is estimated following two approaches:

**1<sup>st</sup> APPROACH**

Starting from provided values of mass flow rate, pressure and temperature, air properties can be derived, such as density  $\rho$ , kinematic viscosity  $\nu$  and so on. According to compressor and turbine assy geometry, air passage section for each region can be

defined, and so equivalent diameters can be computed from them. Now, following definitions provided in 1.3.2, all non-dimensional parameters can be derived in order to compute Nusselt number  $Nu$  by a suitable form of Equation 1.3.14 present in literature. Consequently convective-heat-transfer can be computed.

### 2<sup>nt</sup> APPROACH

Exploiting similarities among different machines,  $h$  coefficient can be derived. This is done by scaling it from a known value using a company formulation, part of design criteria fundamentals.

$$h = h_{ref} \frac{k}{k_{ref}} \frac{D_{eq}}{D_{eq_{ref}}} \left( \frac{Re}{Re_{ref}} \right)^{0.8} \quad (3.2.3)$$

Where  $D_{eq}$  is the equivalent diameter and pedex "ref" stands for "referent value", that is the one of similar machine used as example.

Results coming from the two approaches are both valid approximations, but they are slightly different values. The chosen one is the minor, to be as more conservative as possible. If  $h$  coefficient is lower, the heat-flux from solid metal to cooling air will be underestimated. It represents a more severe operating condition because steady metal temperature becomes higher.

Air cooling channels, used to drive air cooling flow from compressor side to turbine side through C17 and DP, are internal regions of the structural domain. This implies that Robin condition is difficult to be applied here using a 2D-model approach. The problem can be overcome using a Dirichlet boundary condition in that case. The temperature distribution can be derived from 3D steady-thermal map results and applied, as given, in the channel region surfaces as a fixed temperature condition. To clarify this concept a sketch is provided in Figure 3.15.

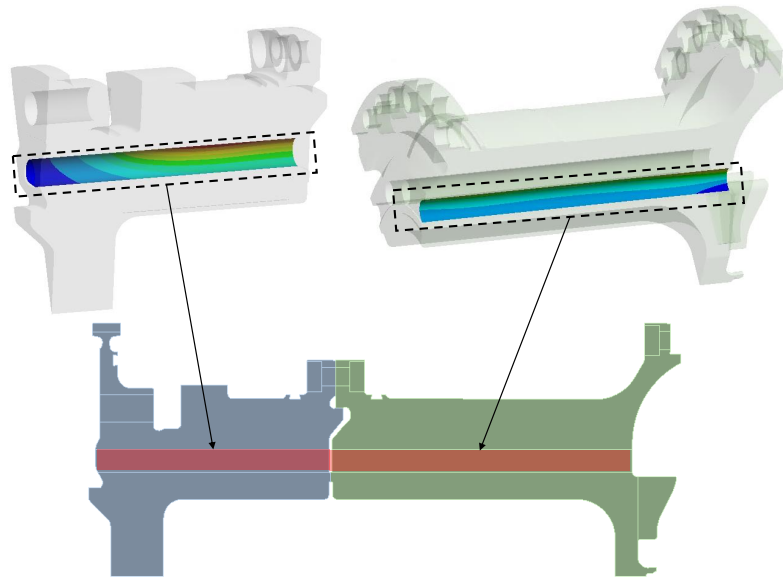


Figure 3.15: Dirichlet condition in air cooling channels

Dirichlet condition is also needed on turbine rim edges. In case of FR1500 turbine rotor, a blade shank separate turbine wheel rims from main exhaust gas flow. It means that this region is not in direct contact with the main flow. Anyway heat diffusion from blade through the shank affected temperature of the rim. In order to consider that contribution a 3D Steady-thermal simulation is needed also in this case. The output temperature distribution in these regions can be assigned to the 2D model (see Figure 3.16). The 3D analysis is comprehensive of blade portion. On the blade external faces convective coefficient and film temperature is derived using a similar approach to that used for turbine disks. The difference is that now thermodynamic variables belong to the main stream. Their evaluation is conducted using a software called AXSTREAM both in axial and radial direction to allow a more detailed analysis along the height of the blade. Also in this case results of AXSTREAM analysis was provided by the company.

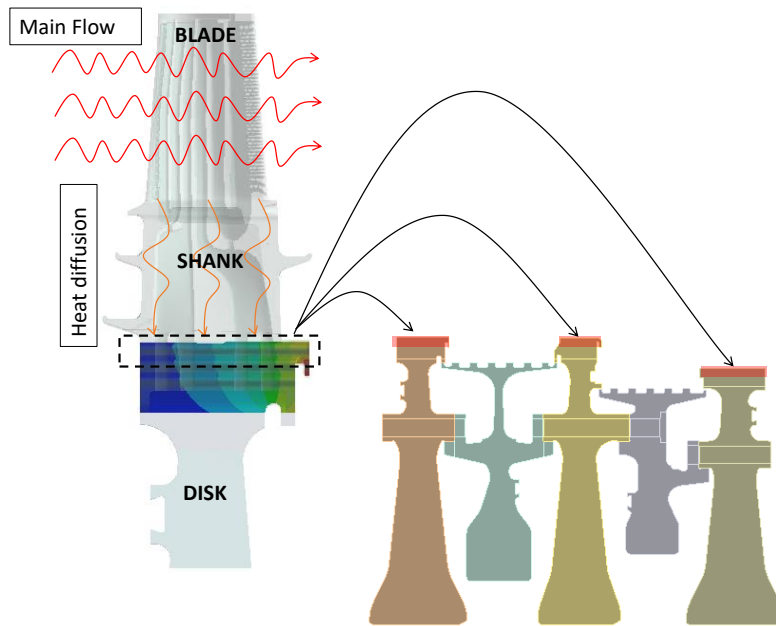


Figure 3.16: Dirchlet condition in TW's Rim

In the compressor blades there is not a shank portion. This means that the compressed air is in direct contact with compressor wheel rims and a Robin condition is applicable in that areas, represented by the highlighted edges in Figure 3.17.

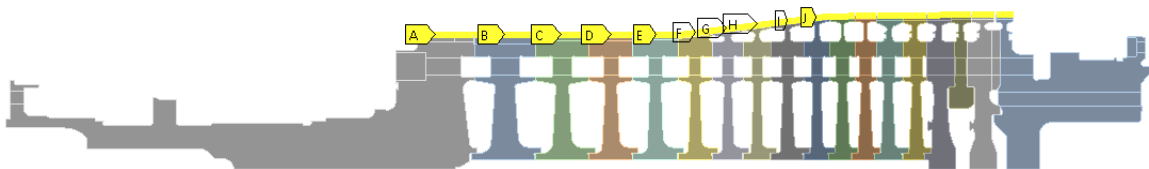


Figure 3.17: Dirchlet condition in CW's Rim

The last thermal boundary condition needs to be assigned in surface portions of FWD and AFT *Stub Shafts*, where radial bearings are located. A fixed temperature condition of around 90°C has to be assigned in that areas because of lubricant oil temperature. Locations are pointed in Figure 2.1.

### 3.3 Analysis results

Once simulation setup is completed, ANSYS software can run steady thermal and structural calculations in order to provide results at each node of the mesh grid. Obviously multiple number of simulations for each component of the turbine rotor, produce a huge amount of informations. The aim of this section is not to provide a detailed description of results for each component with a one-by-one approach, because it will be dispersive and useless. To ensure a better display effectiveness and for sake of brevity, the following pages will report analysis outputs of the entire rotor assembly and a focus on specific components, chosen as examples for common and particular features. Critical area, where concentration of high stresses are present, will be highlighted and most of the time different components share the same behaviour in these regions, because of similar loading condition and geometry.

#### 3.3.1 2D model entire rotor output

In figure 3.18 it can be seen the steady-state temperature map of the rotor. Because of NDA, values have been normalized dividing them by the maximum recorded temperature value. It is evident that the hottest zone is the one near the turbine wheel's rim and the labyrinth seals on the spacers tip. It is due to heat diffusion from turbine' blades and vanes, that are in direct contact with the high-temperature exhaust gasses of the main stream. As gasses expands though the turbine stage, they loose pressure and temperature. This is why the third stage TW has a lower temperature compared to the others. On the compressor side temperatures are globally lower and the distribution gradient is in the same direction of the compressed air axial velocity. Temperature rises quite linearly from C00 to C17 until it reaches the regime Compressor Discharged Temperature (CTD). Slightly the same one is the

initial temperature of the secondary air flow, drawn from C16 impeller in the AFT side and passing through C17 and DP cooling channels. In general it is clear how the combined action of heat convection and conduction affected the entire temperature distribution.

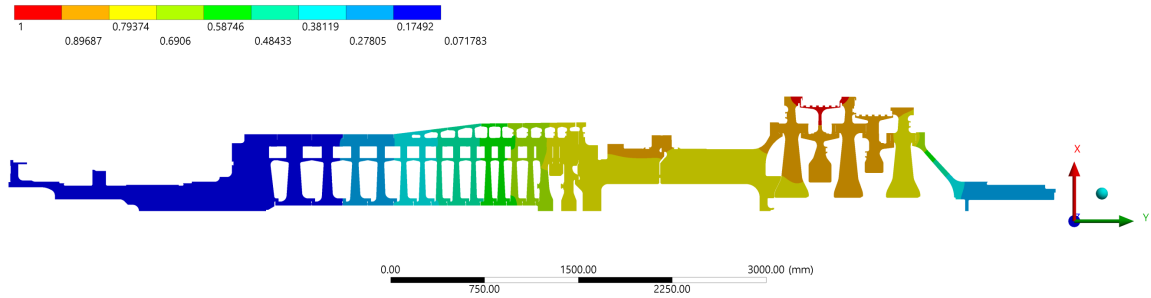


Figure 3.18: Steady-state temperature distribution

The Equivalent Hencky von Mises (HvM) stress is the resistance criteria used in static structural verification, so it is very important to be evaluated. The term equivalent in this criteria means that, even if two different points of the structure are defined by different values of the stress tensor, if they have the same HvM Stress, they are considered equivalent from the energy deformation point of view and so Yielding [14].

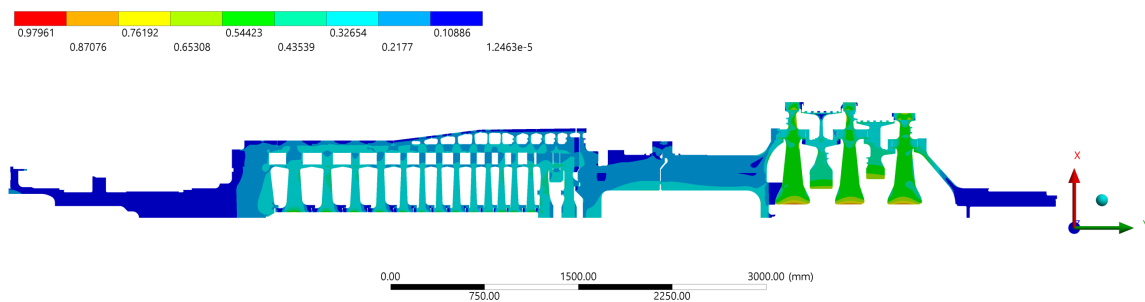
$$HvM = \sigma_{eq} = \sqrt{\sigma_x^2 + \sigma_y^2 + \sigma_z^2 - (\sigma_x\sigma_y + \sigma_y\sigma_z + \sigma_z\sigma_x) + 3(\tau_{xy}^2 + \tau_{yz}^2 + \tau_{zx}^2)} \quad (3.3.1)$$

In Figure 3.19 (a) it can be seen the HvM stress distribution. It is clear that high stress are concentrated in portions of the structural domain. For example in *borehole* proximity there is a prevalence of warm colors of the graduated scale. Also near fillet radii and, in general, where we have change of direction in the geometry, stresses are higher with respect to the average value. It is quite intuitive to foresee higher stresses on these regions and, also the Maximum Principle stress distribution in Figure 3.19 (b) suggests the same idea. The latter is the Maximum stress in one of the three

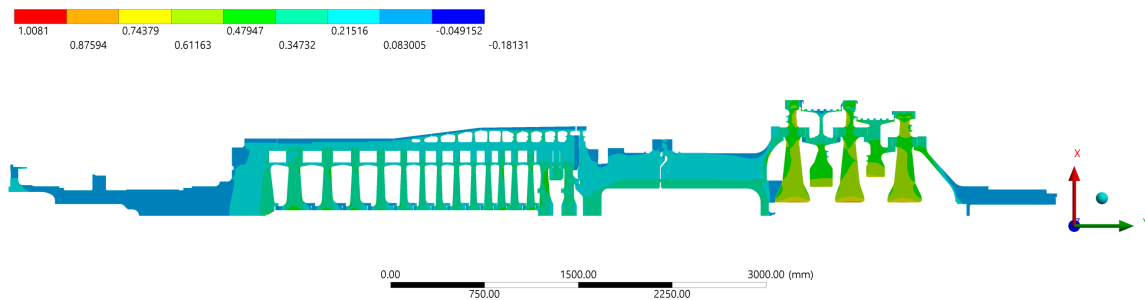
principle stress directions, which together form the Principal set of coordinates. If the stress tensor is rotated according to these coordinates shear stresses will vanish and only values along the main matrix diagonal will be different from zero.

Stresses have been evaluated keeping into account thermal loading and values have been normalized, dividing them by the Yielding Strength  $S_y$  at the given temperature of the turbine's disk alloy. In general all the results are  $\leq$  the yielding stress  $S_y$  of the more performing material.

Other specific area of the domain, where we have high stresses cannot be appreciated from these two images because a magnification would be necessary. Anyway they will be discussed in depth, later on in this paper.



(a) *Steady-state Equivalent Hencky von Mises stress distribution*



(b) *Steady-state Maximum Principal stress distribution*

Figure 3.19: HvM and Max. Princ. Stress distribution

According to thermal effect and centrifugal load rotor displacement will be both in axial and radial direction. Recalling the constraint applied to the structure on the left end side of the compressor assy (see section 3.2), the resulting gradient of total deformation distribution will be directed from the left to the right end side with a certain inclination with respect to the y-axis. At that light it is clearly visible in Figure 3.20, that the maximum total deformation is obtained at the tip of the third-stage rotating wheel TW3. In general the radial displacement on TW rims is higher because of intense centrifugal forces and high metal temperatures. Because of NDA, also deformations values have been normalized w.r.t. the maximum recorded displacement.

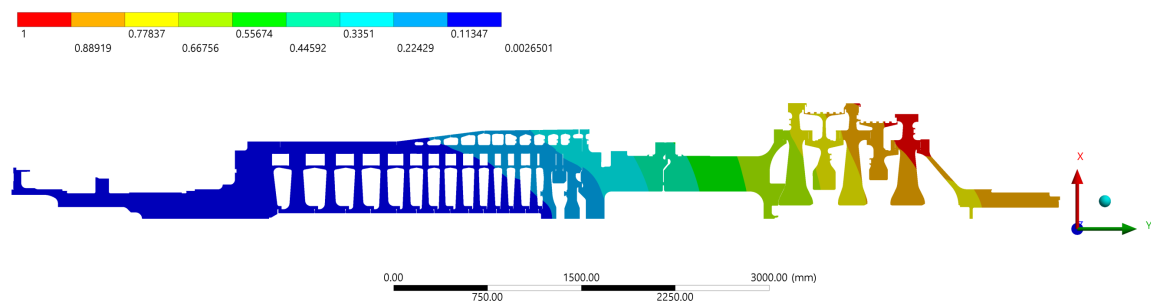


Figure 3.20: Steady-state total deformation distribution

### 3.3.2 2D Vs. 3D stress comparison on TWs WEB

As it was previously said, the 2D and 3D models are not completely independent. Their setup procedure is influenced by some results of both them. Recalling what was explained in section 3.3.1:

- The temperature distribution assigned on 2D-model TW rims is taken from 3D steady thermal output of each turbine wheel sub-models.

- The contact pressure assigned on 3D sub-models is taken from 2D steady structural output.

It means that the two models needs to communicate to each other and, to that end, it is important to verify results alignment in temperature distribution and in the expected principal stress coordinates. Experience in turbogas field suggests to compare stresses in y and z directions of the 2D-model reference system, namely Radial and Hoop stresses. In case of FR1500, this operation was performed looking results in the WEB line of turbine-side disks. WEB is a path defined by a vertical line, starting from the middle of *borehole* all the way to the end of axisymmetric-defined cross section. Turbine disks are chosen because they are the most critical components and needs to have a "preferential" treatment.

In Figure 3.22 Turbine wheel 1 TW1 is taken as example. All values have been normalized as before. In (a) it can be seen the comparison of temperature distribution among 3D and 2D model and the same distribution following the WEB path. In Figure 3.21 is clear that the two models have a good match along the the WEB line, because temperature curves, plotted against WEB length, are almost overlapped.

The hoop stress is represented in Figure 3.22 (b). The magnification image is used to highlight that highest values are near the *borehole* portion. Hoop stress in all the blade root slot portion is "zero", because here a plane stress assumptions was used to characterize the 2D model (see section 3.2.1). Indeed that portion is not counted in the WEB length range. Regarding the distribution along the latter, in Figure 3.21 (b) the curves are very similar so there is s good match. The only deviatory portion is the one in proximity of the *Through Bolt Hole* TBH. Here, the orthotropic material assumptions on the 2D model (see section 3.2.1), doesn't allow to obtain a real locally state of stress. Anyway it is not a problem, because specific geometrical feature are

not analysed looking to the 2D model results. They need to be effectively captured in the 3D sub-model analysis. Moreover The localized error doesn't affect the whole stress distribution, so that the overall solution is in line with what expected.

The radial stress distribution is clearly visible in the 2D model (Figure 3.22 (c)). Here in the magnification image, it can be observed how high radial stresses are concentrated near the fillet radii, instead in *borehole* external surface the radial stress is practically zero, because no external pressure is applied on the internal diameter of the disk. The comparison along the WEB path of radial stresses (Figure 3.21 (c)), reveals a great alignment among 2D and 3D model. No particular deviations are present near the TBH or on other portions of the specific domain.

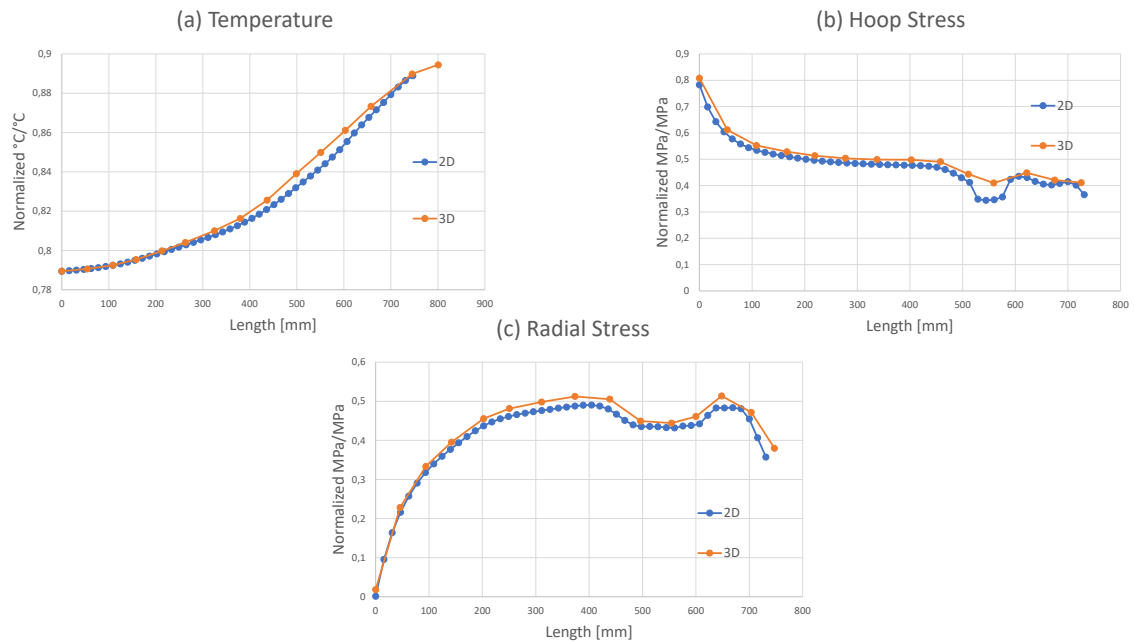
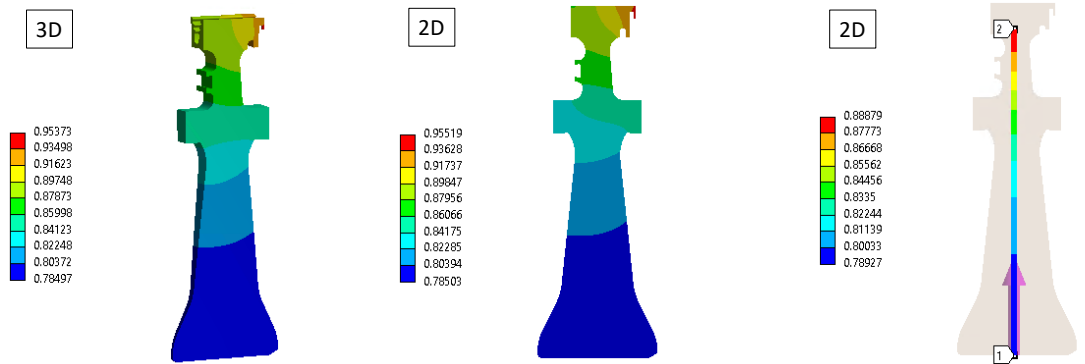
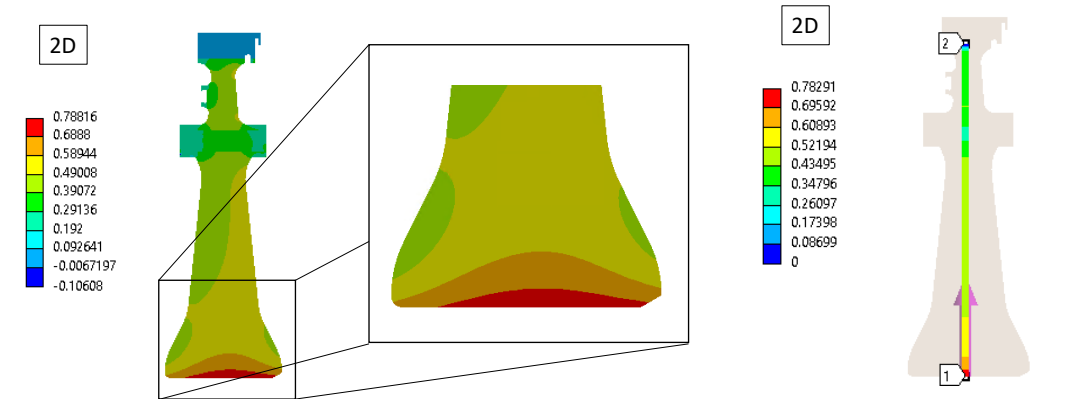


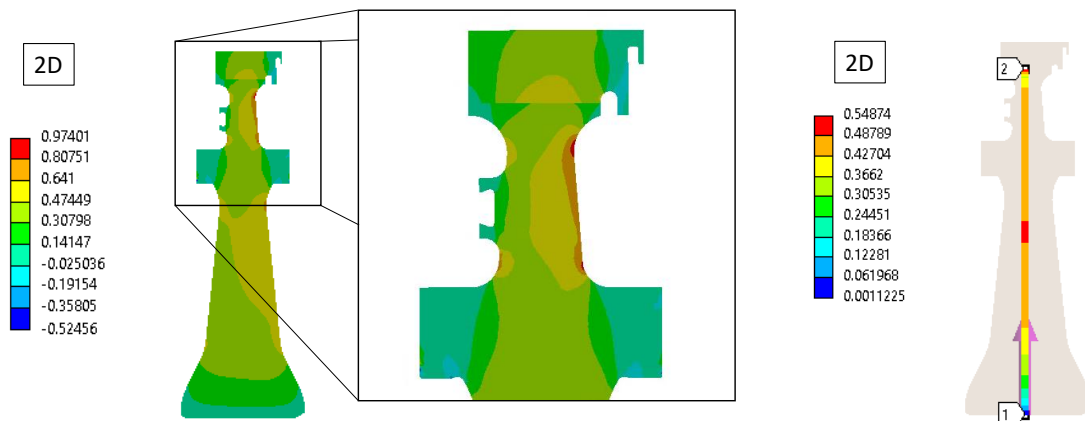
Figure 3.21: Temperature and stress distribution of 2D and 3D plotted against WEB length of TW1



(a) Temperature distribution



(b) Hoop stress distribution



(c) Radial stress distribution

Figure 3.22: Temperature and stress distribution on TW1 cross section and along WEB path

For sake of brevity all the other components from SP1-2 to TW3 are not represented, only their results are plotted in the following figures. All comments done for the TW1 case are valid also for TW2 and TW3, apart from temperature distribution on TW3 WEB. In this case heat conduction through contact regions gives a more evident contribution and it is not possible to take into account a priori that contribution in 3D model. It means that curves are more misaligned, as it can be seen in Figure 3.24(a) and the same happens in case of SP2-3 (see Figure 3.26). Despite it, the difference in temperature is restrained within a small range, so it does not affect stress distribution. SP1-2 and SP2-3 have not to support blade centrifugal force contribution, so the radial stress distribution is different from the TWs case. In Figure 3.25 and 3.26 (c), radial stress curves goes to zero as they reach *labyrinth seals* free surface. Moreover SP1-2 is free of orthotropic assumptions along the entire range of the WEB path. It means that in the hoop stress plot (Figure 3.25 (b)), there isn't any deviation due to it.

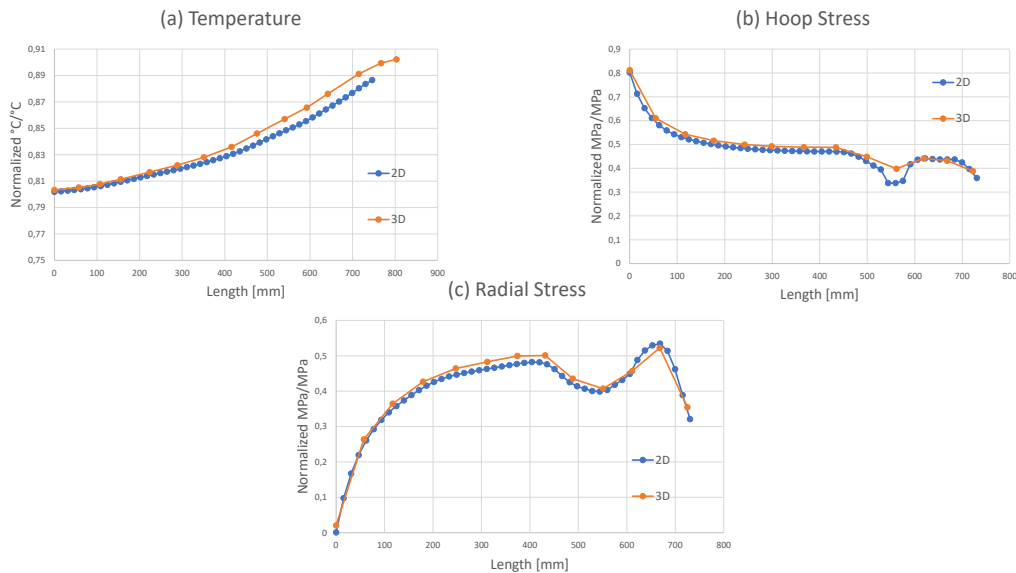


Figure 3.23: Temperature and stress distribution of 2D and 3D plotted against WEB length of TW2

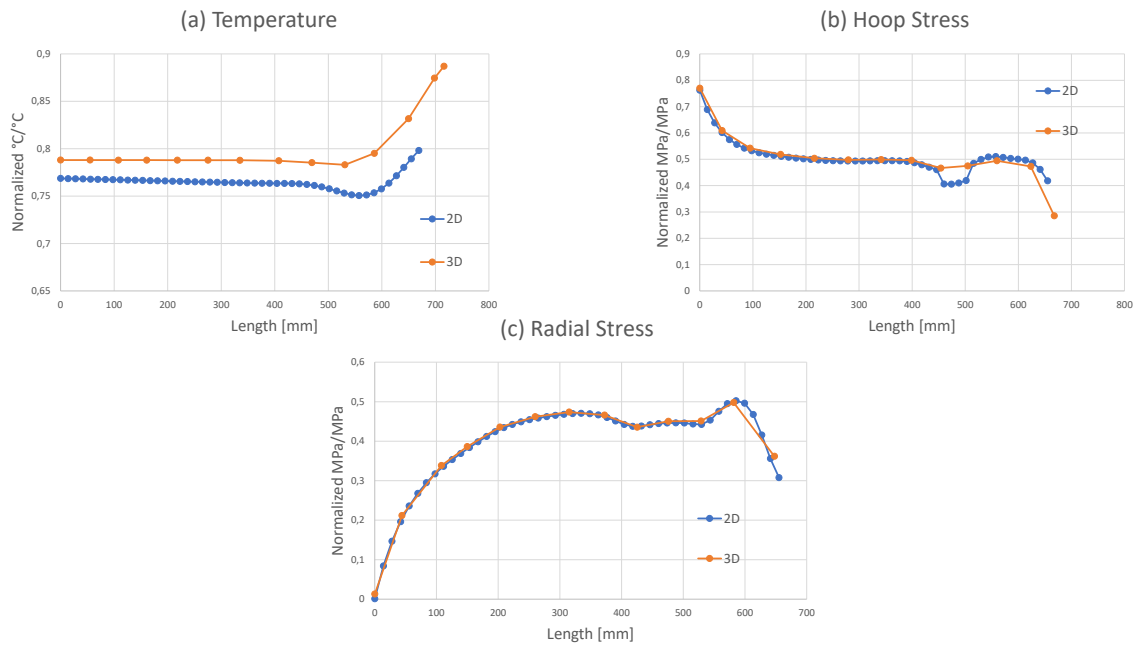


Figure 3.24: Temperature and stress distribution of 2D and 3D plotted against WEB length of TW3

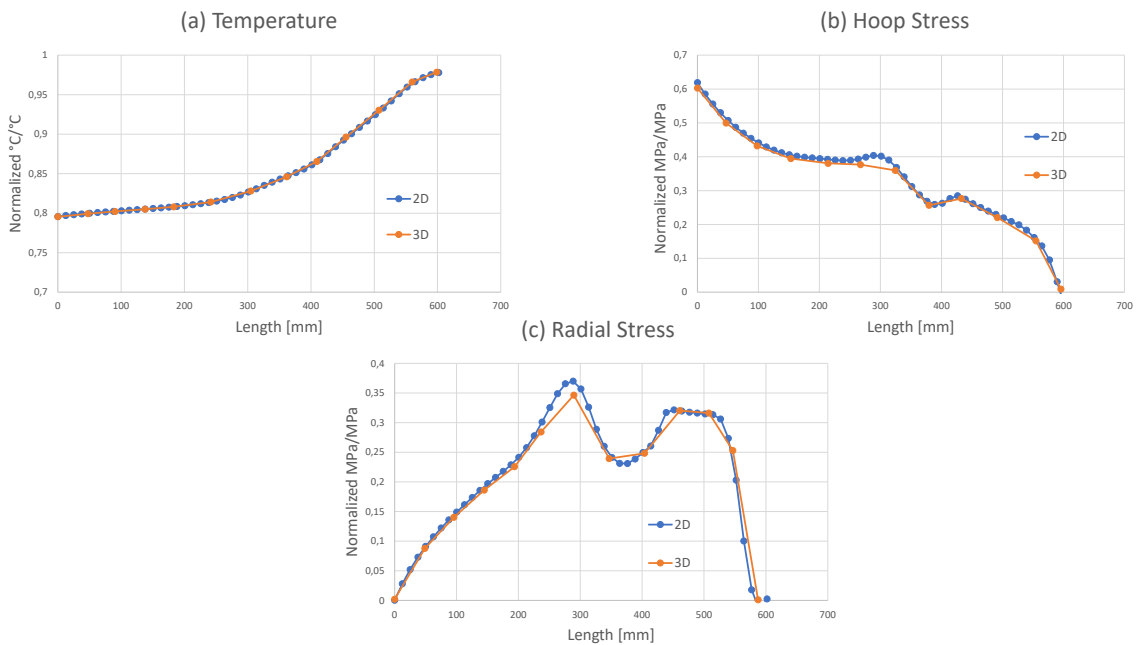


Figure 3.25: Temperature and stress distribution of 2D and 3D plotted against WEB length of SP1-2

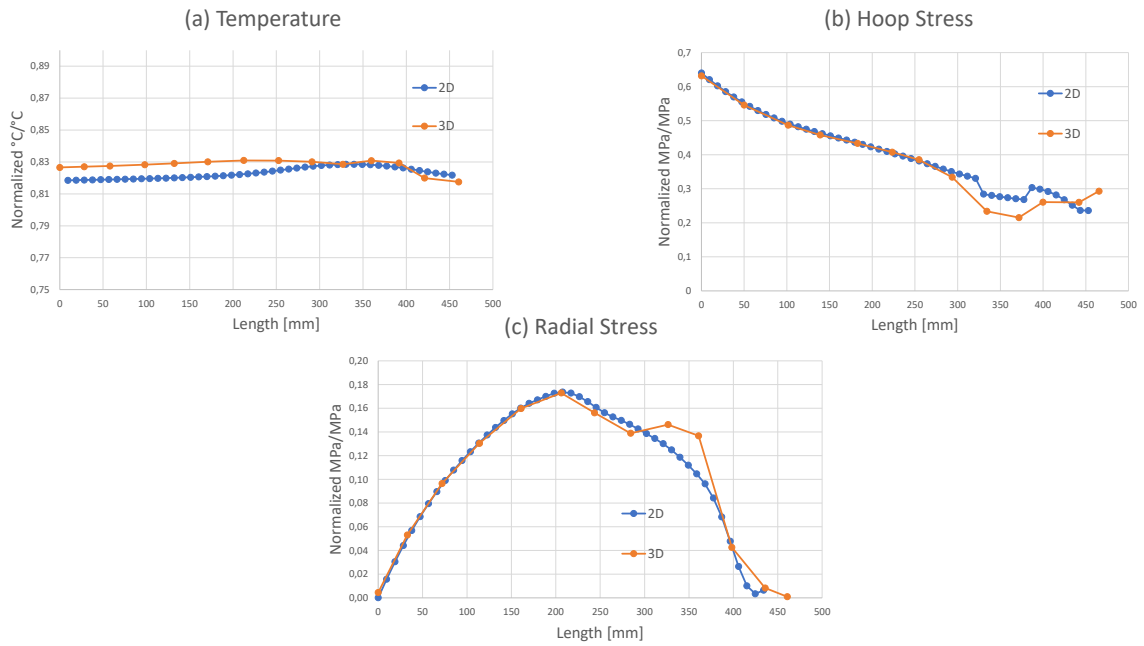


Figure 3.26: Temperature and stress distribution of 2D and 3D plotted against WEB length of SP2-3

In general, apart from particular reasons, the comparison provides a good feedback. Results of the two models are aligned, which means that 2D and 3D model can inter-operate, exchanging informations and sharing results.

### 3.3.3 Turbine side

The aim of this section is to provide a deeper insight on most critical areas of some turbine components, bringing results from 3D sub-models analysis. Like having a magnifying glass and pointing where we expect high stress concentration to appreciate distribution fashion and intensity. For sake of brevity only two components will be seen in detail. These are the turbine wheel TW1 and the spacer SP1-2, that can be of example for all the others. Components share similar geometry and similar loading conditions, so it is not a surprise that most of the time critical areas are the same for all of them. At that light, it will be useless and too dispersive to describe each component. Anyway critical regions for each of them will be post processed in the following chapter to consider the whole situation.

The compressor side 3D sub-models analysis is not less important, but after evaluation it was found that critical areas in compressor wheel CW are the same ones that have been studied in detail during 2D transient analysis. Other high level stresses, for example in *dovetail* region or in TBH proximity doesn't worry us so much. It means that in this chapter no information regarding the 3D steady-state analysis of compressor components will be given. All the discussion on that side will be left to the transient simulation part.

#### TW1

In order to have a better understanding, a sort of approximate legend is provided in Figure 3.27, to appoint regions of interest in the 3D sub-models. This turbine wheel needs two sub-models. The first one is a smaller cutting-angle slice, to capture the full radial range cross section comprehensive of the *fir tree* blade root slot and the other one is a bigger cutting-angle slice, to capture *Through Bolt Hole* and *Air slots*

geometries within a reduced radial range.

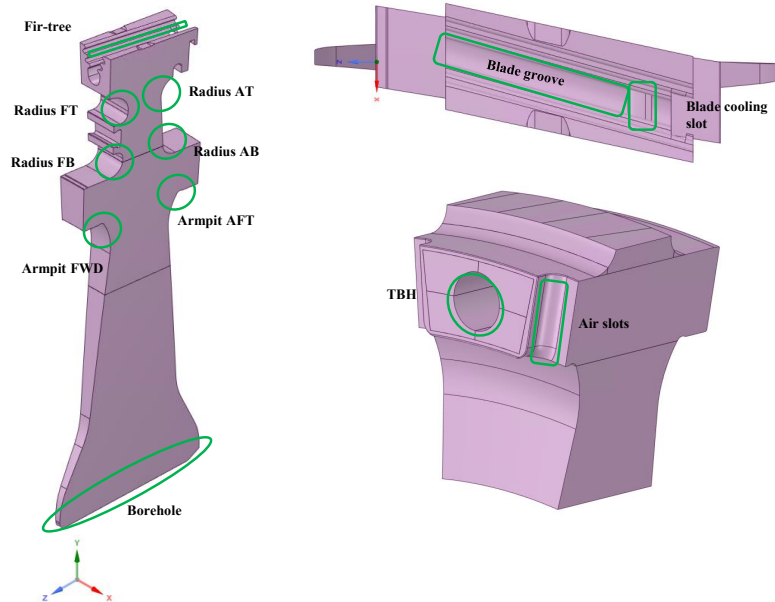


Figure 3.27: TW1 legend on 3D sub-models

The equivalent Hencky von Mises stress distribution on both sub-models is portrayed in figure 3.28. Values have been normalized with the same approach as before.

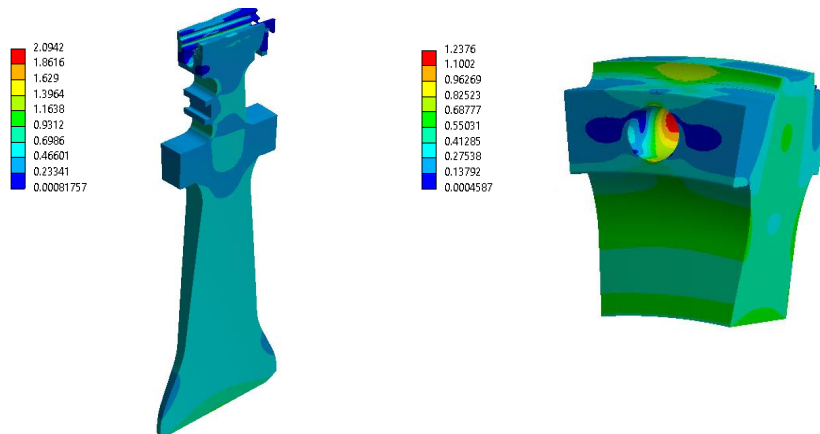


Figure 3.28: Equivalent Hencky von Mises stress distribution on TW1

As it was anticipated in the previous section, fillet radii are locations where the change of direction in the geometry causes a concentration of stresses. In Figure 3.28 it cannot be appreciated, so we propose as example an enlarged image of stress distribution on free surface of *Radius AB* and *AT* in Figure 3.29. In the same figure it is also highlighted the stress map on *Borehole* surface, which is one of the most important location of the disk to keep safe.

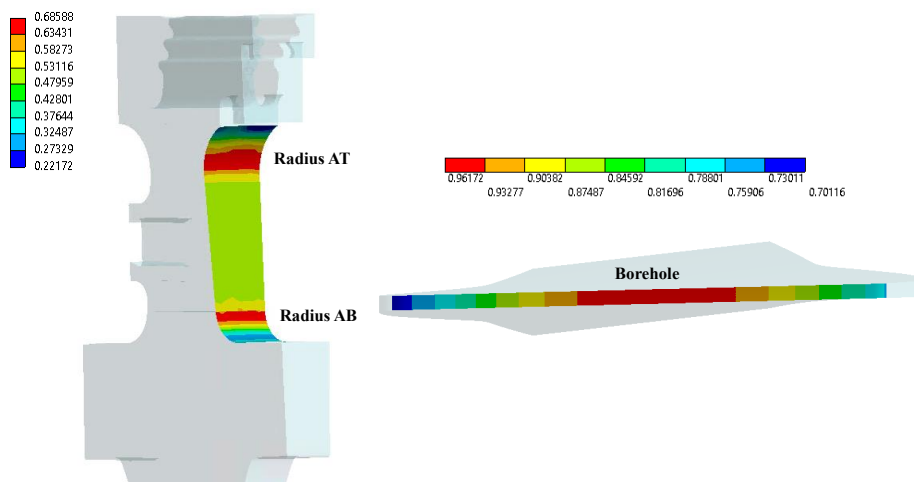


Figure 3.29: Radius AB, AT and Borehole HvM stress distribution

Despite the concentration of stresses in these regions, intensity is not exceeding the Yielding strength value  $S_y$ . Anyway in Figure 3.28 both sub-models suggests that somewhere in the structure is happening. Regarding the first slice, this condition is reached in the *Fir tree* region and in the *Blade cooling slot*. The *Fir tree* is portrayed in Figure 3.30. Here it can be seen that areas with very high values are quite restricted, as in the magnification box. Deeper investigation in that area reveals that isolated red and yellow thin "strips" are the result of irregular pressure distribution in contact active planes with the blade root, that creates "singularities". The latter cannot be completely avoided, because they depends on mesh size and grid arrangement. Sometimes they can be reduced refining the mesh or defining a different contact

behaviour, but for our purpose is enough to ensure that these high values are not physical, but depends on computational errors.

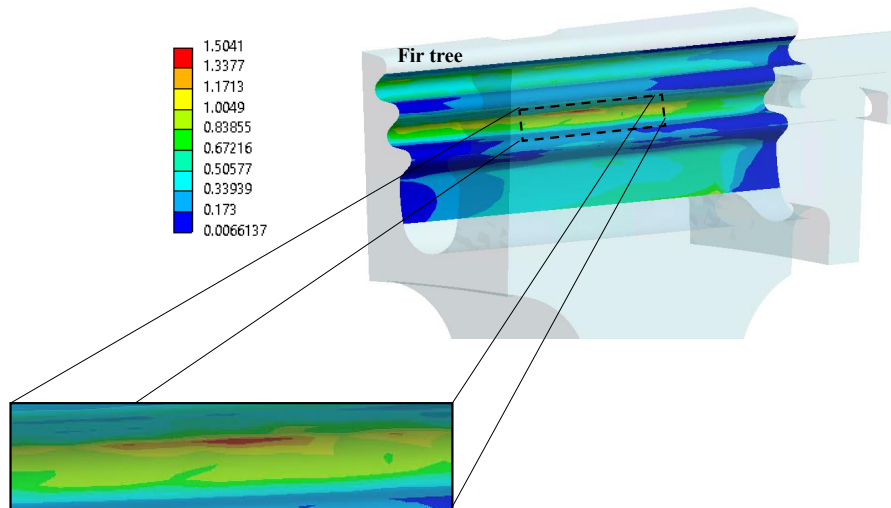


Figure 3.30: Fir tree HvM stress distribution

The *Blade cooling slot* is a sort of elliptical hole obtained, milling the TW slot. His design purpose consists to carry cooling air inside the blade internal cooling channels, through appropriate holes in the bottom part of the blade, just below the *shank* portion. This strange geometry introduces a sudden change of direction of  $90^\circ$  that induces a concentration of stresses in a very restricted area of the hole edge. Here intensity reaches a very high peak value as it can be seen in Figure 3.31, highlighted also in a magnification box. In this case, with a deeper evaluation it was concluded that this result is physical. The intensity value slightly depends on mesh size and on sharp edges that can be somehow rounded with a feasible radius, but in essence this is a critical region that could bring to a crack formation and needs to be further analysed. The last Critical region of TW1 is the *Through Bolt Hole*. Stress intensification is induced by the lack of material in this region and distribution fashion is influenced by both radial and hoop stresses. High stresses in this case are concentrated in a wider

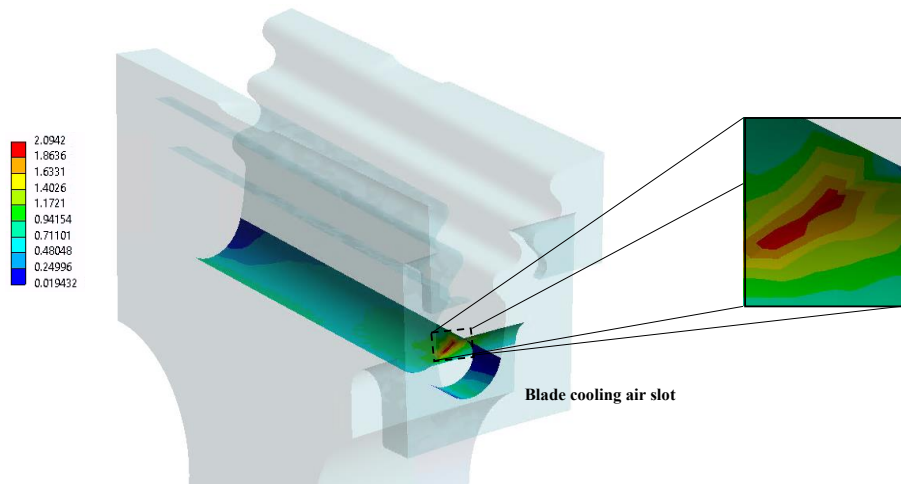


Figure 3.31: Blade cooling slot HvM stress distribution

circular area (see Figure 3.32). Despite values are less worrying, further analysis are also needed in this case to assure safety operating condition.

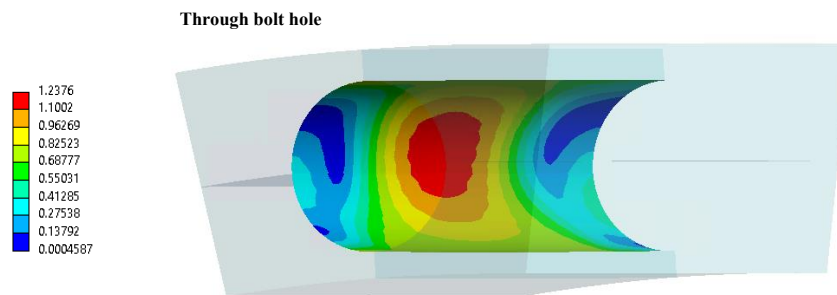


Figure 3.32: Through Bolt Hole HvM stress distribution

**SP1-2**

In the same way of TW1, also for SP1-2 3D sub-model geometry a legend is provided in Figure 3.33, to have a better grasp of what we are talking about. In this case only one slice with a wider cutting-angle is needed to describe each feature of the turbine spacer. In Figure 3.34 The resulting HvM stress distribution.

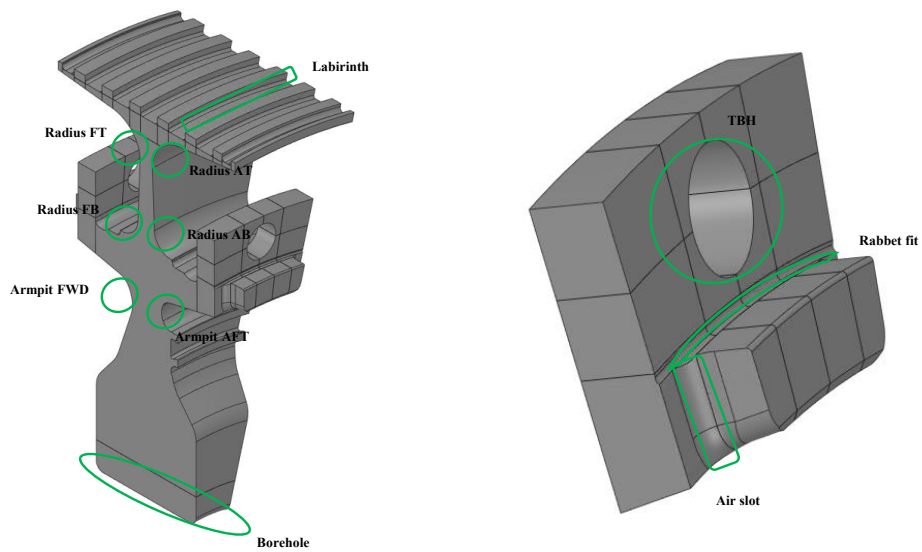


Figure 3.33: SP1-2 legend on 3D sub-model

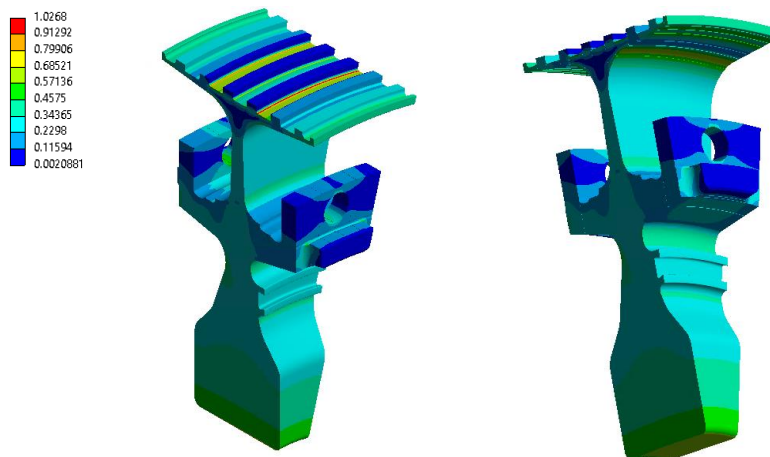


Figure 3.34: Equivalent Hencky von Mises stress distribution on SP1-2

The graduated color bar in figure 3.34 suggests that in this case the overall stress level is lower than for turbine wheels. This is partially due to the absence of blade centrifugal load on the tip of the disk. The most loaded regions are the TBH and the *Labyrinth seals*.

Hoop stress in TBH is the main actor for the stress concentration on the tip of the hole. Anyway, as it can be observed in Figure 3.35, peak stress is lower than the half of  $S_y$  at the considered temperature, so this is not a critical region. Differently on *Labyrinth seals* values reaches the Yield Strength in a red-coloured thin strip, lying along the circumferential coordinate (see Figure 3.35). Further evaluations in that area reveals that the cause has to be attribute to the constraint contact with TW2 at the right extreme of the *labyrinth* geometry. This, according to radial deformations, induces a bending moment in that region and the intensification factor in the change of direction makes the rest. See Figure 3.36 to appreciate the deformation shape.

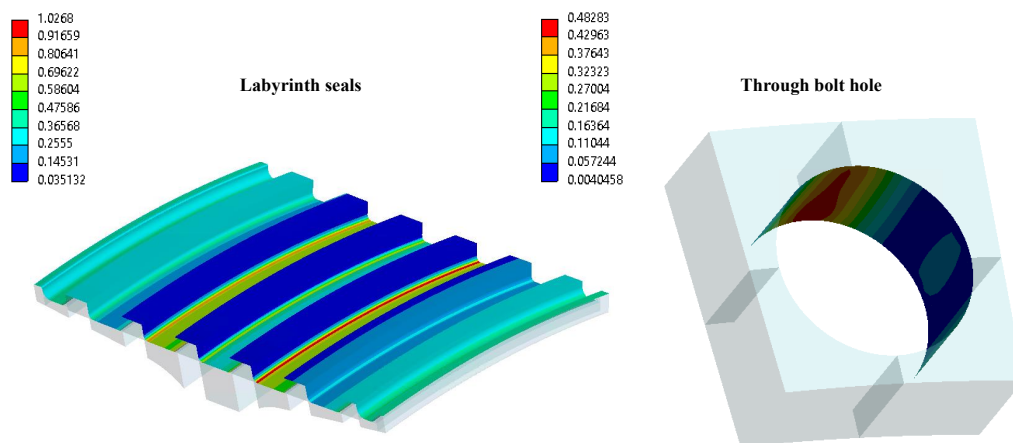


Figure 3.35: TBH and Labyrinth seals HvM stress distribution

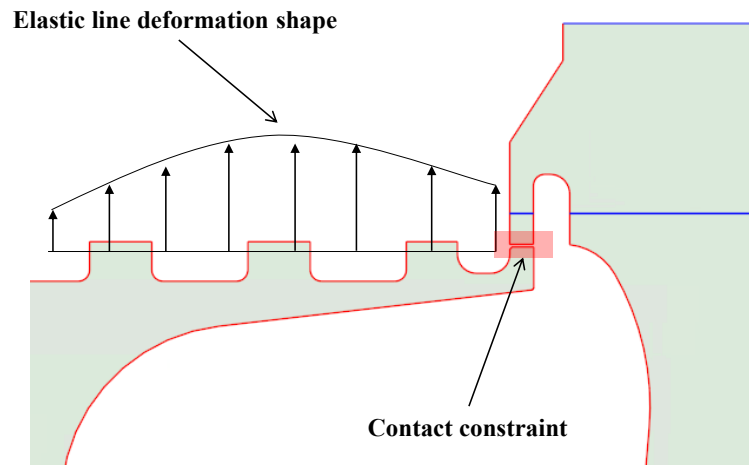


Figure 3.36: Deformation shape sketch of right-end side of Labyrinth seals

### 3.3.4 Classification of stresses

What was described in the previous section is the Equivalent von Mises stress result, considering both mechanical and thermal loads. Anyway, according to *Ethos Energy* design criteria approach, stresses must be classified in order to be post processed. The classification was done distinguishing which stress contribution is due to which cause. The fortuity relation makes it possible to verify the stresses according to a systematic method, which has been shown to guarantee a robust verification process. We distinguish stresses among the following items:

- **Pm**: Primary membrane stress. This is defined as the average cross section stress induced to satisfy the external equilibrium forces.
- **PL**: Primary local stress. This quantity is defined as the local cross section stress induced by only mechanical external forces, like centrifugal load, contact pressure and bolt's pre-load.
- **Q**: Secondary stress contribution. This is the neglected contribution of the

previous case, not ascribable to any mechanical force. Indeed this quantity depends only on thermal load effect.

- **F**: Peak stress contribution. It consist in the peak value of stress, observed in particular areas. In sudden change of direction in a component geometry, like curves or sharp edges, it is observed an amplification of average cross section stress, due to a concentration factor. The latter is usually reported in literature as  $K_t$  coefficient. We have already highlighted this phenomena in the previous section, when we described stress concentration in particular regions.

Regarding the membrane stress, it is evaluated looking to hoop stresses along the WEB path. As it was previously described in section 3.3.2, hoop stresses are plotted against WEB line length of each component, so to obtain a stress curve as function of WEB coordinate. Then an average value is extracted integrating the function over the length range and dividing it by the latter.

In general Primary stresses are inclusive of the membrane contribution, so we refer to them as they are (**Pm+PL**). The Secondary stresses are not evaluated apart from the rest, so the other group consists of Primary + Secondary stresses, namely (**Pm+PL+Q**). Following this reasoning Peak stress should be an all inclusive value (**Pm+PL+Q+F**) and a typical output of a stress analysis performed with a FEM model is this one.

Being the acceptability of the Primary + Secondary stress quite important to guarantee a permanent deformation avoidance, they have to be drawn out from the whole reading. Since there is a strong correlation between the bending moment and the displacement second order derivative, this can be done taking the maximum value of a second grade interpolation along the resistant cross section. Where it is difficult

to define a precise cross section, a rough method to neglect  $F$  contribution could be taking the average value of recorded stresses over the surface of interest. Where  $F$  contribution is not present a priori, since no-concentration factor is affecting stress distribution, the value can be taken as given from output result.

The same approach is followed to evaluate Primary stresses apart from all the rest, but we need to neglect  $Q$  contribution. To perform this task in ANSYS software is very easy. It is sufficient to suppress Thermal load in the boundary condition and it is done avoiding to import steady thermal output analysis in the structural one.

### 3.3.5 Neuber's rule

The performed FEM simulations are based in linear elastic behaviour. It means that the software based stress calculations following the Hooke's law:

$$\sigma = E(T) \cdot \varepsilon \quad (3.3.2)$$

where  $E$  is a function of temperature. In reality, tensile-tests in ductile materials as steel, demonstrates that samples exhibit an elastic-plastic behaviour. It means that, the linear assumption at a certain point is no more valid. Yielding strength of ductile material is defined as the resulting tensile stress obtained at 0.2% of permanent deformation. From that point on, if we continue to pull the test-sample we will observe a non-linear behaviour in which a certain amount of cumulated energy is consumed to move dislocations in the crystalline lattice. It causes stress release, according to an increase in permanent deformation. This means that stress-strain ( $\sigma - \varepsilon$ ) curve slope progressively decreases. Practically, according to Ramberg-Osgood theory, from  $S_y$

on, the Eq. 3.3.2 is substituted by the following relation.

$$\sigma = S_y + K_y \varepsilon_p \frac{1}{M_y} \quad (3.3.3)$$

where  $\varepsilon_p$  is the amount of plastic (permanent) deformation. Ones  $K_y$  and  $M_y$  parameters are known a model is provided [5]. At that light, is easy to understand that when peak stresses results overcomes  $S_y$  value they need to be corrected (reduced) following the real elastic-plastic curve. Multiple approaches are available in literature to perform this computation, but according to our design purpose the **Neuber's rule** is the more suitable one. The rule states that stresses can be re-conducted on the real  $\sigma - \varepsilon$  curve, following an elastic energy equivalence, so:

$$\sigma \cdot \varepsilon = const. \quad (3.3.4)$$

In Figure 3.37 it can be seen how the elastic-plastic real stress is the intersection between the base material Ramberg-Osgood curve and the Neuber hyperbolic one.

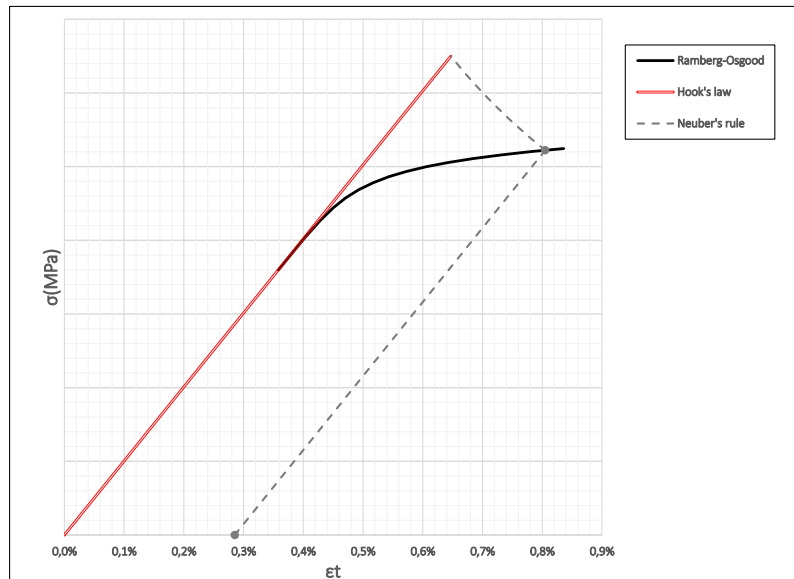


Figure 3.37: Neuber's rule

### 3.4 Static structural verification

#### 3.4.1 Design criteria curves

Once classified as in section 3.3.4, stresses must be compared with allowable ones. In figure 3.38 are plotted against temperature all the limiting curves that are used in static structural post processing.  $S_u$  and  $S_y$  are respectively the Ultimate strength

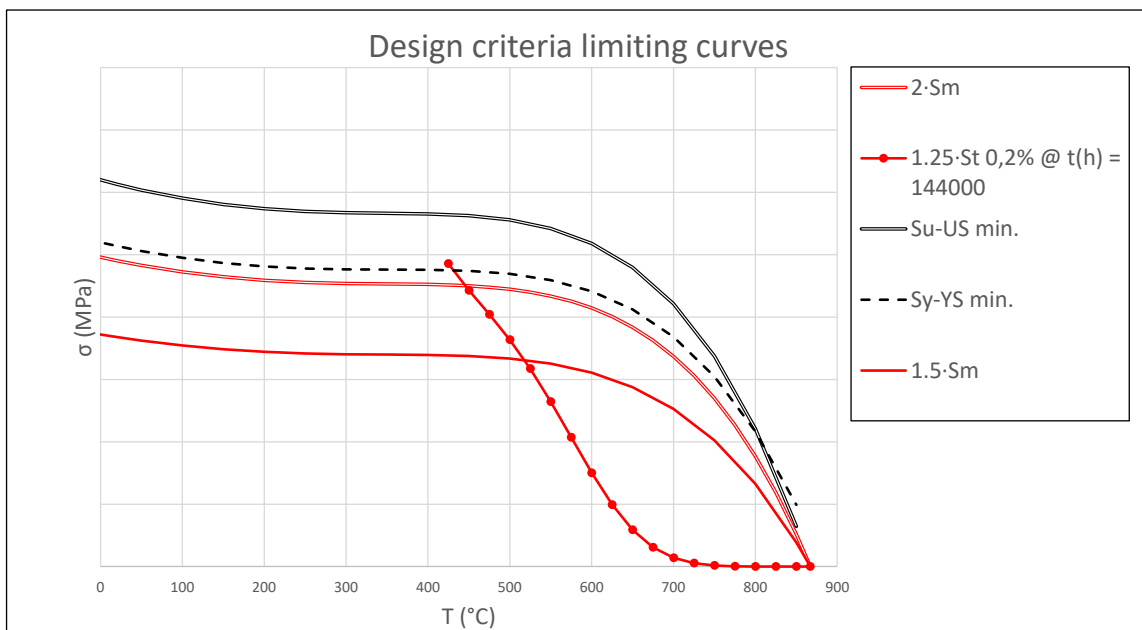


Figure 3.38: Design criteria allowable stresses

and the Yielding strength curves, extrapolated from data test in order to ensure 99% probability and 95% confidence.

$S_m$  is defined as  $MIN\left(\frac{S_u}{2.5}; \frac{S_y}{2}\right)$  and is used to check allowable membrane strength at the considered temperature.

$S_t$  is the creep allowable stress curve against temperature. *Creep* is defined as the failure that occurs in a component subjected to a certain static load and temperature level for a certain time, generally expressed in hours. Generally the creep curve is plotted against a parameter, called Larson Miller parameter, which is able to keep

into account a given temperature  $T$  and time  $t$  in a unique variable  $LM$ , thanks to the following empirical relation:

$$LM = \frac{(T(C) + 273.15)}{1000} [20 + \log(t)] \quad (3.4.1)$$

In our case the OEM service life recommends to do not overcome 144000 Factored Fired Hours (FFH), that is the equivalent endurance limit in steady state operating condition for which the OEM has designed the FR1500 turbogas rotor. Indeed, fixed the time at  $t(h) = 144000$  a unique creep value can be obtained at different temperatures, so to build the spotted curve in Figure 3.38. The limit is not the final rupture but the yielding, that's why 0.2% is indicated in the legend.

- Membrane stresses have to be  $\leq S_m$  and  $\leq S_t$
- Primary stresses have to be  $\leq 1.5 \cdot S_m$  and  $\leq 1.25 \cdot S_t$ , but sometimes values overcome  $1.5S_m$  curve, so  $2 \cdot S_m$  is always reported for reference.
- Primary + Secondary stresses have to be  $\leq 2 \cdot S_m$  and  $\leq 1.25 \cdot S_t$
- For peak stresses the  $S_t$  curve is no more necessary, but we need to add  $S_y$  and  $S_u$  curves for reference, because often stress intensification can overcome these values. Moreover, as it was explained in the previous section, the linear elastic model of FEM simulations tends to overestimate peaks of stress, so verification is needed before and after Neuber's reduction.

### 3.4.2 Post-processing results

The aim of this section is to provide the static structural verification of turbine components. For sake of brevity, only the most critical regions will be presented in that discussion and, for the same reason, not all the acceptance plots for each component will be provided. TW1 and SP1-2, carrying on section 3.3.3, are taken as example. Results on critical areas of other components will be briefly discussed and collected in a summary table. For completeness, in **Annex** of the present paper, all 3D geometries legend are listed.

All peak stresses, apart when specified, are multiplied by a coefficient factor of 1.2. This value, based on past experience and experimental evaluations, is an estimated factor to keep into account any transient intensification of stresses during rotor start-up or shut-down. In some cases this factor returns a preliminary result, pending a more precise verification by a 2D transient simulation, which will be discussed in the following chapter. Other times it is not possible to capture particular geometrical features (e.g. TBH, Blade cooling slots) with a 2D analysis, then approximated results are considered valid, because the 20% incipient is, most of the time, a conservative approach. In firm's routine 3D transient analysis are almost avoided. That's because it is quite difficult to set them and they are very time-consuming.

Bacause of NDA numerical values have been normalized as before. AFT *Stub Shaft* AS and *Distance Piece* DP are made of a less performing steel alloy. It means that  $S_y$  value used to normalize results is different, but in any case material specifications cannot be released.

**Membrane stress**

Membrane stress for each turbine disk is computed as the average hoop stress along the web path. Doing so, we obtain a sort of mean stress induced to satisfy external equilibrium forces and it is evaluated to assure general robustness of the structure. Resulting values can be appreciated in Figure 3.39, where it is evident that SP1-2 and SP2-3 are well within the acceptable limits. TW1 and TW2 are quite overlapped to the allowable stress  $S_m$  at the given temperature and TW3 is slightly above the namesake curve. Anyway the latter is still acceptable, pending a more precise structural evaluation.

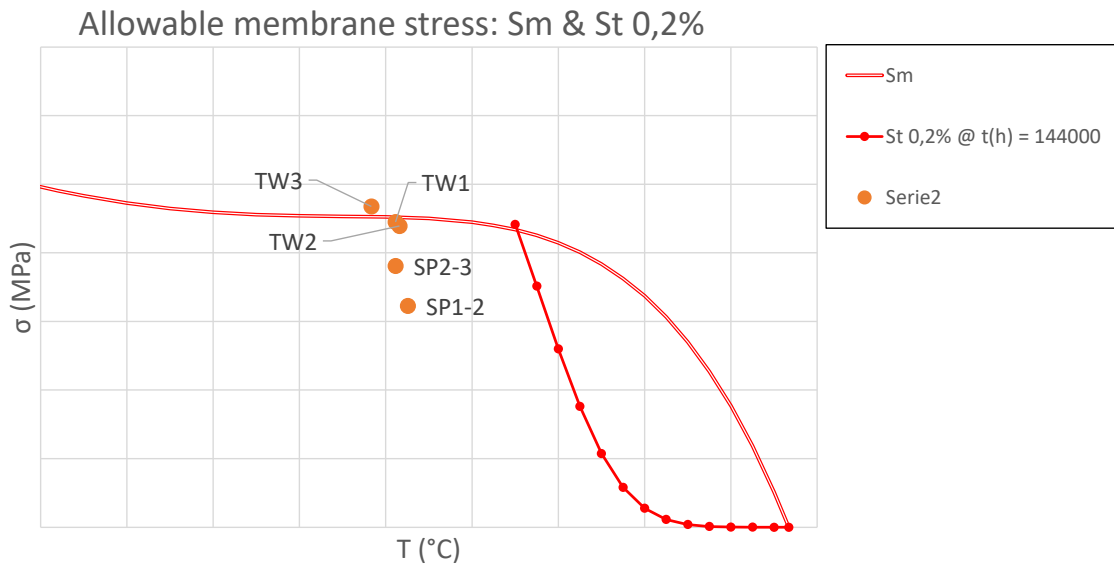


Figure 3.39: Membrane stress acceptance plot (All turbine disks)

**TW1**

Primary stress evaluation reveals that *Radius* FB, FT and, in particular, *Borehole* values are above the  $1,5S_m$  curve, but below the  $2S_m$ . Adding secondary stress contribution, *Borehole* is quite near the  $2S_m$ , but it is still acceptable.

Peak stresses on TBH, *Fir tree*, *Blade cooling slot* and *Borehole* are pretty high. Indeed, even reduced following the Neuber's rule, the first three remain above the  $S_y$  curve, especially *Blade cooling slot*. What has been described is summarized in the following table and plots (see from Figure 3.40 to 3.43).

TW1						Actual values		Extra Load		Neuber's reduction Stress; Mpa/MPa
Type of stress	Codification	Allowable Stresses		Temp; °C/°C	Stress; MPa/MPa	Coeff trans	Stress; MPa/MPa			
<b>Primary Stress</b>										
Primary Stress	Radius FB	HvM	Pm (or PL) + Pb	1.5Sm	1.25 St	0,89	0,80	1,0	0,80	
Primary Stress	Radius FT	HvM	Pm (or PL) + Pb	1.5Sm	1.25 St	0,92	0,78	1,0	0,78	
Primary Stress	Bore Hole	HvM	Pm (or PL) + Pb	1.5Sm	1.25 St	0,82	0,93	1,0	0,93	
<b>Primary + Secondary Stress</b>										
Primary + Secondary Stress	Bore Hole	HvM	Pm (or PL) + Pb + Q	2Sm	1.25 St	0,82	0,96	1,0	0,96	
<b>Peak Stress</b>										
Peak Stress	Fir Tree	HvM	Pm (or PL) + Pb + Q + F	Sy		0,98	1,53	1,0	1,53	1,09
Peak Stress	TBH	HvM	Pm (or PL) + Pb + Q + F	Sy		0,89	1,24	1,2	1,49	1,07
Peak Stress	Bore Hole	HvM	Pm (or PL) + Pb + Q + F	Sy		0,82	0,96	1,2	1,16	1,01
Peak Stress	Blade Cooling Slot	HvM	Pm (or PL) + Pb + Q + F	Sy		0,95	2,23	1,2	2,67	1,16

Figure 3.40: Summary table results (TW1)

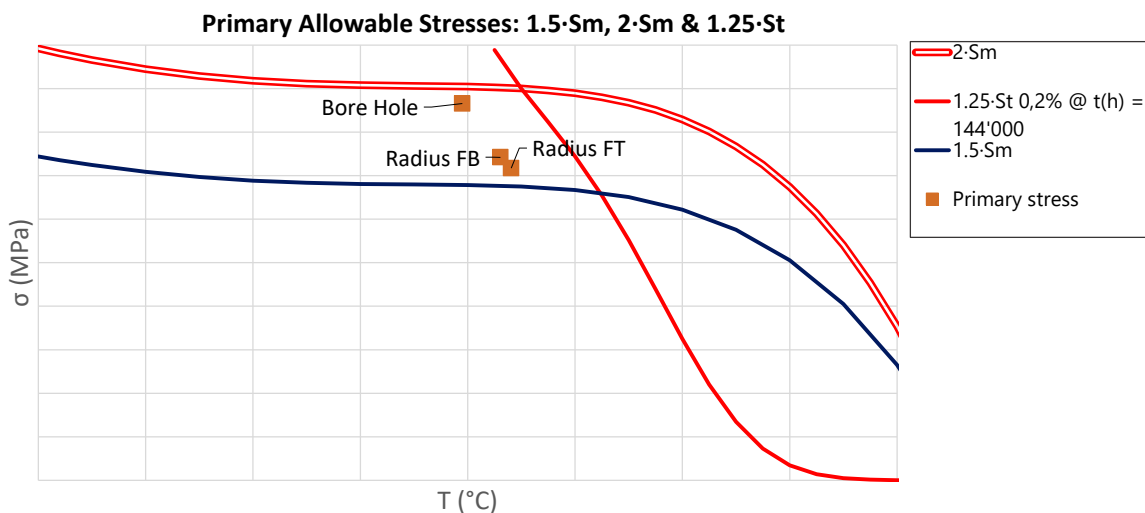


Figure 3.41: Primary stress acceptance plot (TW1)

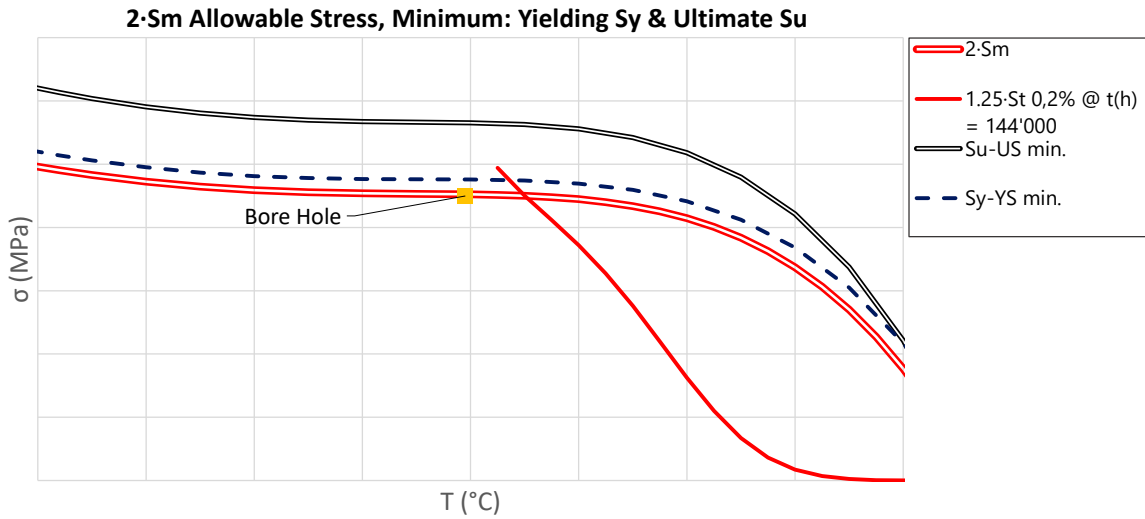


Figure 3.42: Primary + Secondary stress acceptance plot (TW1)

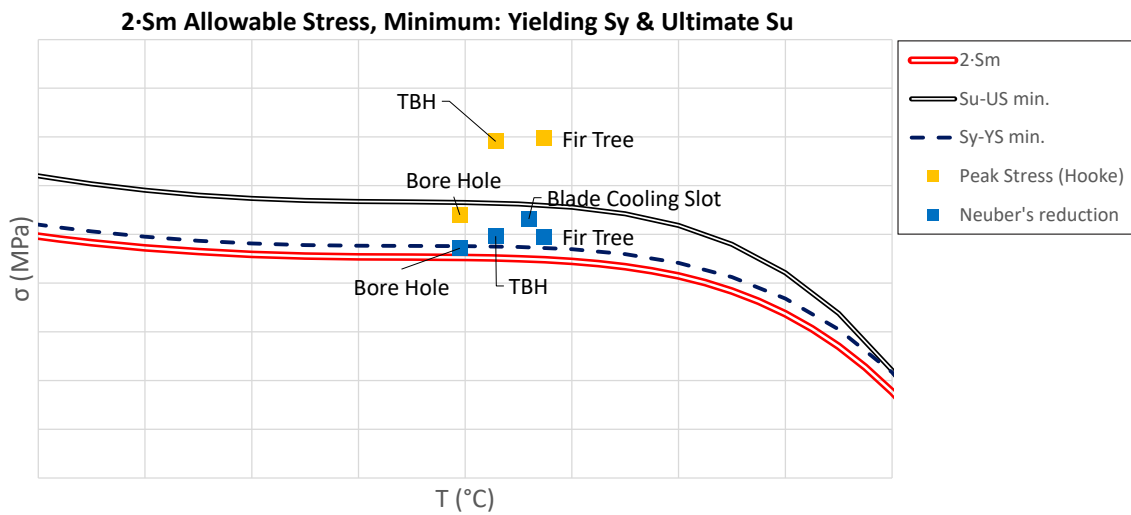


Figure 3.43: Peak stress acceptance plot (TW1)

The rest of the regions indicated in the legend on Figure 3.27 are well within the allowable stresses, so they are not reported.

**SP1-2**

TBH and *Labyrinth seals* are slightly above the  $1,5S_m$  in the Primary stress evaluation. Looking to the Primary + Secondary chart *Labyrinth seals* is very closed to the creep curve, but is still below it, so it is able to accomplish a few more than 144000 equivalent hours until permanent deformations arises. Peak stress in the same region, considering the intensification factor, is high, but with Neuber's reduction it can be observed that value reaches almost  $S_y$  magnitude at the given temperature.

SP1-2						Actual values		Extra Load		Neuber's reduction
	Evaluation	Type of stress	Codification	Allowable Stresses		Temp: °C/°C	Stress: MPa/MPa	Coeff trans	Stress: MPa/MPa	Stress: Mpa/MPa
<b>Primary Stress</b>										
Primary Stress	TBH FWD	Average	HvM	Pm (or PL) + Pb	1.5Sm	1.25 St	0,88	0,80	1,0	0,80
Primary Stress	Labyrinth Seal #5	Average	HvM	Pm (or PL) + Pb	1.5Sm	1.25 St	1,04	0,75	1,0	0,75
<b>Primary + Secondary Stress</b>										
Primary + Secondary Stress	Labyrinth Seal #5	Average	HvM	Pm (or PL) + Pb + Q	2Sm	1.25 St	1,04	0,78	1,0	0,78
<b>Peak Stress</b>										
Peak Stress	Labyrinth Seal #5	Peak	HvM	Pm (or PL) + Pb + Q + F	Sy		1,04	1,04	1,2	1,25

Figure 3.44: Summary table results (SP1-2)

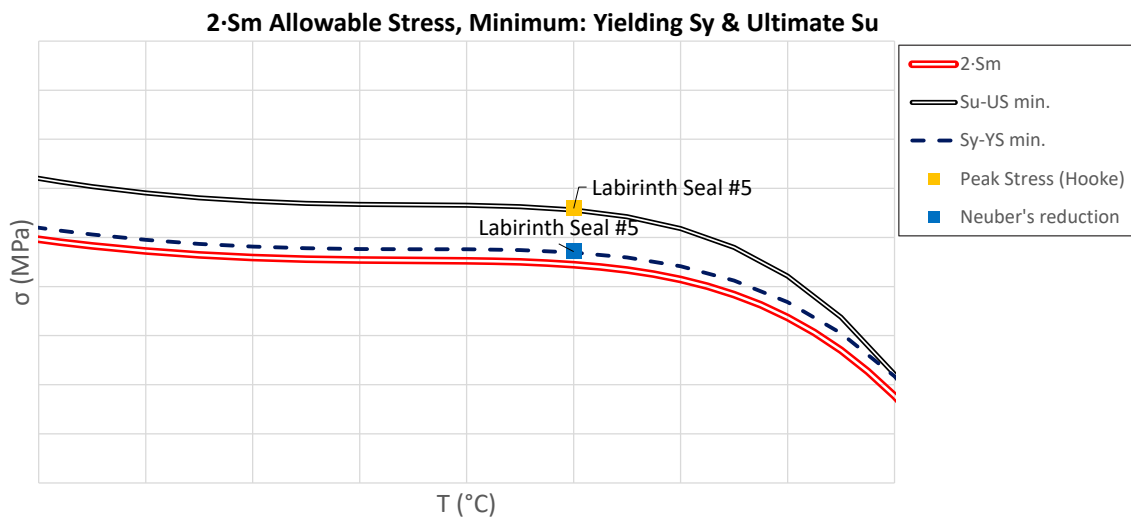


Figure 3.45: Peak stress acceptance plot (SP1-2)

As it was done for TW1, results are collected in the table 3.44 and only Peak stress

plot is provided in Figure 3.45. The other the regions indicated in the legend on Figure 3.33 are well within the allowable stresses, so they are not reported.

### The remaining turbine components

Turbine wheel TW2 situation is quite similar to TW1 one. TBH and *Fir tree* values are slightly higher than TW1 case and *Blade colling slot* value is quite lower. Also for TW3 TBH is a critical region. Together with *Radius* AB, AT and especially *Borehole*, the results are above the  $1.5S_m$  curve in the Primary acceptance plot, but below  $2S_m$ . Regarding peak stresses the same regions shows high values, but also *Air slot* and *Fir tree* are quite high. In this case Neuber's reduction is able to lower these preliminary results below the  $S_y$  curve, apart from TBH, which value is higher than both TW1 and TW2 equivalent region.

Regarding the DP, *Internal cone* is very closed to the creep curve in the Primary + Secondary verification, but the allowable stress is slightly higher. In the Peak stress verification *Air cooling hole* and TBH AFT are the highest values, but after the Neuber's reduction they both fall down the  $S_y$  curve. Also in AS the TBH value is high and in this case the reduced value is still relatively higher than  $S_y$  stress at the given temperature. Other peak stresses like *Outer cone* and *Rabbit fit* are quite high but Neuber's reduction confirms they are not worrying.

The SP2-3 is the only component whose post processing assures the complete acceptability of all the investigated regions for each of the static structural verifications, so none of them will be discussed. The table in Figure 3.46 contains all the results information divided for each component.

OTHERS							Actual values		Extra Load		Neuber's reduction
Component		Evaluation	Type of stress	Codification	Allowable Stresses		Temp; °C/°C	Stress; MPa/MPa	Coeff trans	Stress; MPa/MPa	Mpa/MPa
<b>Primary Stress</b>											
TW3	Primary Stress	Bore Hole	Average	HvM	Pm (or PL) + Pb 1.5Sm 1.25 St		0,82	0,91	1,0	0,91	
	Primary Stress	Radius AB	Average	HvM	Pm (or PL) + Pb 1.5Sm 1.25 St		0,80	0,83	1,0	0,83	
	Primary Stress	Radius AT	Average	HvM	Pm (or PL) + Pb 1.5Sm 1.25 St		0,84	0,84	1,0	0,84	
	Primary Stress	TBH	Average	HvM	Pm (or PL) + Pb 1.5Sm 1.25 St		0,84	0,91	1,0	0,91	
TW2	Primary Stress	Bore Hole	Average	HvM	Pm (or PL) + Pb 1.5Sm 1.25 St		0,78	0,78	1,0	0,78	
<b>Primary + Secondary Stress</b>											
DP	Primary + Secondary Stress	Internal Cone	Average	HvM	Pm (or PL) + Pb + Q 2Sm 1.25 St		0,83	0,42	1,0	0,66	
<b>Peak Stress</b>											
DP	Peak Stress	Air Cooling Hole	Peak	HvM	Pm (or PL) + Pb + Q + F Sy		0,82	0,55	1,2	1,02	0,94
	Peak Stress	TBH AFT	Peak	HvM	Pm (or PL) + Pb + Q + F Sy		0,82	0,69	1,2	1,29	0,99
TW2	Peak Stress	Fir Tree	Peak	HvM	Pm (or PL) + Pb + Q + F Sy		0,96	1,93	1,0	1,93	1,12
	Peak Stress	TBH	Peak	HvM	Pm (or PL) + Pb + Q + F Sy		0,90	1,51	1,2	1,81	1,10
	Peak Stress	Bore Hole	Peak	HvM	Pm (or PL) + Pb + Q + F Sy		0,84	0,94	1,2	1,13	1,00
	Peak Stress	Blade Cooling Slot	Peak	HvM	Pm (or PL) + Pb + Q + F Sy		0,96	1,38	1,2	1,66	1,10
TW3	Peak Stress	Radius AB	Peak	HvM	Pm (or PL) + Pb + Q + F Sy		0,80	0,85	1,2	1,02	0,96
	Peak Stress	Air Slot	Peak	HvM	Pm (or PL) + Pb + Q + F Sy		0,84	0,86	1,2	1,03	0,97
	Peak Stress	Fir Tree	Peak	HvM	Pm (or PL) + Pb + Q + F Sy		0,94	1,03	1,0	1,03	0,97
	Peak Stress	TBH	Peak	HvM	Pm (or PL) + Pb + Q + F Sy		0,78	1,54	1,2	1,85	1,10
	Peak Stress	Bore Hole	Peak	HvM	Pm (or PL) + Pb + Q + F Sy		0,82	0,91	1,2	1,10	0,99
AS	Peak Stress	Outer Cone	Peak	HvM	Pm (or PL) + Pb + Q + F Sy		0,70	0,70	1,2	1,26	0,99
	Peak Stress	TBH	Peak	HvM	Pm (or PL) + Pb + Q + F Sy		0,73	1,22	1,2	2,23	1,06
	Peak Stress	Rabbit Fit	Peak	HvM	Pm (or PL) + Pb + Q + F Sy		0,72	0,59	1,2	1,07	0,96

Figure 3.46: Summary table results (all the rest)

### Comments

Turbine components simulation results have been post processed according to design criteria. Multiple critical areas have been spotted out and for each of them further analysis are needed in order to specify our conclusions. Transient 2D rotor analysis and Low Cycle Fatigue prediction are provided in the next chapter to correct preliminary result and to estimate life-time endurance of components.

# Chapter 4

## Transient FEM Analysis

### 4.1 Introduction

The objective of this chapter is the 2D FEA of the FR1500 rotor assembly in start-up and shut-down conditions. Understanding the behaviour of the machine during these transients is even more important with respect to the steady-state analysis to assess critical areas and evaluate the cumulated damage according to life-prediction techniques [9]. In chapter 3 it was anticipated the intensification phenomena of stresses during transients. This is mainly due to the establishment of high thermal gradients, which can greatly affect the loading condition of a component, introducing the secondary stress contribution, as it was just discussed. Once the base load is reached after starting the machine, the component's metal is not yet at the steady-state temperature, because heat diffusion takes time; this is why rotor's disks experience high gradients. The direction of them is not only radial, but also axial and it can determine bending moments, that bring to an unexpected result in some regions.

The goal of transient analysis is to derive the temperature map of the rotor at each time laps and the stress status at the same points in time. In this way it is possible to detect different critical time-steps, where specific regions experience high peak stresses, which needs to be verified considering the temperature field in that moment.

This is done to classify FR1500 rotor components in terms of cyclic fatigue performances, with respect to the OEM-recommended stars and stops, namely Factored Fired Starts (FFS). To achieve our purpose in this chapter the following points will be presented:

- A full description of variables-over-time boundary conditions will be given.
- Results will be commented and specific ones will be compared to preliminary results in the steady-state solution, where was considered the intensification factor.
- LCF analysis in critical areas will be provided. In order to account for mean stress contribution, Smith-Watson-Topper model was used to estimate the cumulated damage in terms of cycles, as we have just described in section 1.3.3.

The aim of LCF is to verify components according to the first fracture mode, so it is needed to investigate the Maximum Principal stress rather than the Equivalent one, used in the steady-state analysis. To this end, it is crucial to specify that all the presented results are obtained looking to the maximum stress of the principal stress tensor.

## 4.2 Boundary conditions

Apart from boundary conditions and time steps of the analysis settings, the setup of the 2D transient simulation is identical to the one described in the steady state case. Also constraints applied to the structure are the same and constant during the simulation.

The idea behind boundary condition assignment is to start from measurable transient

operating parameters of the machine, that are involved in the mechanical and thermal load of components during start-up and shut-down [10]. These informations are real operative condition data, provided from engineering service in a simple cycle mode. The latter was chosen, because the starting ramps have the highest slopes and in them no stationary section is present, typical of combined cycle mode. It means that there is no time to calm down temperatures, so it represent the most severe condition, in which high thermal gradients amplify stresses.

In order to deal with the huge amount of parameter controls coming from a variety of sensors installed on the machine, we have selected only those that are related to our purpose. In order to simplify our simulation, data have been sampled against time using a qualitative approach to preserve useful information only. In other words, the sampling frequency depends on the rate of variation of parameters in time. Extrapolated data, involved in calculations, are:

- Turbine shaft angular Speed (TS)
- Compressor Discharge Temperature (CTD)
- Compressor Discharge Pressure (CPD)
- Turbine Bearing Temperature (TBT)
- Turbine Exhaust Temperature (TET)

Their trends, in percentage w.r.t. the steady-state values, are plotted in Figure 4.1, where they can be appreciated the different phases of the operating cycle.

- Starting ramp from 0 to 3600 RPM lasts 17 minutes.

- The Base Load, defined as the condition in which all the parameters have reached the 100%, is gained in more or less 30 minutes and this condition is maintained for about 300 minutes.
- Consequently Shut-down ramp starts after 330 minutes (5,5 hours) and lasts 47 minutes to bring RPMs proximately to zero.

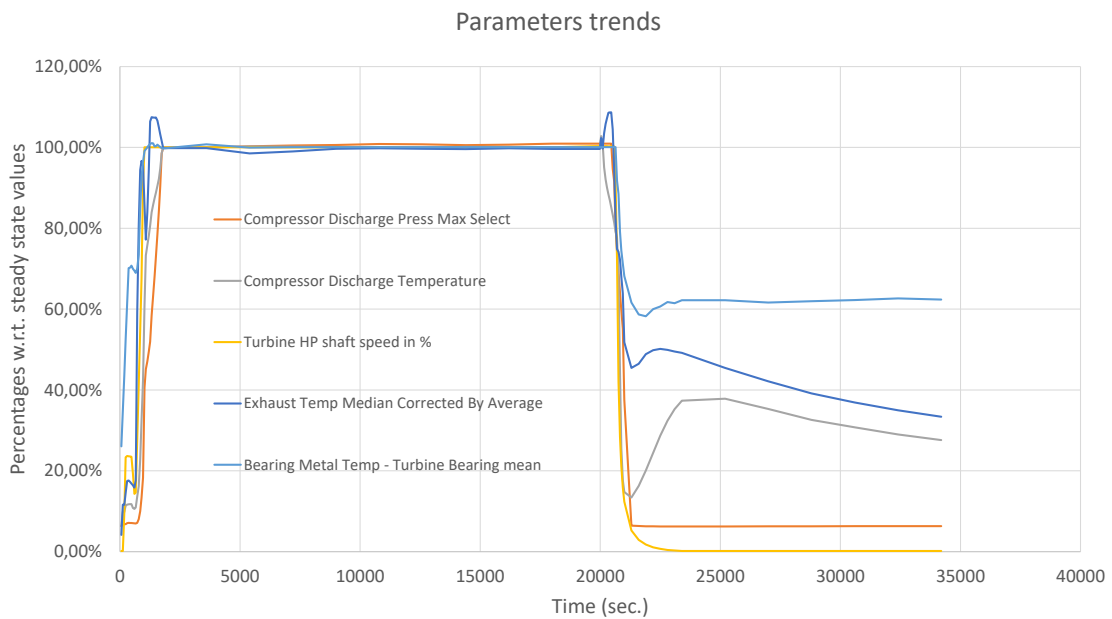


Figure 4.1: Parameters trends against time

As it was done in the previous chapter, also in this case Mechanical and Thermal conditions are discussed separately. In each section it will be justified the choice of parameters involved in calculations.

### 4.2.1 Mechanical

The speed trend in Figure 4.1 was given in input to consider variable angular velocity during ramps in transient analysis. Consequently the blades centrifugal load

changes proportionally to the given rotational speed, because assigned points of mass experience a variable centrifugal acceleration.

Regarding the turbine tie bolts, as anticipated in section 3.2.3, the estimated pre-load in different operating condition comes in handy in order to assign this coupling force in transients simulation [11]. Indeed, based on plot in Figure 3.12 (b), the variable load is applied following the obtained trends in Figure 4.2 for each stage. The forces are expressed in percentage w.r.t. the assembled condition (CASE 1 in section 3.2.3) and plotted against simulation time, so the 100% value is obtained only before the start.

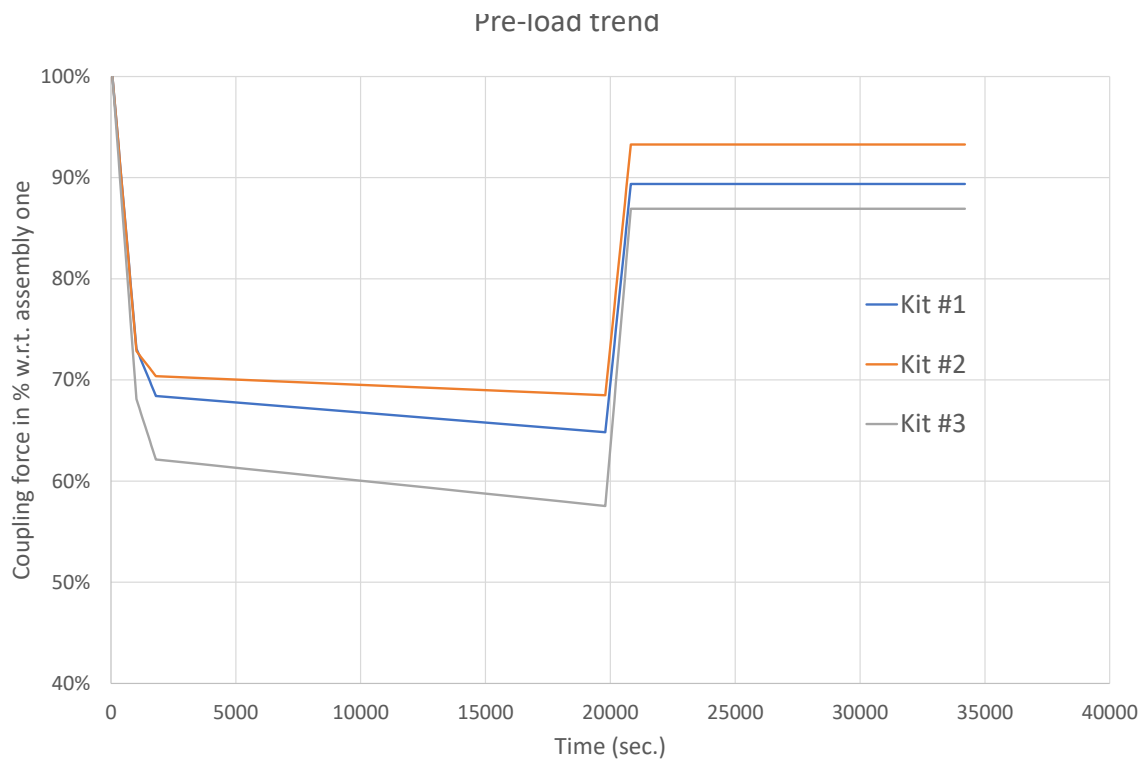


Figure 4.2: Pre-load trends for each turbine stage bolts kit

Bolts pre-load in the marriage flange and tie rods one in the compressor side is assumed to be constant during the transient simulation as in the steady-state one, because no specific analysis have been performed for them.

### 4.2.2 Thermal

Compressor discharge pressure and temperature trends are used to calculate variable Robin conditions on compressor rims (see Figure 3.17) and on turbine disks surfaces (see Figure 3.14), cooled down by secondary mass flow rate. It is intuitively to assume that air flowing through compressor blades follow the discharge trend and, consequently, the cooling air, drawn from the compressor, shares the same behaviour. The procedure used to calculate these conditions is the following:

1. In each specific boarder, pressure and temperature trends of air are evaluated according to the same percentage variation of the respective values of compressor discharge parameters, taking as reference the steady state quantities used in the steady-state simulation.
2. Once pressure and temperature values are known for each region at each time-step, air properties can be evaluated at the same points in time, using reliable engineering data sources. These are the density  $\rho_t$ , kinematic viscosity  $\mu_t$  and thermal conductivity  $k_t$ . where the pedex  $t$  denotes the considered time instant.
3. At this point the formulation in Equation 3.2.3 can be used to estimate the convective coefficient at each time laps  $h_t$ . This is done taking as reference the HTC evaluated in the steady state case, because we are dealing with the exactly same machine, so similarity hypothesis is met.

Giving the fact that we are talking about the same machine Eq. 3.2.3 can be re-write in a different manner.  $D_{eq}/D_{eq_{ref}} = 0$  because they are the same quantity and, by the definition given in section 1.3.2, Reynolds number can be expressed as  $Re = \frac{\rho V L_c}{\mu}$ . That said,  $\frac{Re_t}{Re_{ref}} = \frac{\rho_t n_t}{\mu_t} \frac{\mu_{ref}}{\rho_{ref} n_{ref}}$ , because the characteristic length is the same and

the velocity term is proportional to the angular shaft speed  $n_t$ , so we can replace it. Finally the relation becomes the following:

$$h_t = h_{ref} \frac{k_t}{k_{ref}} \left( \frac{\rho_t n_t}{\mu_t} \frac{\mu_{ref}}{\rho_{ref} n_{ref}} \right)^{0.8} \quad (4.2.1)$$

An example of variable Robin boundary condition is provided in Figure 4.3, where it is evident how film temperature trend follows the same CTD path and convective term  $h$  trend is influenced by CTD, CPD and TS together, so the path shape depends on their mutual contribute.

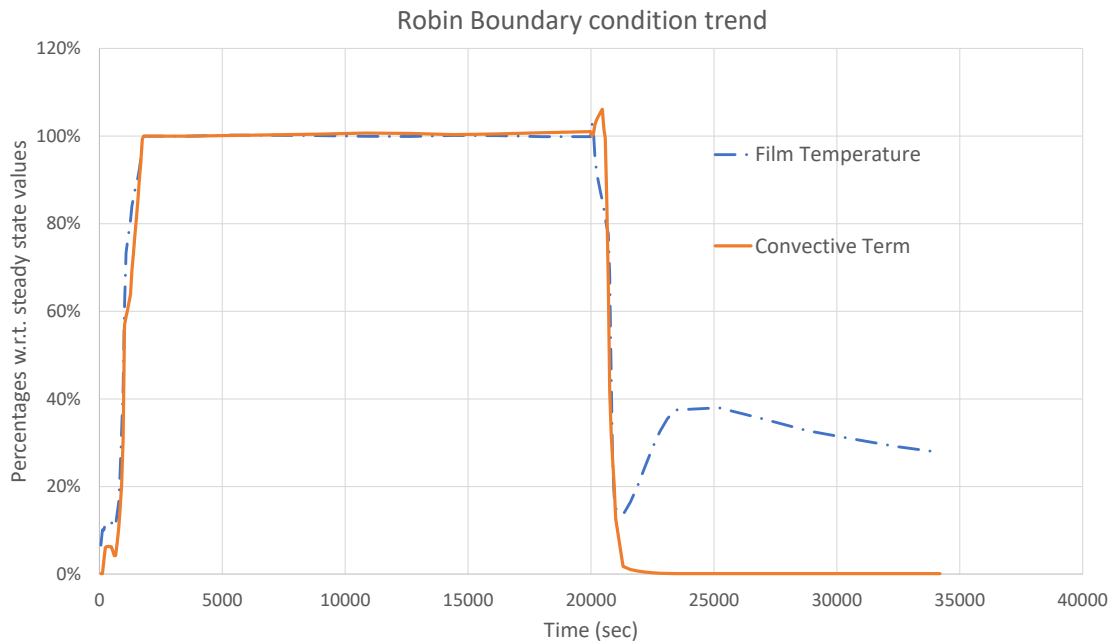


Figure 4.3: Example of variable Robin boundary conditions, plotted against simulation time

On turbine wheel rims (see Figure 3.16) and air cooling channels in C17 and DP components (see Figure 3.15) a variable-over-time Dirichlet boundary condition have been assigned. In order to do it, in case of turbine rims, a dedicated 2D transient thermal analysis was performed, including blade shank portion. Turbine exhaust temperature trend have been used as reference to assign proper boundary conditions

on the tip surface of the shank. The resulting percentage variation of temperature on the rims allowed to create these conditions, taking as reference the steady-state values. The Temperature curves are plotted in Figure 4.4.

In case of air cooling channels the dedicated transient analysis was performed on C17 3D model, because here it was possible to assign variable Robin boundary condition in an internal region of the structural domain, following the procedure from points 1. to 3. Then boundary conditions have been applied as before.

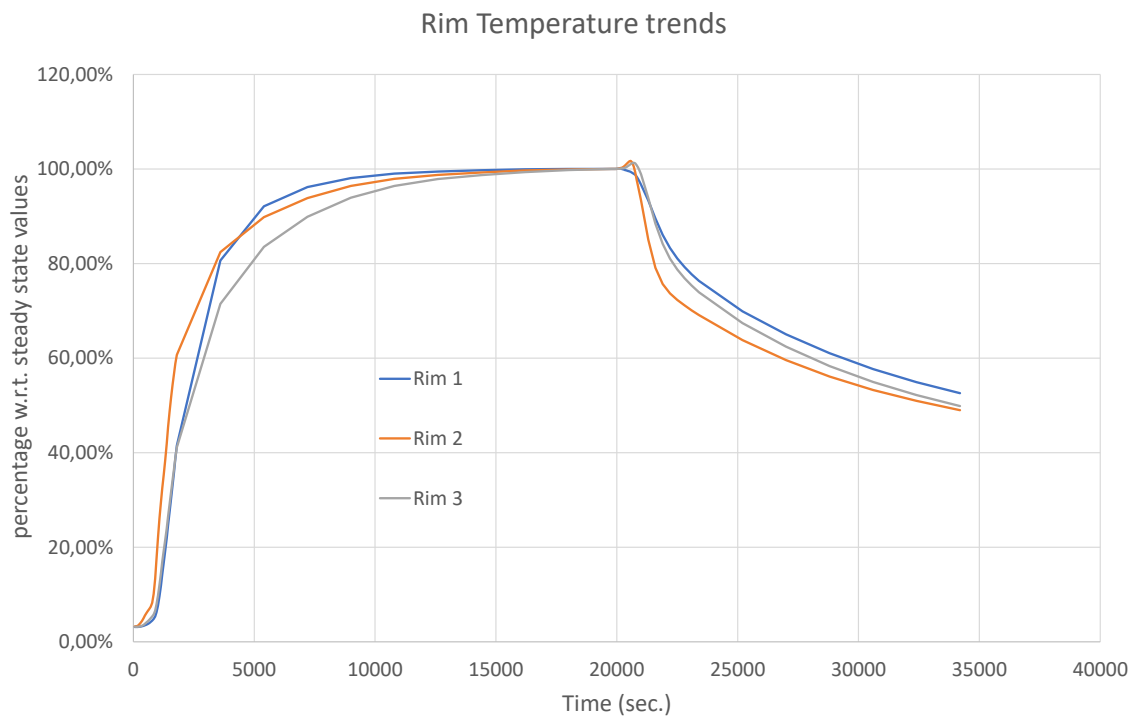


Figure 4.4: Example of variable Dirichlet boundary conditions, plotted against simulation time

Lastly on the bearing location, TBT trend have been used to assign temperature trend on the *Stub Shaft* surface.

### 4.3 Temperature map

The aim of this chapter is to provide the resulting temperature distribution fashion of the whole rotor at different points in time to highlight the transient behaviour. Temperature values have been normalized w.r.t. the maximum temperature reached in the steady-state condition.

In Figure 4.5 (a), the rotor is at the regime RPM but it has not already reached the based load. From that it is possible to see how secondary air flow, coming from last compressor stages, is heating up components. Travelling from last stage compressor rims through the air cooling channel, the temperature of surfaces, crossed by the flow, is increasing. Also temperature of turbine rims is increasing, because of heat coming from the main flow is diffusing through the shank. Once Base load is reached (Figure 4.5 (b)) at 30 minutes is evident how overall temperature is increased and heat has diffused more deeply inside the components, affecting the distribution. Where the heat transfer coefficient is higher temperature gradients changes more rapidly and where it is lower the time to calm down temperatures expends. This is the case of last turbine stage, where still at 90 minutes gradient is quite high from the borehole to the tip of the disk (see Figure 4.5 (c)). At the same time the temperature in proximity of the SP1-2 labyrinth seals and the first two turbine rims are now approaching the equilibrium condition of the steady-state case.

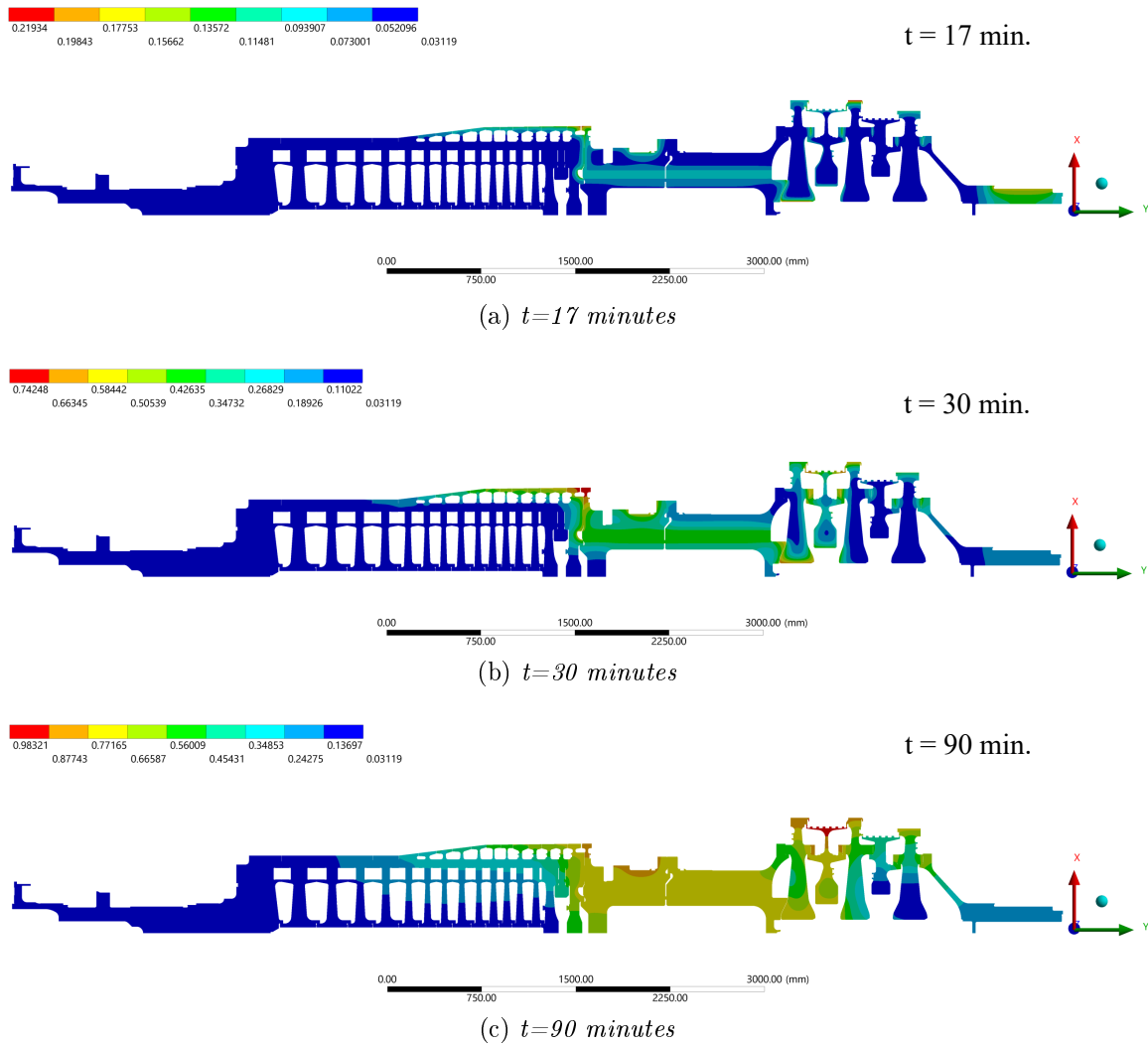


Figure 4.5: Temperature distribution of the whole rotor at different time laps

## 4.4 LCF analysis

### 4.4.1 Notch sensitivity

The Low cycle fatigue analysis is performed referring to the Smith-Watson-Topper model. As it was extensively discussed in section 1.3.3, this model allows to benefit from an elastic-plastic approach, accounting for the mean stress contribution.

The typical output of a stress analysis performed with a FEM model is inclusive not only of the primary + secondary stress, but also of the peak stress. This happens in particular geometrical features of the structure, where there is a remarkable change in direction, like grooves, sharp edges and fillet radii. Restricted in these areas, the high stress are characterized by a concentration factor  $K_t$ , that we have just introduced in section 3.3.4. When we talk about LCF, the notch effect is less effective, so the peak stress should be not obtained multiplying by  $K_t$ , but multiplying by  $K_f < K_t$ ; a coefficient that can be extrapolated by testing notched specimens.

At that light, stresses coming from simulation output are analysed to see if concentration factor is present or not. In case the answer is yes, a proper notch sensitivity factor is applied to correct it, namely  $K_f/K_t$ .

Once stresses have been elaborated, LCF analysis is performed to compute Number of cycles  $N_c$  (endurance limit), according to the fatigue curve, considered at the the given temperature (see Figure 4.6). The goal is to verify that all peak stresses in critical regions of components, are able to accomplish 5000 OEM-recommended Factored Fired Starts (FFS).

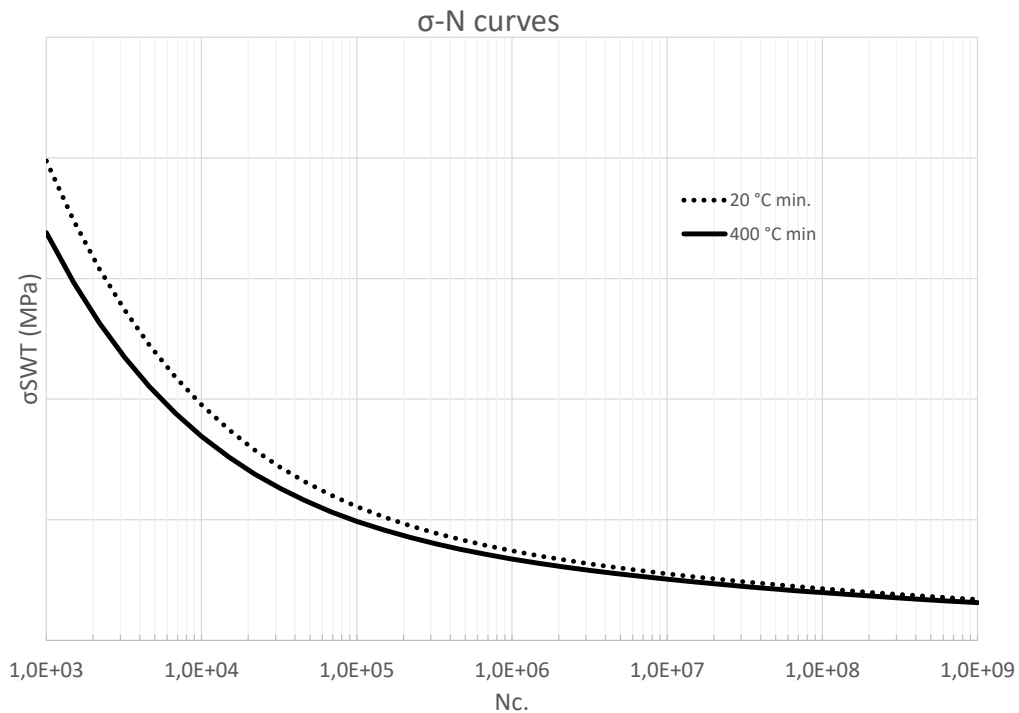


Figure 4.6: Smith-Watson-Topper Fatigue curve at R.T. and 400°C as example

#### 4.4.2 Compressor side

The Compressor side has not already been discussed in the steady-state section and reasons have been justified at the beginning of section 3.3.3.

Critical areas, spotted out during the 2D transient analysis are common geometrical features of all compressor wheels. These are the *Rabbit fit radius* and the *Borehole*. The former are the ones in proximity of central planes, where we have the mechanical contact among components. To better understand where are located these regions, a legend in Figure 4.7 is provided. In (a), an example of the C9 geometry is representative for all CW from C1 to C13 and in (b) is represented the assembled portion from C14 to C17 to point all the different locations.

For compressor wheels two different type of material have been adopted. From C12 to C17 the used material is the same of *Distance Piece* and *AFT Stub Shaft*, because it

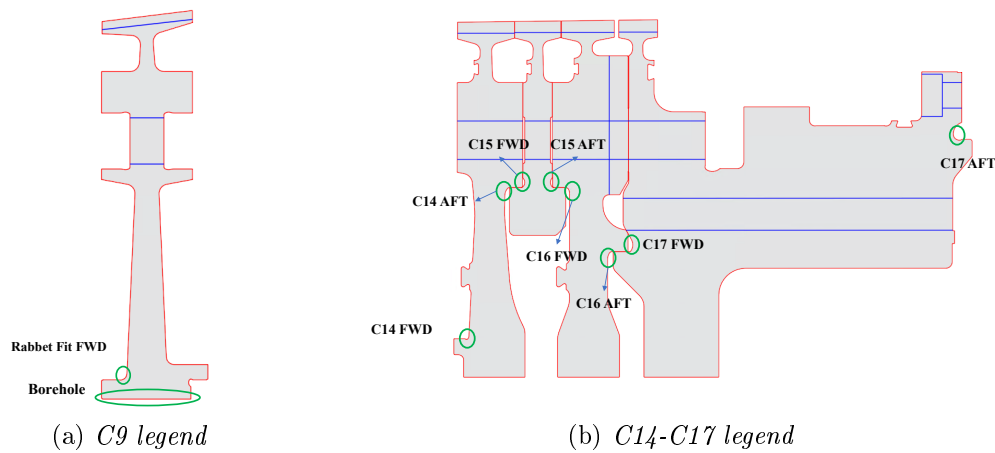
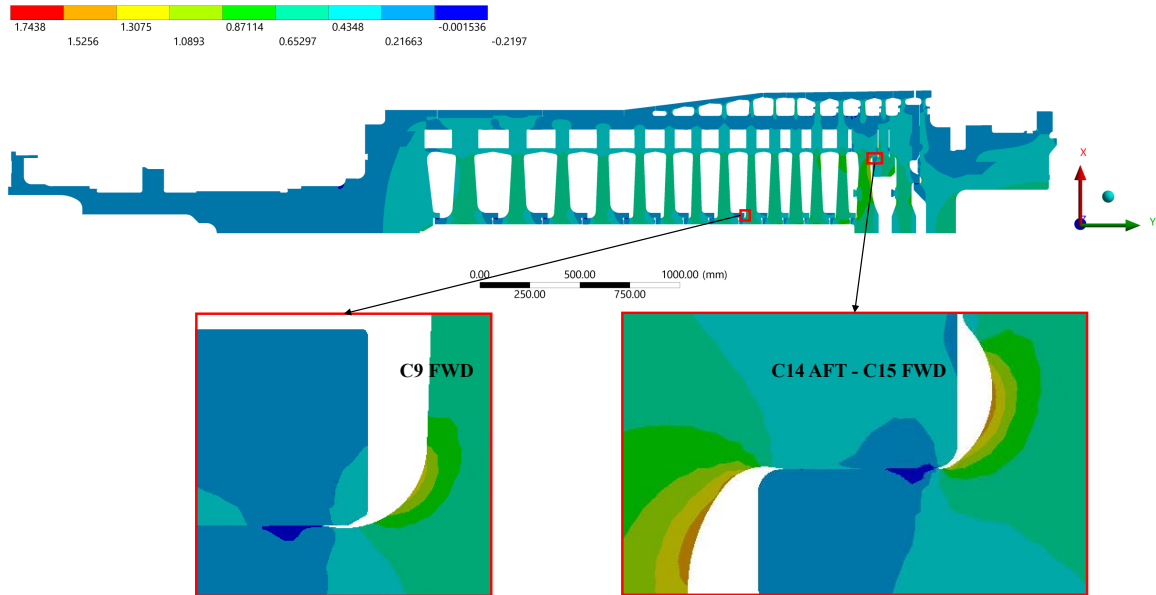


Figure 4.7: Temperature distribution of the whole rotor at different time laps

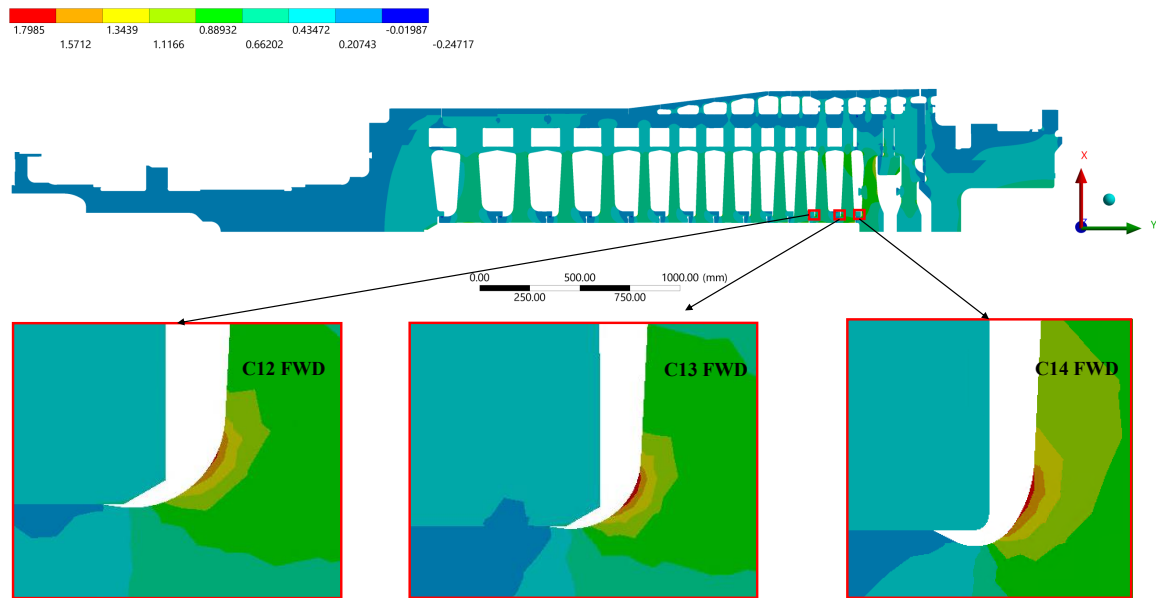
is more resistant at higher temperatures. For the rest, the material is a different alloy steel, generally adopted for cold components. Consequently the following approaches have been used to normalize provided results in terms of Maximum principle stresses:

- To properly compare results of disks of different materials the common denominator is the yielding stress of the C12 - C17 CWs at the given temperature. Consequently color bars of ANSYS output distributions and y-axis values of transient charts are normalized following this approach.
- Results summarized in tables are normalized using the yielding stress of the proper material at the given temperature. In this way each component can be analysed and verified according to its own base material properties.

FR1500 compressor disks typically present peak stress values at 3600, 5400 and 7200 seconds. In Figure 4.8 (a) and (b) stress distribution on most critical rabbet fit radii is highlighted in zoomed images. From this pictures is evident how peak stresses generally overcome  $S_y$ . As observed in Figure 4.8, peak stresses from C12 to C15 FWD are the highest ones.



(a)  $t = 5400 \text{ sec.}$



(b)  $t = 7200 \text{ sec.}$

Figure 4.8: Maximum Principle stress distribution on most critical *Rabbet fit* radii

Typical outcome of 2D transient analysis is temperature and stress trend as a function of time. To give an idea on Rabbet fit regions C9, C13, C14 FWD and C15 FWD trends are taken as example in Figure 4.9 and 4.10. In the former is quite evident how increasing the compressor stage, the overall mean temperature rises. Moreover C15 FWD region is located closer to the air mass flow, so the trend is more affected by the Compressor Discharge Temperature one.

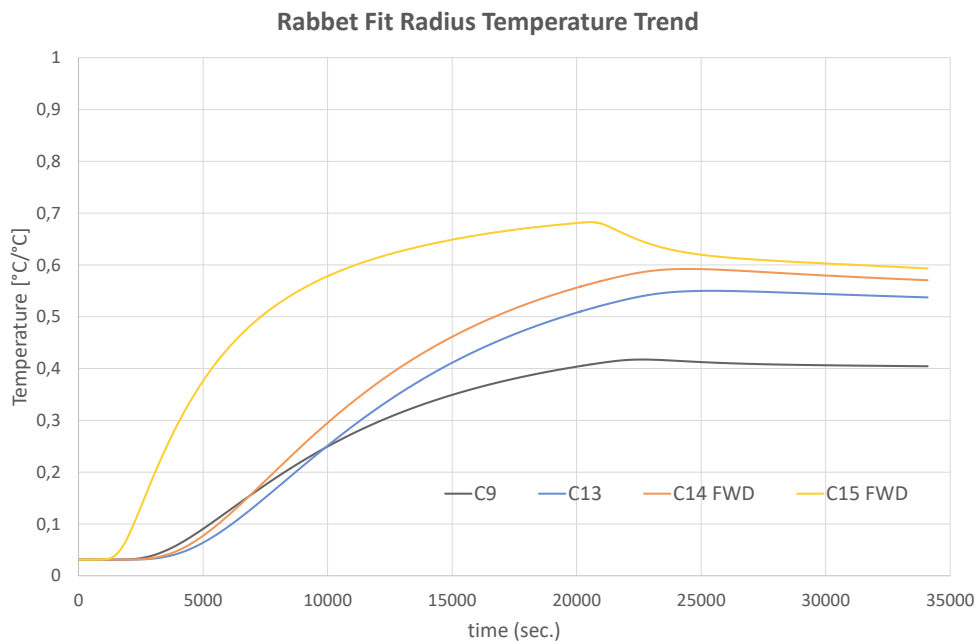


Figure 4.9: *Rabbet fit* radius temperature trend on C9, C13, C14 FWD and C15 FWD

In figure 4.10 it can be appreciated how stresses are influenced by transient ramps. Peak stress are mainly caused by the establishment of high thermal gradients at the critical time steps, as it can be seen in Figure 4.5 (c), especially in the last stages. It is important to note that compressor wheels are not cooled down by any kind of refrigerating flow. It means that adiabatic condition is assumed to almost all the side surfaces and heat transfer is by pure conduction.

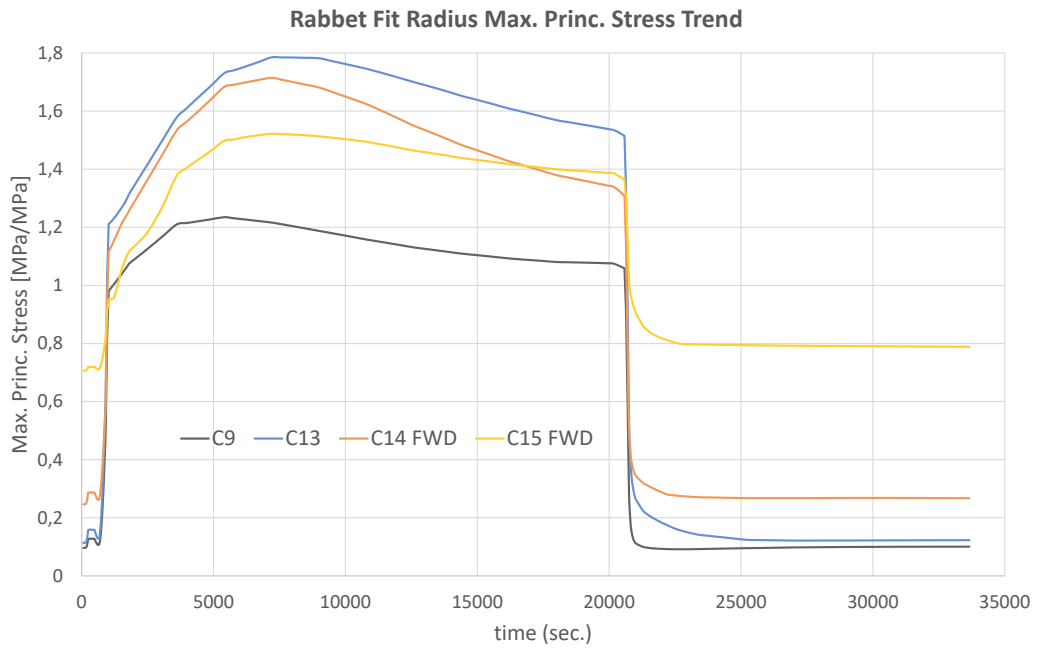


Figure 4.10: *Rabbit fit* radius stress trend on C9, C13, C14 FWD and C15 FWD

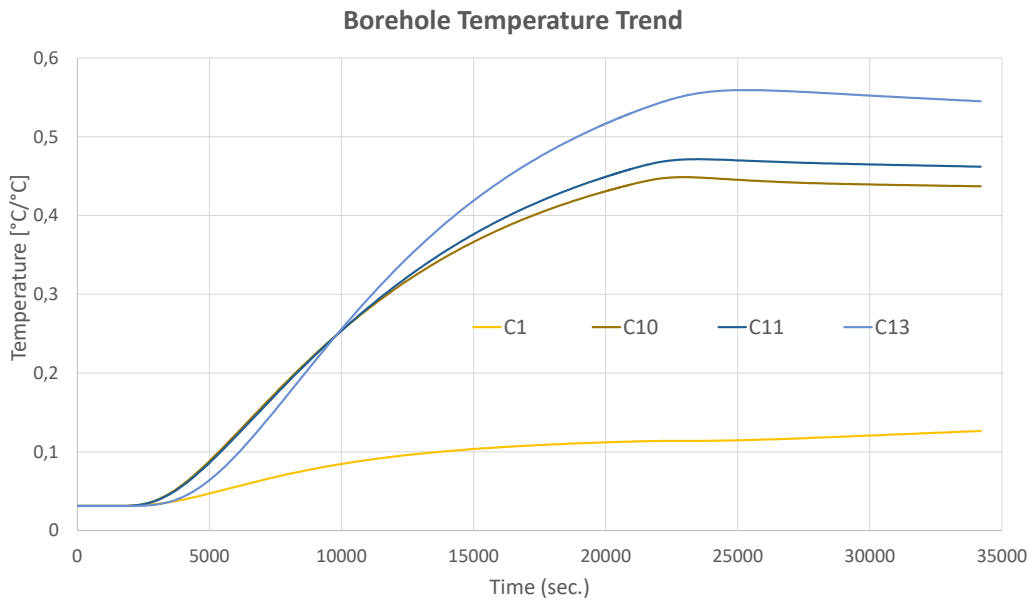


Figure 4.11: *Borehole* temperature trend on C1, C10, C11 FWD and C13

Almost same considerations can be done in case of *Borehole* regions, Which temperature and stress trends are respectively represented in Figure 4.11 and 4.12. In this case C1, C10, C11 and C13 are taken as example.

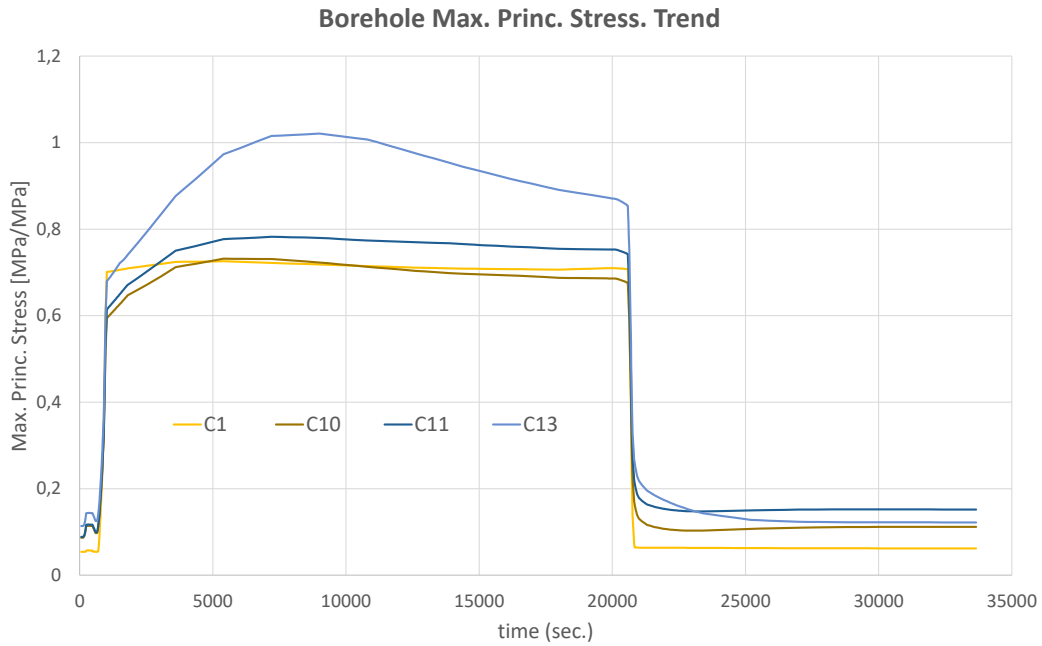


Figure 4.12: *Borehole* stress trend on C1, C10, C11 FWD and C13

Results are collected in tables below from C1 to C17. For each of them the peak stress value is reported as given from ANSYS output  $\sigma_{un-notched}$  and corrected by the notch sensitivity factor  $\sigma_{notched}$ . For both them Number of cycles to failure  $N_c$  are computed and the percentage of useful life covered is evaluated for the notched case by  $\frac{N_c}{5000} \times 100$  and indicated in the last column as  $\Sigma_{N_c./n}$ . In case of *Borehole* table, C14 and C16 are not considered because they are full disks.

Rabbit Fit	t peak [s]	T Hot Day	$\sigma_{M.P. \text{ Un-notched}}$	Nc. Un-notched	Kf / Kt	$\sigma_{M.P. \text{ Notched}}$	Nc. Notched	$\Sigma_{N/n}$	
C1 - C11	1	3600	0,07	0,53	2,13E+04	0,6	0,32	>1.0E+05	0,22%
	2	3600	0,07	0,61	7,93E+03	0,6	0,36	>1.0E+05	0,96%
	3	3600	0,08	0,72	2,66E+03	0,6	0,43	9,86E+04	5,07%
	4	3600	0,08	0,72	2,82E+03	0,6	0,43	>1.0E+05	4,65%
	5	3600	0,09	0,90	7,97E+02	0,6	0,54	1,70E+04	29,36%
	6	3600	0,09	0,91	7,55E+02	0,6	0,55	1,58E+04	31,68%
	7	5400	0,14	1,02	4,36E+02	0,6	0,61	7,43E+03	67,33%
	8	5400	0,14	1,00	4,91E+02	0,6	0,60	8,69E+03	57,56%
	9	5400	0,14	1,03	4,23E+02	0,6	0,62	7,11E+03	70,34%
	10	5400	0,13	1,01	4,59E+02	0,6	0,61	7,92E+03	63,11%
	11	5400	0,13	0,97	5,56E+02	0,6	0,58	1,03E+04	48,73%
C12 - C17	12	7200	0,18	1,64	1,11E+03	0,6	0,98	8,61E+04	5,81%
	13	7200	0,17	1,79	7,53E+02	0,6	1,08	2,27E+04	22,05%
	14 FWD	7200	0,20	1,72	8,86E+02	0,6	1,03	3,78E+04	13,24%
	14 AFT	5400	0,37	1,54	1,41E+03	0,6	0,93	>1.0E+05	2,30%
	15 FWD	5400	0,43	1,51	1,56E+03	0,6	0,90	>1.0E+05	1,46%
	15 AFT	1020	0,06	0,65	>1.0E+05	1,0	0,65	>1.0E+05	0,00%
	16 FWD	1020	0,07	0,98	>1.0E+05	0,7	0,69	>1.0E+05	0,00%
	16 AFT	3600	0,60	0,91	>1.0E+05	0,7	0,64	>1.0E+05	0,00%
	17 FWD	1800	0,39	1,12	1,18E+04	0,6	0,67	>1.0E+05	0,00%
	17 AFT	1020	0,08	0,55	>1.0E+05	1,0	0,55	>1.0E+05	0,00%

Figure 4.13: Rabbit fit Max. Princ. stress and LCF prediction

Borehole	t peak [s]	T Hot Day	$\sigma_{M.P. \text{ Un-notched}}$	Nc. Un-notched	Kf / Kt	$\sigma_{M.P. \text{ Notched}}$	Nc. Notched	$\Sigma_{N/n}$	
C1 - C11	1	5400	0,08	0,60	8,68E+03	1,0	0,60	8,68E+03	57,58%
	2	3600	0,07	0,55	1,45E+04	1,0	0,55	1,45E+04	34,55%
	3	3600	0,08	0,55	1,59E+04	1,0	0,55	1,59E+04	31,53%
	4	3600	0,08	0,54	1,80E+04	1,0	0,54	1,80E+04	27,75%
	5	3600	0,08	0,52	2,43E+04	1,0	0,52	2,43E+04	20,57%
	6	3600	0,08	0,48	4,43E+04	1,0	0,48	4,43E+04	11,29%
	7	5400	0,13	0,49	3,73E+04	1,0	0,49	3,73E+04	13,42%
	8	5400	0,13	0,53	2,01E+04	1,0	0,53	2,01E+04	24,83%
	9	5400	0,13	0,51	2,73E+04	1,0	0,51	2,73E+04	18,29%
	10	5400	0,13	0,61	7,68E+03	1,0	0,61	7,68E+03	65,14%
	11	5400	0,13	0,65	5,23E+03	1,0	0,65	5,23E+03	95,67%
C12 - C17	12	7200	0,18	0,74	>1.0E+05	1,0	0,74	>1.0E+05	0,00%
	13	7200	0,17	1,02	4,70E+04	1,0	1,02	4,70E+04	10,63%
	14								
	15	3600	0,28	0,83	>1.0E+05	1,0	0,83	>1.0E+05	0,11%
	16								
	17	1800	0,34	0,56	>1.0E+05	1,0	0,56	>1.0E+05	0,00%

Figure 4.14: Borehole Max. Princ. stress and LCF prediction

## COMMENTS

The highest stresses, especially in the rabbet fit case, are induced from the 12-th to the 15-th stage and it is quite intuitive to think that hotter compressor wheels are the most loaded components. Even if the stress evaluation shows this, quite surprising the most "damaged" components are the last stages of the first group. That's why they are made by a less performing material from a fatigue endurance point of view. In the first table in Figure 4.13 C7,C9 and C10 overcome the 60% of recommended life. Borehole analysis in Figure 4.14 reveals that also first stages are quite critical (C1 reaches almost 58 %) and C11 components seems not to have residual life left, because peak stress consumes the 96 %.

### 4.4.3 Turbine side

As it was done in the previous chapter, preliminary results, in terms of maximum principal stress, can be obtained multiplying the peak stresses by a transient coefficient of 1.2, coming from 3D steady state analysis. Some of them can be deeply investigated in the 2D transient analysis of the whole rotor. That's the case of *borehole*, *rabbet fit* and *armpits* regions, where results can be easily compared among the two models. Critical issues, highlighted in the static structural verification of section 3.4, are analysed in thi chapter to performe LCF prediction.

As it was done for the compressor, also in this case significant results have been normalized with respect to the yielding stress at the given temperature and collected in example charts and summary tables. Geometrical legend for TW1 and SP1-2 can be appreciated in Figure 3.27 and 3.33 and for the others components in **Annex**.

### 3D Results

LCF analysis performed on max. princ. peak stresses coming from 3D models reveals that some regions do not match OEM specifications. Indeed  $\Sigma_{N/n}$  parameter, in the case of *blade cooling slot* of the first stage and TBH of both TW3 and AS, exceeds the recommended 100%. As you can see in the summary table in Figure 4.15 TBH peak stress is quite high also in TW2 and the same for *borehole* region both in TW1 and TW2.

3D Max. Princ. Stress	T Hot Day	$\sigma_{peak}$	Coeff. trans.	$\sigma_{M.P. Un-notched}$	Nc. Un-notched	Kf / Kt	$\sigma_{M.P. Notched}$	Nc. Notched	$\Sigma_{N/n}$	
TW1	Borehole	0,82	0,86	1,2	1,03	6,37E+03	1,00	1,03	6,37E+03	78,49%
	Blade Cooling Slot	0,96	2,27	1,2	2,72	2,97E+02	0,64	1,74	1,15E+03	434,48%
	TBH	0,89	1,22	1,2	1,46	1,98E+03	0,64	0,94	8,79E+03	56,90%
TW2	Borehole	0,84	0,87	1,2	1,05	5,96E+03	1,00	1,05	5,96E+03	83,94%
	Blade Cooling Slot	0,96	1,42	1,2	1,70	1,24E+03	0,64	1,09	5,25E+03	95,16%
	TBH	0,90	1,36	1,2	1,64	1,38E+03	0,65	1,06	5,84E+03	85,60%
TW3	Borehole	0,82	0,81	1,2	0,97	7,71E+03	1,00	0,97	7,71E+03	64,89%
	TBH	0,78	1,64	1,2	1,97	7,79E+02	0,64	1,26	3,17E+03	157,59%
	Armpit FWD	0,83	0,72	1,2	0,87	1,18E+04	0,66	0,57	6,79E+04	7,37%
	Armpit AFT	0,82	0,72	1,2	0,86	1,23E+04	0,66	0,57	7,09E+04	7,06%
SP2-3	Borehole	0,86	0,65	1,2	0,78	1,79E+04	1,00	0,78	1,79E+04	28,00%
AS	TBH	0,73	1,91	1,2	2,30	2,44E+02	0,60	1,38	1,99E+03	250,30%

Figure 4.15: 3D sub-models Max. Princ. stress results and LCF prediction

DP and SP1-2 3D sub-models results have not been reported in the table, because preliminary evaluation on LCF analysis does not emphasize any critical region. For sake of brevity it was decided to do not provide details for resulting stresses, whose LCF prediction shows a low percentage and that cannot be compared with a corresponding 2D transient analysis outcome.

## 2D Results

2D transient analysis allow us to investigate stress trends. Unfortunately, because of 2D geometry limitations, we are not able to compare The critical results obtained in *blede cooling slot* and TBH regions.

*Borehole*, instead, is efficiently captured by this kind of analysis and, resulting trends, in Figure 4.16 suggest that for turbine wheels the 20% incipient may be to conservative in case of TW1 and TW2, so we can rely on a less worrying situation.

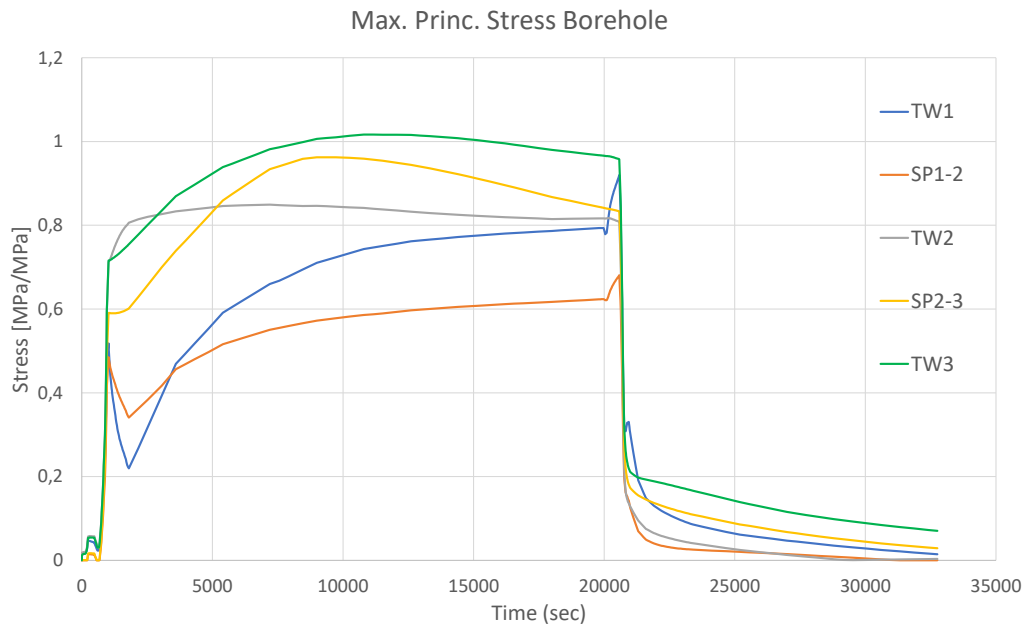


Figure 4.16: 2D transient *borehole* stress trends

TW3 trend, instead, reaches a peak value that is quite similar to the one obtained with the transient coefficient and SP2-3 seems to have a more stressed *borehole* region than the preliminary result of the 3D sub-model analysis. that's because in these cases the thermal gradient from internal to external radius of the disk cross sections is still quite high after hours later the base load condition (30 minutes). Higher the gradient, higher is the effect stress panorama in proximity of the *borehole*, as it was just said for the last compressor stages.

Temperature gradient are also partially responsible for high pressure contacts within components that led stress concentration on TW3 armpits to reach higher Peak values, compared to the ones evaluated with the 3D sub-model. Further details on trends can be seen in Figure 4.17.

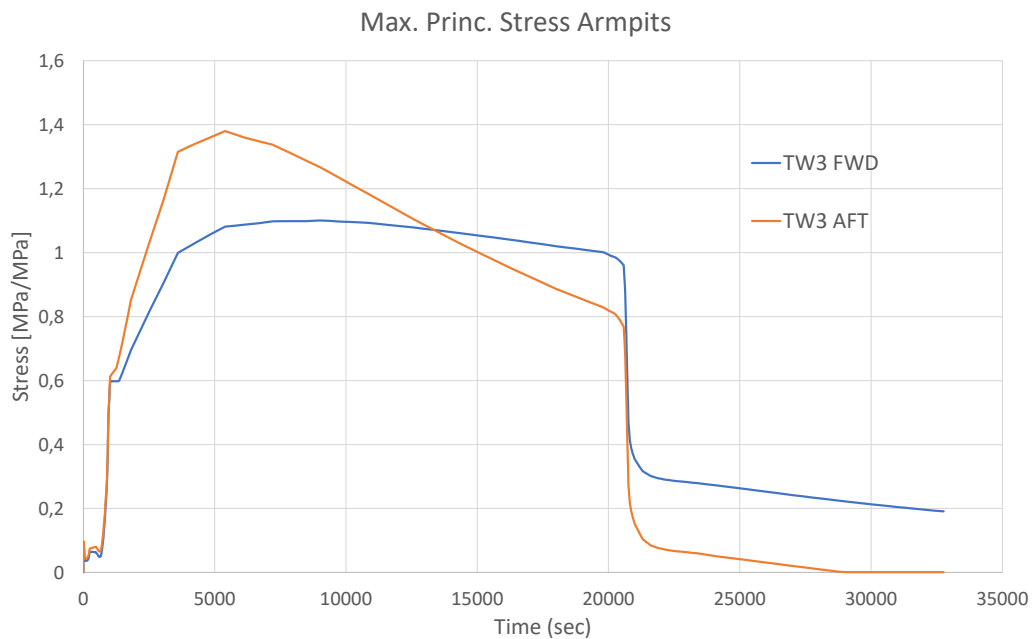


Figure 4.17: 2D transient *armpits* stress trends

The *labyrinth seals* of SP1-2 presents a peak value, quite similar to the one evaluated in the static-structural verification and reasons that led to this result are similar too. Looking to the trend curve in Figure 4.18, it is quite easy to notice that the maximum is reached at 3600 seconds, 30 minutes after the base load condition. The same is the critical time instant in which the FWD *rabbit fit radius* of SP1-2 reaches its peak value, as it can be observed in Figure 4.19.

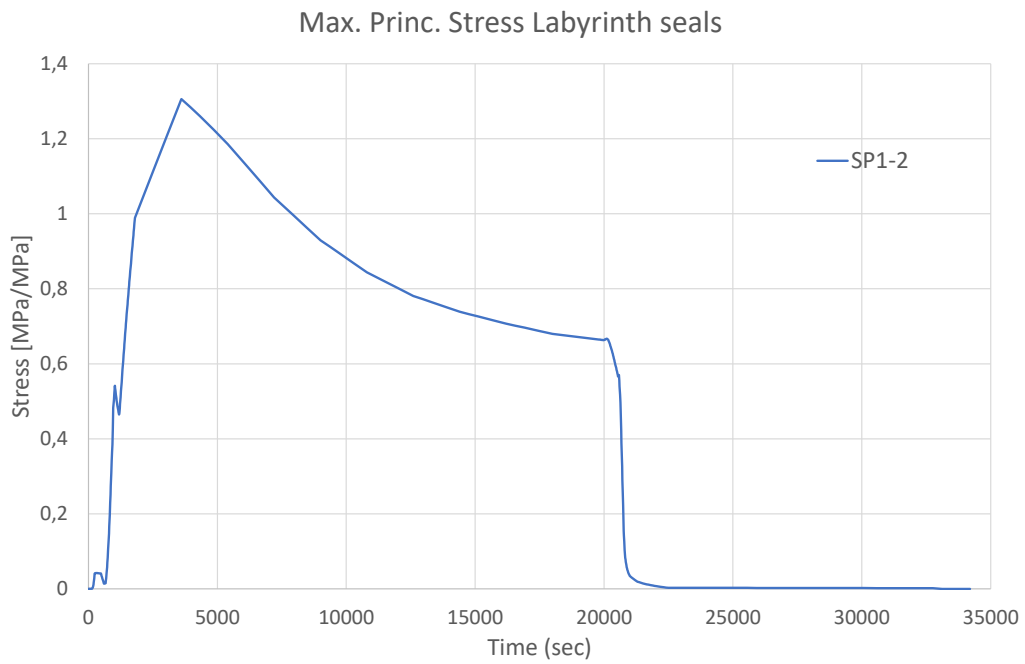


Figure 4.18: 2D transient *labyrinth seals* stress trend



Figure 4.19: 2D transient *rabbet fit* stress trends

2D transient results are collected in the following tables.

2D Transient	t peak [s]	T Hot Day	$\sigma_{M.P. \text{ Un-notched}}$	Nc. Un-notched	Kf / Kt	$\sigma_{M.P. \text{ Notched}}$	Nc. Notched	$\Sigma_{N/n}$	
TW1	Borehole	20580	0,73	0,92	9,62E+03	1,00	0,92	9,62E+03	51,98%
	Armpit FWD	2160	0,14	0,64	4,63E+04	1,00	0,64	4,63E+04	10,80%
	Radius AB	20580	0,88	1,04	6,29E+03	0,66	0,68	3,14E+04	15,93%
	Radius AT	5400	0,84	1,03	6,54E+03	0,66	0,67	3,29E+04	15,19%
TW2	Borehole	7200	0,64	0,85	1,34E+04	1,00	0,85	1,34E+04	37,32%
	Armpit AFT	3600	0,36	0,88	1,28E+04	0,66	0,58	7,17E+04	6,98%
	Radius FB	9000	0,78	0,92	9,79E+03	0,65	0,60	5,54E+04	9,02%
	Radius FT	4860	0,71	0,86	1,27E+04	0,66	0,57	7,10E+04	7,05%
TW3	Borehole	10800	0,27	1,02	7,65E+03	1,00	1,02	7,65E+03	65,34%
	Armpit FWD	9000	0,62	1,09	5,46E+03	0,66	0,71	2,63E+04	19,01%
	Armpit AFT	5400	0,56	1,37	2,57E+03	0,65	0,89	1,13E+04	44,35%
	Radius AB	10800	0,67	1,03	6,58E+03	0,65	0,67	3,36E+04	14,90%
Radius AT	10800	0,75	1,0	7,31E+03	0,65	0,65	3,88E+04	12,90%	

Figure 4.20: 2D transient stress results and LCF prediction on TWs

2D Transient	t peak [s]	T Hot Day	$\sigma_{M.P. \text{ Un-notched}}$	Nc. Un-notched	Kf / Kt	$\sigma_{M.P. \text{ Notched}}$	Nc. Notched	$\Sigma_{N/n}$	
SP1-2	Borehole	20580	0,786	0,68	3,09E+04	1,00	0,68	3,09E+04	16,16%
	Radius FT	1800	0,500	0,88	1,23E+04	0,66	0,58	6,91E+04	7,23%
	Radius AT	1800	0,470	0,88	1,22E+04	0,66	0,58	6,76E+04	7,40%
	Rabbit fit FWD	3600	0,738	0,88	1,14E+04	0,66	0,58	6,46E+04	7,74%
	Rabbit fit AFT	5400	0,782	0,89	1,09E+04	0,66	0,59	6,10E+04	8,20%
	Labyrinth	3600	0,900	1,30	2,92E+03	0,65	0,84	1,34E+04	37,18%
SP2-3	Borehole	9000	0,280	0,97	9,22E+03	1,00	0,97	9,22E+03	54,24%
	Armpit FWD	7920	0,560	0,68	3,27E+04	0,68	0,46	>1,0E+05	2,33%
	Armpit AFT	7200	0,455	0,58	7,09E+04	1,00	0,58	7,09E+04	7,05%

Figure 4.21: 2D transient stress results and LCF prediction on SP

## COMMENTS

LCF analysis on 2D transient simulation output reveals that all components can accomplish 5000 OEM-recommended FFS. The most critical regions are the TW3 and SP2-3 *borehole*, but they do not overcome the 70% of consumed life. The 3D sub-models analysis, instead, show multiple "red-flags" that must be further discussed in final conclusions of this paper.

# Chapter 5

## Grammel's method

### 5.1 Introduction

It may have been noticed while reading this paper, that rotating disks have particular cross section shape, because their thickness is not constant, but varies along the radial coordinate. This is typical of multiple technical applications such as Flywheels, Gears and Fans. This approach is widely used to control stress intensity and distribution inside the rotating components, which are usually undergoing centrifugal loads and thermal gradients, as in this case. The aim of this chapter is to explain a credited analytical approach to foresee induced stresses in axysimmetric bodies. This procedure is referred to as Grammel's method (1923) and it is still used today for its ability to provide well-approximated results. In simple cases this method provides a valid alternative to FEM analysis, which is nowadays the most reliable and user friendly tool implemented in several commercial software. In spite of its undisputed excellence, FEM requires lots of preliminary passages such as geometry preparation and meshing operations, that have already been discussed in detail. When using FEM does not give any additional benefit, Grammel's method can be a valid substitute to save time and achieve a good result accuracy. This procedure is based on the closed form solution of the differential equilibrium equation, ascribable to a constant

thickness disk's infinitesimal element, when plane stress condition can be assumed. Before turning to the formal discussion of Grammel's method implementation procedure, a brief theoretical introduction will be provided in this chapter to introduce the fundamentals of the method.

## 5.2 Constant thickness solution

Recalling section 1.3.1 of chapter 1 and looking at Figure 5.1, the equilibrium differential equation of constant thickness disk that is rotating at a constant angular speed  $\omega$  is the following:

$$\frac{d(\sigma_r r)}{dr} - \sigma_\theta + \rho \omega^2 r^2 = 0 \tag{5.2.1}$$

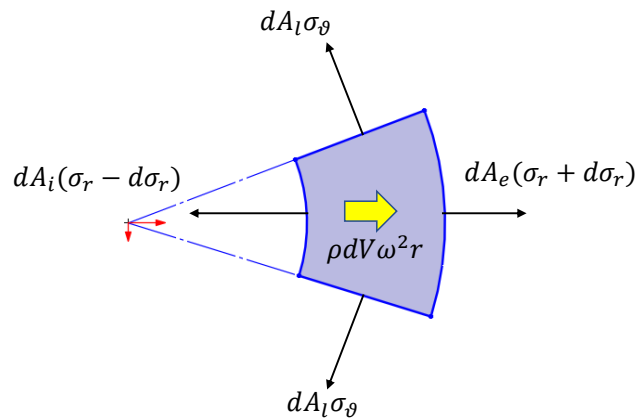


Figure 5.1: Infinitesimal element equilibrium vector forces

The equation is valid for both perforated disks and full disks. It was said that the body is subjected to a plane stress condition of axisymmetric type. It means that deformations are axisymmetric too, as it can be observed in Figure 5.2. On such account, we can evaluate the congruence equation for both radial and circumferential strain, respectively  $\varepsilon_r$  and  $\varepsilon_\theta$ .

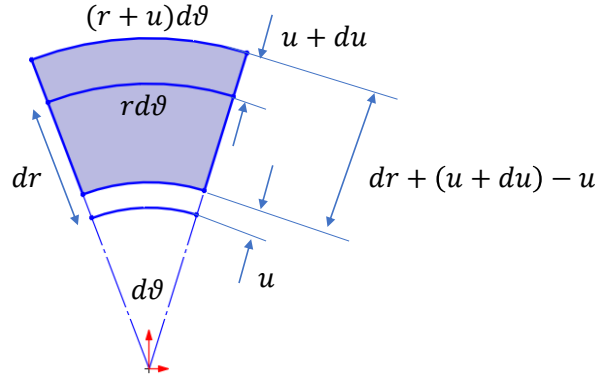


Figure 5.2: Infinitesimal element deformation shape

For radial strain:

$$\varepsilon_r = \frac{[dr + (u + du) - u] - dr}{dr} = \frac{du}{dr} \quad (5.2.2)$$

For circumferential strain:

$$\varepsilon_\theta = \frac{(r + u)d\theta - rd\theta}{rd\theta} = \frac{u}{r} \quad \rightarrow \quad u = \varepsilon_\theta r \quad (5.2.3)$$

At that light we can write a relation between 5.2.2 and 5.2.3 Eqs., that becomes the congruence equation:

$$\varepsilon_r = \varepsilon_\theta + r \frac{d\varepsilon_\theta}{dr} \quad (5.2.4)$$

The congruence equation can be expressed in terms of  $\sigma_r$  and  $\sigma_\theta$  stresses, exploiting the constitutive links in Eq. 1.3.6. So, assuming  $\alpha$  to be constant w.r.t. the disk's radial coordinate, the 5.2.4 becomes:

$$(1 + \nu)(\sigma_\theta - \sigma_r) + r \frac{d}{dr}(\sigma_\theta - \nu\sigma_r) + Er\alpha \frac{dT}{dr} = 0 \quad (5.2.5)$$

Taking the equilibrium equation 5.2.1, it is intuitive that the two following expressions can be directly obtained:

$$\sigma_r + r \frac{d(\sigma_r)}{dr} - \sigma_\theta + \rho\omega^2 r^2 = 0 \quad (5.2.6)$$

$$\frac{d\sigma_\theta}{dr} = r \frac{d^2\sigma_r}{dr^2} + 2 \frac{d\sigma_r}{dr} + 2\rho\omega^2 r \quad (5.2.7)$$

Substituting  $\sigma_\theta$  and  $\frac{d\sigma_\theta}{dr}$  in Eq. 5.2.5, the differential equation that describes the stress status of a rotating constant-thickness disk, subjected to a thermal gradient, becomes:

$$r^2 \frac{d^2\sigma_r}{dr^2} + 3r \frac{d\sigma_r}{dr} + (3 + \nu)\rho\omega^2 r^2 + E\alpha r \frac{dT}{dr} = 0 \quad (5.2.8)$$

The good news is that is possible to find a closed analytical solution for  $\sigma_r(r)$  and  $\sigma_\theta(r)$  for this particular case.

It consists in solving the homogeneous part  $\left[ r^2 \frac{d^2\sigma_r}{dr^2} + 3r \frac{d\sigma_r}{dr} \right]$ , ascribable to external and internal pressure boarders conditions and the particular integrals, for both inertial effect  $[(3 + \nu)\rho\omega^2 r^2]$  and thermal gradient effect  $\left[ E\alpha r \frac{dT}{dr} \right]$ . It is not interesting to replicate all the mathematical passages needed to find the final expressions, because they can be easily found in literature [6]. That said, in case of constant angular velocity and linear thermal gradient along the radius (see Figure 5.3), the following solutions for 5.2.8 are valid:

$$\sigma_r = A + \frac{B}{r^2} - \frac{(3 + \nu)}{8} \rho\omega^2 r^2 - \frac{E\alpha k}{3} r \quad (5.2.9)$$

$$\sigma_\theta = A - \frac{B}{r^2} - \frac{(1 + 3\nu)}{8} \rho\omega^2 r^2 - \frac{2E\alpha k}{3} r \quad (5.2.10)$$

Where  $k$  is the known slope of thermal gradient and A and B are the two constant values to be determined by the boarders conditions. The latter can be different depending on the case study. For example the value of blade centrifugal forces can be provided, and so the external pressure  $P_e$  acting at the external diameter. So the radial stress at the external radius  $R_e$  must be equal to that value  $\sigma_r(R_e) = P_e$ . In the same way Internal pressure can be known. Maybe no pressure is acting on the

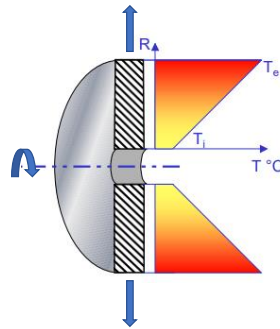


Figure 5.3: Sketch of a rotating constant-thickness disk, subjected to a linear thermal gradient

internal diameter and so radial stress at the internal radius  $R_i$  must be equal to zero

$$\sigma_r(R_i) = 0.$$

This is only to say that, once boarder conditions are known, A and B coefficients can be computed solving a linear system and  $\sigma_r$ ,  $\sigma_\theta$  can be evaluated at each radius.

### 5.3 The method and its implementation

When a disk has an arbitrary profile, the equation 5.2.1 is no more valid, because the thickness variable  $h$  cannot be neglected. When the thickness variability can be expressed with a simple analytical relation as a function of disk's radius  $h(r)$ , is still possible to find a closed solution for the differential equilibrium, but a unique solution that is valid in any case does not exist and one must determine it every time you face a different profile shape.

The Grammel's method can overcome this challenge with a geometric schematization. The variable-thickness disk can be replaced by series of N concentric ring elements, each of which has a constant thickness  $h$ . The radial extension of each ring depends on two parameters. They are the temperature difference and the thickness difference

between the internal and the external radius. the thickness variation should not be too high, otherwise the discretization is no more representative and the temperature variation should be as small as possible to allow considering constant material properties inside the ring. An example of this schematization is provided in Figure 5.4, where:

- $h_n$  is the n-th ring.
- $r_{ni}$  is the internal radius of the n-th ring
- $r_{ne}$  is the external radius of the n-th ring
- $R_e$  is the external radius of the disk
- $R_i$  is the internal radius of the disk (if the disk is not perforated  $R_i = 0$  but the method is still valid)

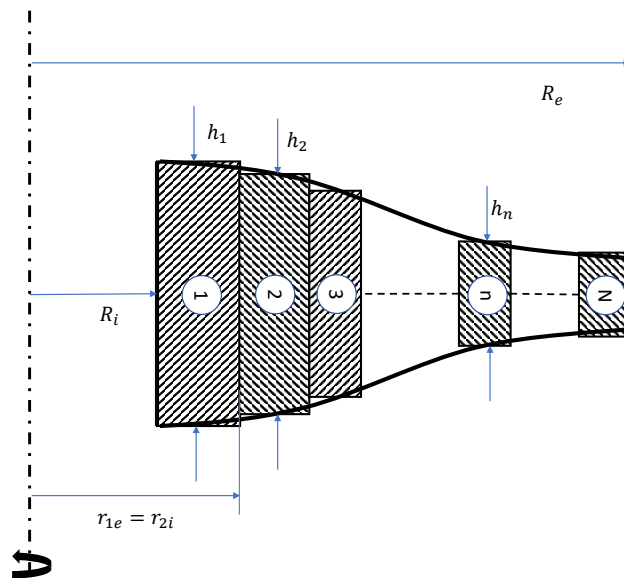


Figure 5.4: Disk cross section discretization in a series of N concentric rings

The point-line axis is the symmetric axis, that coincides with the rotational axis in case we have a rotating disk.

The power of this method is that for each ring Equations 5.2.9 and 5.2.10 are applicable because the element has a constant thickness and average material properties can be considered with good approximation. The higher the slope of thermal gradient and thickness variability, the higher is the number of rings by which we need to divide the disk. In short, the method is able to "sew" the rings one on the other, respecting the congruence of displacements and force equilibrium at the interface between one ring and the next. Indeed, solving the previous equations (5.2.9 and 5.2.10), means to find A and B parameter for each ring in the manner in which borders conditions of the problem are met and congruence and equilibrium conditions are respected among each element.

### 5.3.1 Procedure

For each ring element we have two unknowns parameters, so globally  $2N$  unknowns, namely  $A_1, A_2, \dots, A_N$  and  $B_1, B_2, \dots, B_N$  involved in  $\sigma_r$  and  $\sigma_\theta$  expressions. At least  $2N$  equations are needed in order to fully solve that problem. At the interface between one ring and the next two conditions are imposed:

- **Radial equilibrium condition:**

$$2\pi r_{(n-1)e} h_{n-1} \sigma_r(r_{(n-1)e}) = 2\pi r_{ni} h_n \sigma_r(r_{ni}) \quad (5.3.1)$$

Since the the radius at the interface is the same  $r_{(n-1)e} = r_{ni}$ , it is possible to write:

$$\sigma_r(r_{ni}) = \frac{h_{n-1}}{h_n} \sigma_r(r_{(n-1)e}) \quad (5.3.2)$$

- **displacement congruence:**

$$\varepsilon_{\theta}(r_{(n-1)e}) = \varepsilon_{\theta}(r_{ni}) \quad (5.3.3)$$

Following the constitutive link, Eq. 5.3.3 can be re-write in terms of radial and hoop stresses:

$$\begin{aligned} \frac{1}{E_{n-1}}[\sigma_{\theta}(r_{(n-1)e}) - \nu_{n-1}\sigma_r(r_{(n-1)e})] + \alpha_{n-1}(T(r_{(n-1)e}) - T_0) = \\ = \frac{1}{E_n}[\sigma_{\theta}(r_{ni}) - \nu_n\sigma_r(r_{ni})] + \alpha_n(T(r_{ni}) - T_0) \end{aligned} \quad (5.3.4)$$

For  $N$  rings there will be  $N - 1$  interfaces, so imposing these conditions at each of them means to write  $2(N - 1)$  equations, that are  $2N - 2$ . The last two equations are given by the boundary conditions that have been just discussed. Generally, in a turbine disk it is known the magnitude of centrifugal force  $F_c$  exercised by the row of blades, on the external surface of the disk. Consequently on the external radius  $R_e$  of the outermost ring the radial stress must be equal to:

$$\sigma_r(R_e) = \frac{F_c}{2\pi R_e h_N} \quad (5.3.5)$$

On the contrary, at the inner radius of the first ring, it is generally known the internal pressure value  $P_i$ , so the last equation should be:

$$\sigma_r(R_i) = P_i \quad (5.3.6)$$

Most of the time internal pressure is considered equal to zero. When the disk is not perforated, the last condition is no more valid because internal radius does not exist, so the last condition is replaced by the equality between radial and hoop stress at  $r = 0$ :

$$\sigma_r(r = 0) = \sigma_{\theta}(r = 0) \quad (5.3.7)$$

Equations 5.3.5 and 5.3.6 (or 5.3.7) are the last informations we need to solve the disk. The resulting linear system can be translated in matrix notation, as follows:

$$[C] \{X\} = \{b\} \quad (5.3.8)$$

Where  $[C] \in \mathbb{R}^{2NX2N}$  is the coefficient matrix and  $\{b\} \in \mathbb{R}^{2NX1}$  is the vector of constant terms. The unknowns are grouped in a column vector  $\{X\} \in \mathbb{R}^{2NX1}$  in pairs:

$$\{X\} = \begin{pmatrix} A_1 \\ B_1 \\ A_2 \\ B_2 \\ \cdot \\ \cdot \\ \cdot \\ A_N \\ B_N \end{pmatrix} \quad (5.3.9)$$

### 5.3.2 Inputs

What was just described in the previous section can be used to write a routine in a suitable programming language. The one used in this paper is a well known commercial software, called "MATLAB", which is an efficient tool to implement algorithms of this type.

The inputs of program's script are the material properties, temperature distribution and the geometry discretization.

- The former, depending on the disk base material, need to be provided at different temperatures in order to perform linear interpolations.
- Size of the problem will depend on geometry partitioning and this is done giving a vector of radial distances  $\{R\} \in \mathbb{R}^{(N+1)X1}$  and another one of ring's thicknesses

$\{H\} \in \mathbb{R}^{N \times 1}$ , as follows:

$$\{R\} = \begin{pmatrix} R_i \\ r_{1e} \\ r_{2e} \\ \cdot \\ r_{ne} \\ \cdot \\ r_{(N-1)e} \\ R_e \end{pmatrix} = \begin{pmatrix} R_i \\ r_{2i} \\ r_{3i} \\ \cdot \\ r_{ni} \\ \cdot \\ r_{Ni} \\ R_e \end{pmatrix} \quad \{H\} = \begin{pmatrix} h_1 \\ r_2 \\ \cdot \\ h_n \\ \cdot \\ h_N \end{pmatrix} \quad (5.3.10)$$

- At each radius of  $\{R\}$  a temperature value is associated, based on the thermal distribution, to define a vector of temperatures  $\{T\} \in \mathbb{R}^{(N+1) \times 1}$ . Given this, it is possible to compute the  $k$  slope of the distribution at each ring, as:

$$k_n = \frac{T(r_{ne}) - T(r_{ni})}{r_{ne} - r_{ni}} \quad (5.3.11)$$

### 5.3.3 Versatility

The Grammel's method was originally implemented as a table type algorithm, which procedure is slightly different than the one presented in this paper, in order to allow a by-hand computation of radial and hoop stresses. Anyway governing equations are the same and solution quality is practically equal.

Equations 5.3.5 and 5.3.6 depend on the nature of the problem. The ones presented in section 5.3.1 are suitable for a turbine disk in operating conditions, but in other cases boundary conditions change. For example another case-study in which the method is applicable is the stress evaluation of a press-fitted disk on a shaft. Starting from the interference value, an initial radial displacement can be estimated. Then, the 5.3.6 is replaced by the following condition:

$$\begin{aligned} u(R_i) = const. & \quad \longrightarrow \quad \varepsilon_\theta(R_i) \cdot R_i = const. \\ u(R_i) = \left\{ \frac{1}{E_1} [\sigma_\theta(R_i) - \nu_1 \sigma_r(R_i)] + \alpha_1 (T(R_i) - T_0) \right\} \cdot R_i & = const. \end{aligned} \quad (5.3.12)$$

Then, if the disk is not supporting rotating blades, the equation 5.3.5 is replaced by:

$$\sigma_r(R_e) = 0 \quad (5.3.13)$$

What said demonstrates the versatility of the Grammel's method, because it is adaptable to different problems, making only little changes in the algorithm equations, without modifying the entire structure.

## 5.4 Design concept of rotating disks and FEM validation

The aim of rotating disk design is to reduce stresses as much as possible and, sometimes, to approximate uniform stress distribution. The idea is to introduce a thickness variation along the radius to shape them in a more efficient way. To introduce the concept in this section, rotating conical disks, whose thickness varies linearly on radius, are taken as example [17]. Let us take a sample perforated disk made of Nickel-based steel alloy, with the following dimensions:

- Internal radius  $R_i = 106$  mm.
- External radius  $R_e = 854$  mm.
- Constant thickness  $h_{const.} = 171$  mm.

This is subjected to a linear thermal gradient from the *borehole* to the external diameter  $T = 200 \rightarrow 400$  °C and it is supporting a row of blades. Taking as example the U.S.A. grid frequency ( $60H_z$ ), the disk is supposed to rotate at a constant angular velocity of 3600 RPM + 3% over-frequency, so 3708 RPM. Reasonably, point mass of

buckets can exert as a whole 80000 KN of centrifugal force on the external diameter of the disk. It should be noted that it is described a typical case of thermo-mechanical load to which a turbine disk is subjected. The same load is applied to a conical disk with the same  $R_i$  and  $R_e$ . Its thickness convergence is linear, so the convergence angle is constant  $\frac{\varphi}{2} = 3.2^\circ$ . The two samples are made of the same material to be comparable and their geometries can be appreciated in figure 5.5.

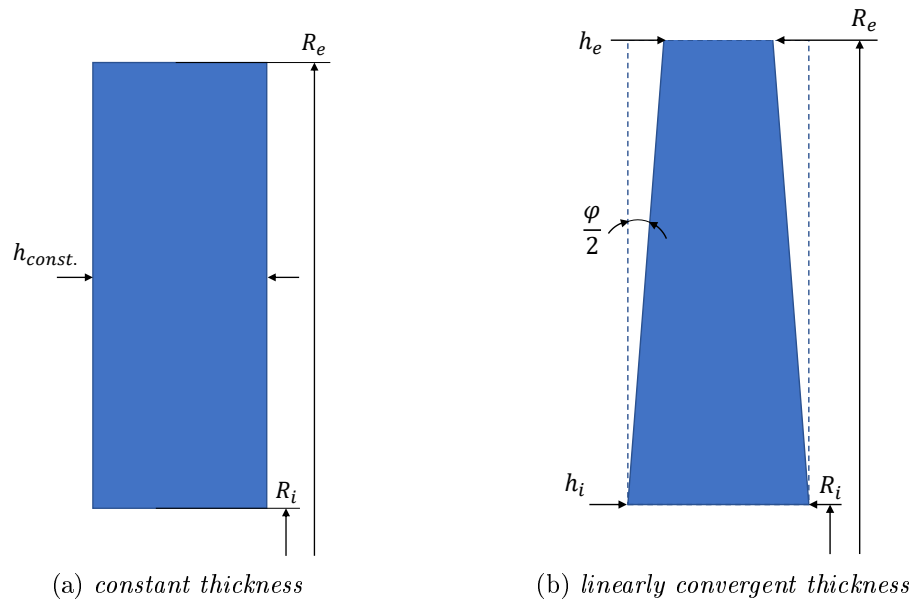


Figure 5.5: Transversal cross section of the sample disks

With the same centrifugal force, the resulting pressure at the external radius will be different in the two cases. That's because in the convergent disk  $h_e < h_i = h_{const.}$  and, following Equation 5.3.5, the external radial stress condition will be:

- **Constant-thickness disk:**  $\sigma_r(R_e) = 86.8$  MPa.
- **Convergent-thickness disk:**  $\sigma_r(R_e) = 166.8$  MPa.

Solutions provided for the two problems are obtained thanks to Grammel's method application and validated using a dedicated FEM analysis. This proves that the imple-

mented algorithm effectively works, because FEM results perfectly match Grammel's one, as it can be seen in the following plots.

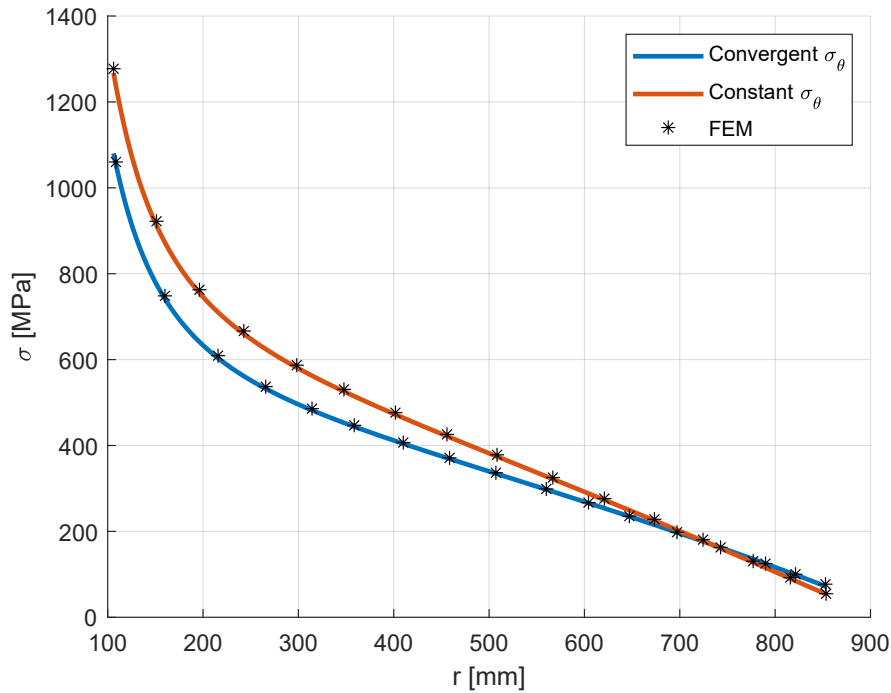


Figure 5.6: Hoop stress curves against radial length

The centrifugal acceleration is directly proportional to the distance from the center of rotation. It means that the largest the ray, the strongest should be the inertial forces to which the disk element is subjected. the idea of convergent disks is to retain this effect, reducing the mass as the disk's radius increases. In that way the overall inertial contribution of each disk element will induce a lower peak value of the hoop stress in the borehole region. In the provided example the percentage of reduction is 14,76% (see Figure 5.6). Not only hoop but also radial stresses benefit from this geometrical optimization as it can be observed in Figure 5.7. The peak value is reduced by 7,98%. The radial displacement curves are represented in Figure 5.8 and the FEM comparison shows a perfect match also in that case.

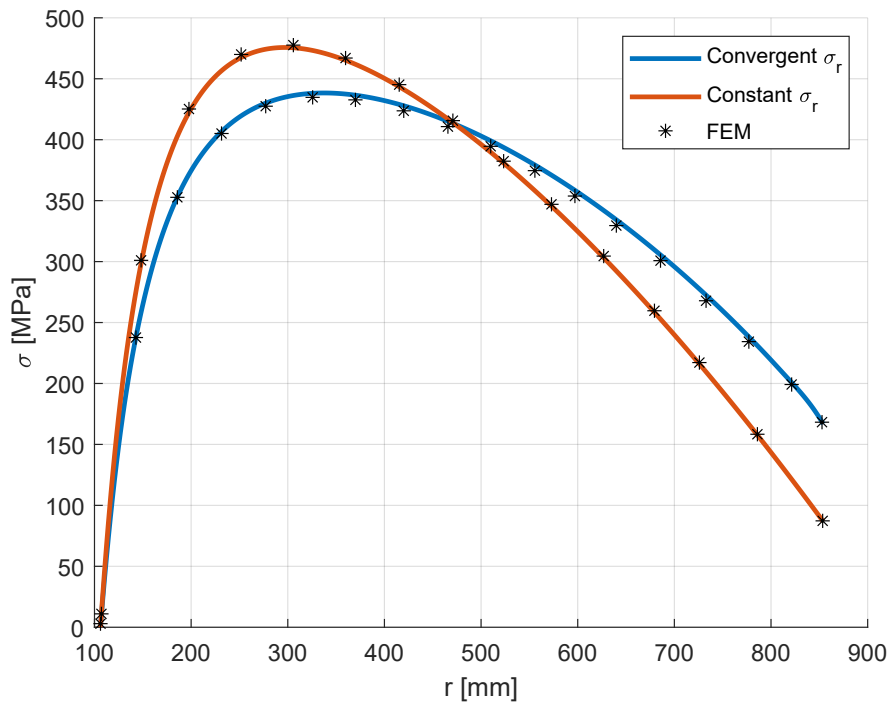


Figure 5.7: Radial stress curves against radial length

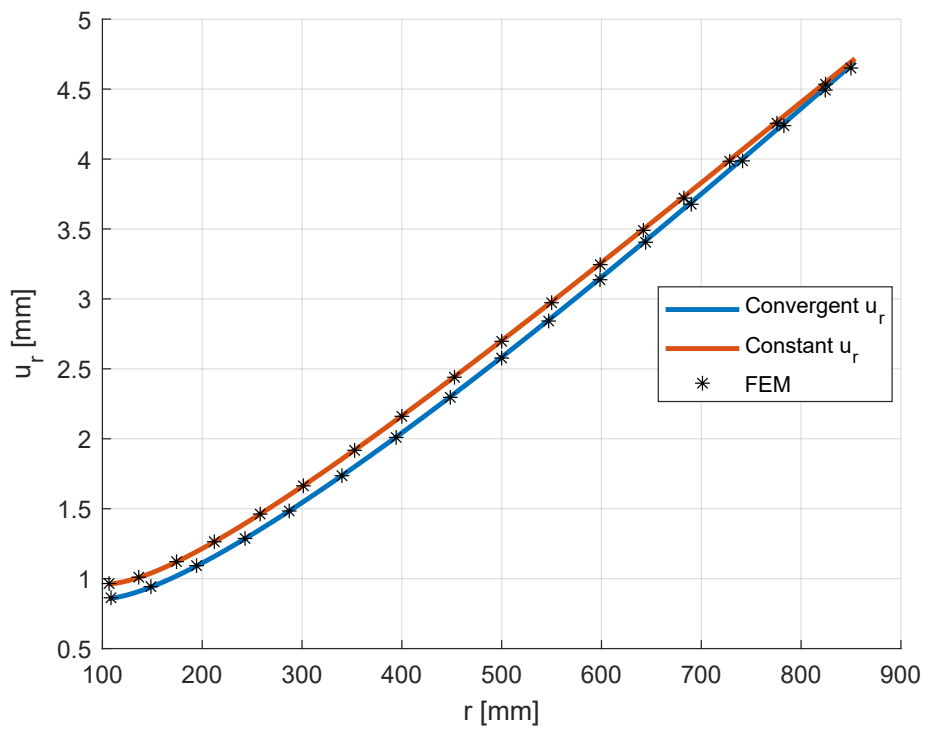


Figure 5.8: Radial displacement curves against radial length

The aim of this exercise is only to give an example of stress improvement by geometrical optimization. If properly managed, the Grammel's algorithm can be programmed to find an optimal starting shape given a design goal, which depends on different necessities and contextual limitations. Lots of factors needs to be taken into account when you are involved in turbine disk design and, among them, an important one is the thermal gradient effect. This, referred to as Secondary Load contribution, has a huge impact on the stress panorama. In order to provide sensible data linked to this phenomena, the same convergent disk is solved at environmental temperature  $\frac{\partial T}{\partial r} = 0$  and resulting stress curves are compared in Figure 5.9. The thermal contribution overloads the disk in *borehole* proximity, increasing the hoop stress peak, while releasing hoop stresses near the external diameter, because the gradient points outward. Radial stresses increase everywhere along the disk's radius.

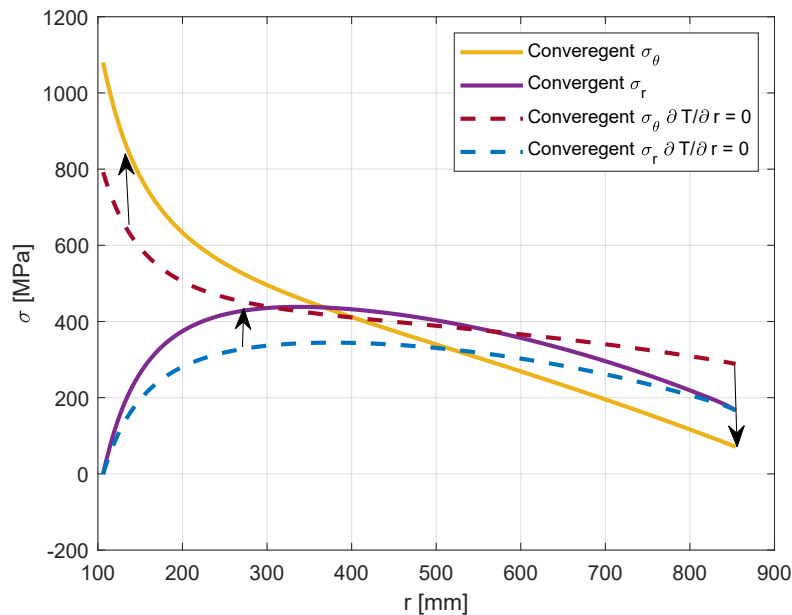


Figure 5.9: Radial and hoop stress curves against radial length

## 5.5 Limitations of the method

Reality of things is never simple. Sometimes thermal gradient can be also function of the z-coordinate and this means that at a fixed radial height temperature along the width of the disk can vary. Also pressure contact within surrounding components can be different among aftward and forward sides and aerodynamic axial load, acting on supported buckets, may not be negligible. These conditions introduce a bending moment around  $\theta$ -direction, invalidating plane stress condition hypothesis, because at least  $\tau_{rz} = \tau_{zr} \neq 0$ . On account of this, Grammel's method is no more applicable, because it would lead to an incorrect result.

Another important limitation of the method is the presence of geometrical singularities. It means when there is a sudden change of the disk's width. In order to describe this phenomenon, TW3 2D model disk of FR1500 rotor is taken as example, because of its geometrical singularity near TBH region. Grammel's discretization can be observed in Figure 5.10, where a series of concentric rigs are used to represent the variable-thickness shape with a certain accuracy. The last ring representative of the *blade root slot* region is not part of the simulation, because of break in the material along the circumferential coordinate. Its contribution is accounted in the overall centrifugal load, additionally to the blade one. Considering the lateral surface area of the disk and a rotational velocity of 3708 RPM, the external applied pressure is estimated:  $\sigma_r(R_e) = 186.16$  MPa. Like in the FEM analysis, also in Grammel's algorithm the holes for tie bolts are taken into account by orthotropic material properties assignment (see section 3.2.1 for more details). A linear thermal gradient is considered from the internal radius  $T(R_i) = 300$  °C to the external one  $T(R_e) = 400$ , which is only function of  $r$ ,  $\frac{\partial T}{\partial z} = 0$ .

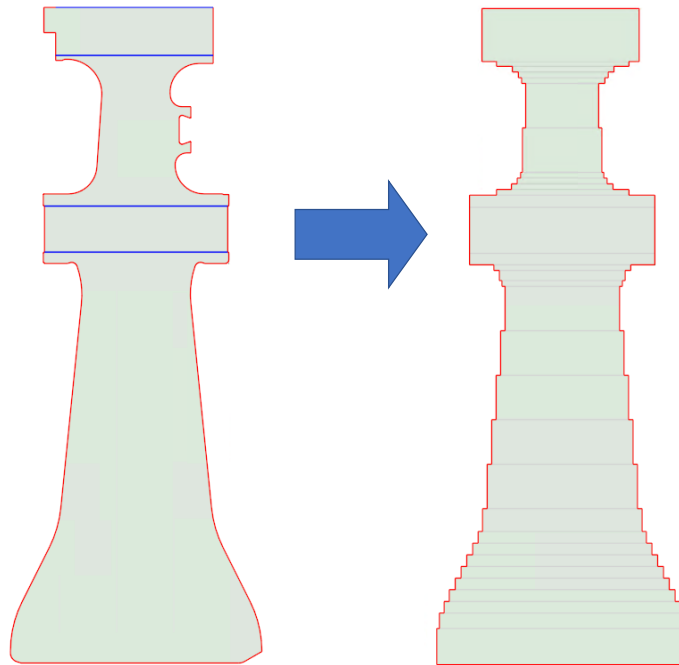


Figure 5.10: Grammel geometrical schematization of TW3 2D axisymmetric cross section model

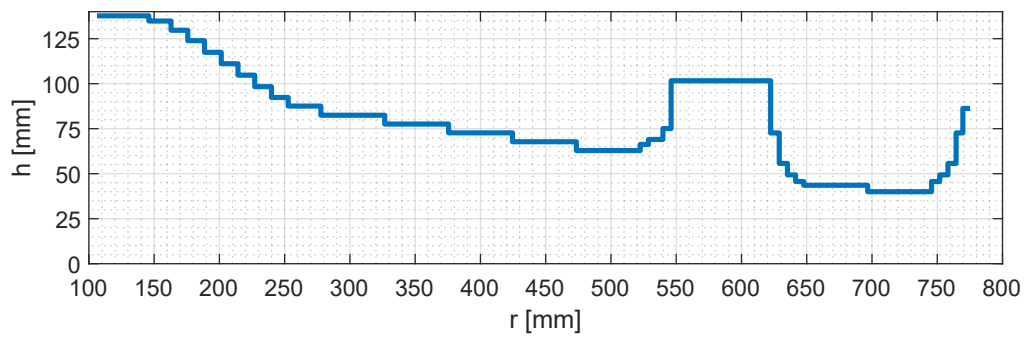


Figure 5.11: TW3 Thicknesses against radial coordinate

In Figure 5.11 is represented a chart in which half of the disk thicknesses are plotted against radial extension.

As before, the provided solutions are compared with FEM ones in order to identify the weaknesses of the method. The well-known notion that "*nature doesn't make jumps*" is evident in this case. It means that in correspondence of geometrical discontinuity radial stresses are not homogeneously distributed along the circumferential cross section. Grammel's algorithm cannot capture this kind of behaviour and, as observed in Figure 5.12, this leads to measurement biases such that radial stresses are:

- Underestimated inside the TBH region and in its surroundings;
- Overestimated just before and after the geometrical discontinuity to compensate forces acting on the relative interfaces.

As observed in Figure 5.13, despite preserving minor discrepancies, hoop stresses from Grammel's method do a better job at matching FEM results compared to their radial counterpart.

Despite differences in stress distribution, the overall contribution translates in a good approximated radial deformation. Indeed, plotted in Figure 5.14, the deformation curve is almost superposed to the FEM one.

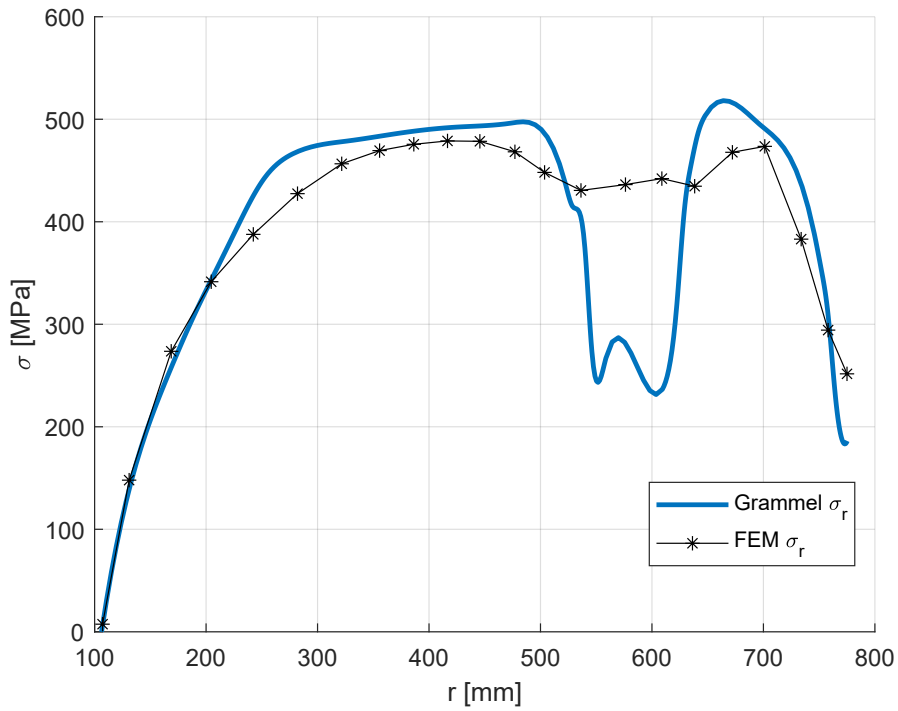


Figure 5.12: TW3 radial stress curves against radial length

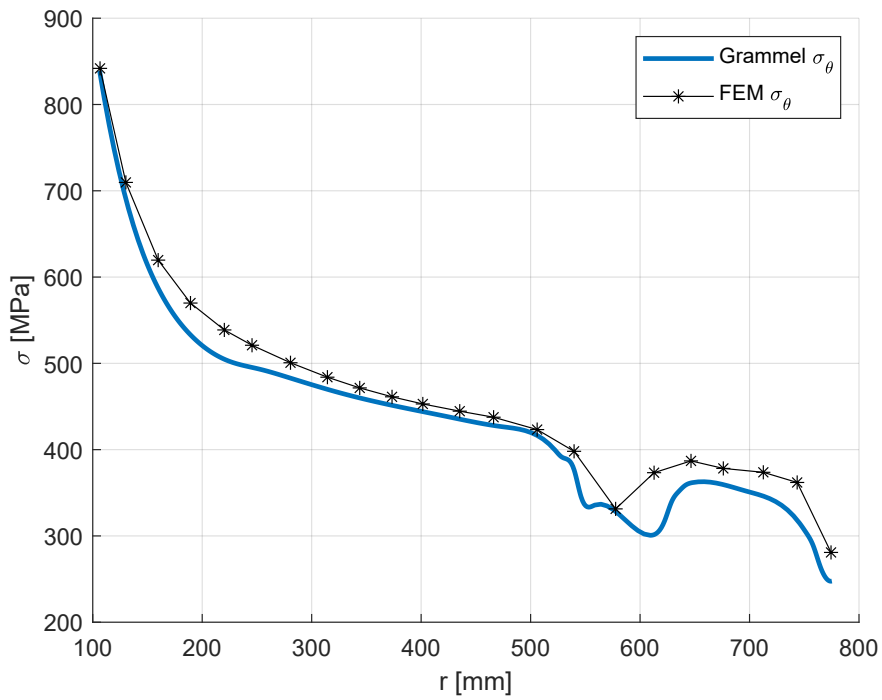


Figure 5.13: TW3 hoop stress curves against radial length

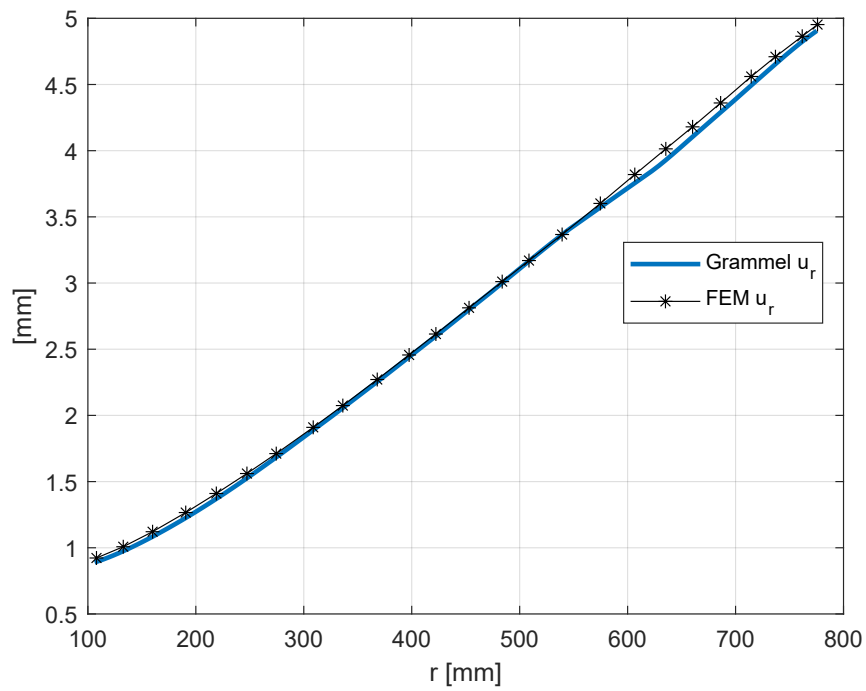


Figure 5.14: TW3 radial displacement curves against radial length

Knowing its capabilities and limitations is important to develop a conscious use of Grammel's method. It can be exploited in many application fields, providing a good calculation support, but it cannot substitute more accurate FEM software.

# Chapter 6

## Conclusions and future developments

The present work aimed to evaluate the behaviour of FR1500 rotor components under simulated operative conditions. The main research objective is to classify rotor parts according to the OEM-recommendation, by means of thermo-structural analysis as well as post processing the related outcomes. As a part of a wider life-assessment program, this research should convince the reader about its importance to provide functional solutions in a field where firms operate in a competitive environment with limited budgets. To this end, the employed methodology exploits the computational power of modern instrumentation, relying on a robust reference literature. This attitude has shown an important role behind simulations set-up. For instance, the pre-load estimation of turbine tie bolts proved to be a case study with interesting implications. It consists in an iterative procedure that involves analytical approaches and FEM simulations. That algorithm led to an efficient routine in evaluating coupling forces trends during transients. This avoids simulating bolts as physical entities, which involves many difficulties in the field of 2D steady-state and transient simulations of the assembled rotor. Also relevant to results interpretation, the mutual contribution of theoretical models and modern software programs was helpful, leading to the implementation of Grammel's method. At the end of the the dissertation it was discussed

about its applicability as a supporting calculation tool. Indeed, despite multiple limitations, the method is able to foresee the effect of thermal gradients and geometrical changes on principal stresses along disk's WEB. These are the Membrane stresses, that have been verified, according to the approach outlined in the static structural control, thus ensuring the general robustness of the entire rotor. Similarly, design criteria has proven that Primary + Secondary stresses are within the acceptance regions, so that:

- They do not overcome the  $2 \cdot S_m$  limiting curve.
- They are below the creep curve, so components do not exhibit creep failures within 144000 Factored Fired Hours.

Regarding peak stresses, despite Neuber's reduction, some critical areas have emerged such as *Blade cooling slot* and *Through Bolt Holes* (TBH), whose results are above the  $S_y$  curve, potentially bringing to localized permanent deformations. LCF analysis in these regions was able to predict that cumulated damage could be enough to induce a crack in TW1, TW2 and AFT *Stub Shaft* (AS) before the 5000 Factored Fired Starts (FFS). Such issues may pave the way for future developments and further analysis, such as:

- 3D transient analysis of TW3 sub-model to understand correct behaviour of peak stresses on TBH region, without relying on the intensification factor.
- Topological optimization of *Blade cooling slot* geometry to reduce the notch effect and so stress intensification in that area.
- More performing material adoption for fatigue endurance improvement of AS.

2D transient analysis has shown that preliminary results, obtained multiplying peak stresses by the transient coefficients, may be too conservative. TBH geometry cannot be captured by 2D model, so in this case doubts about the relevance of the results should be solved through a 3D transient simulation. On the contrary, experimental evidence on real rotors, has proven that turbine disks may experience failures in *Blade cooling slot* region. This implies that re-design could be necessary to reduce that risk and to match 5000 FFS.

Apart from the different problems that have emerged and the proposals on how to deeply analyse them, some components are believed to be promising candidates for life time extension proposal. This is especially the case of the hot compressor wheels and turbine spacers. Regarding the latter, practitioners should consider increasing the *Labyrinth seals* stiffness of SP1-2 by material addition on the relative cross section and to lower the inertial effect on the SP2-3 *Borehole* lightening the structure in that proximity. This could possibly lead to double the useful life of these components with respect to the OEM-specifications, but the implication of such changings should be carefully managed, especially from a vibration dynamic perspective.

# Annex

Here are listed the figures representing the legend for each of the remaining components of the turbine side:

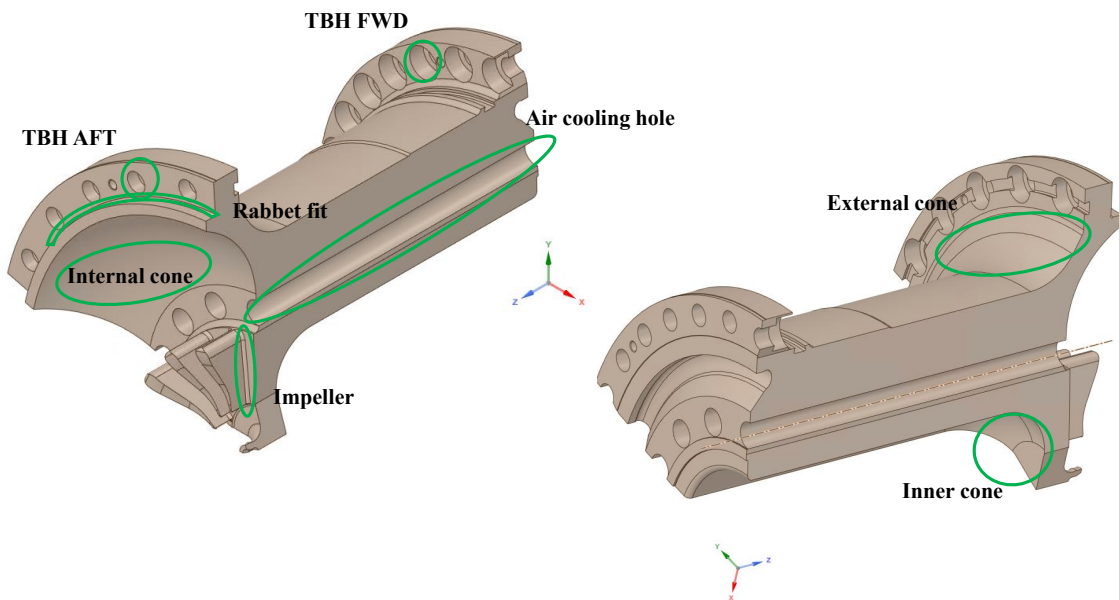


Figure 6.1: DP legend on 3D sub-model

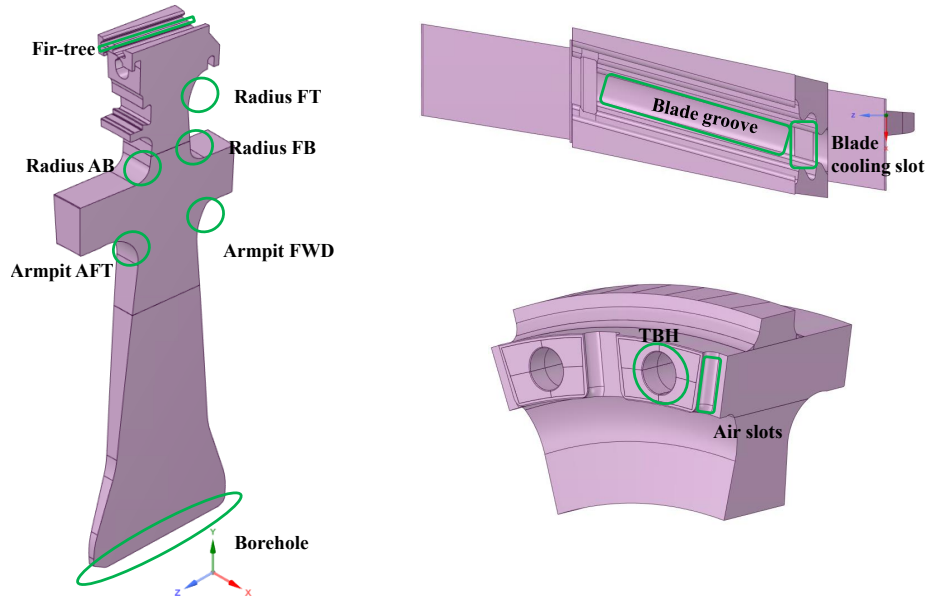


Figure 6.2: TW2 legend on 3D sub-models

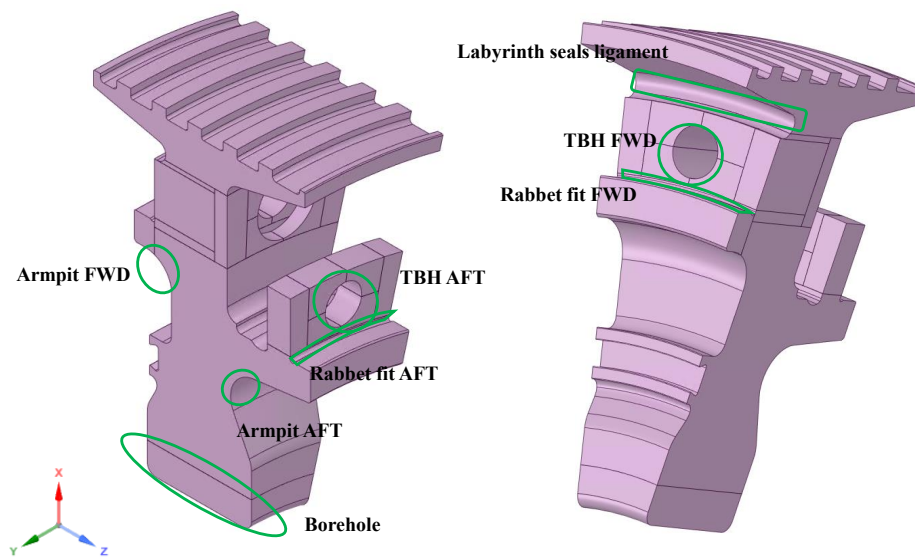


Figure 6.3: SP2-3 legend on 3D sub-model

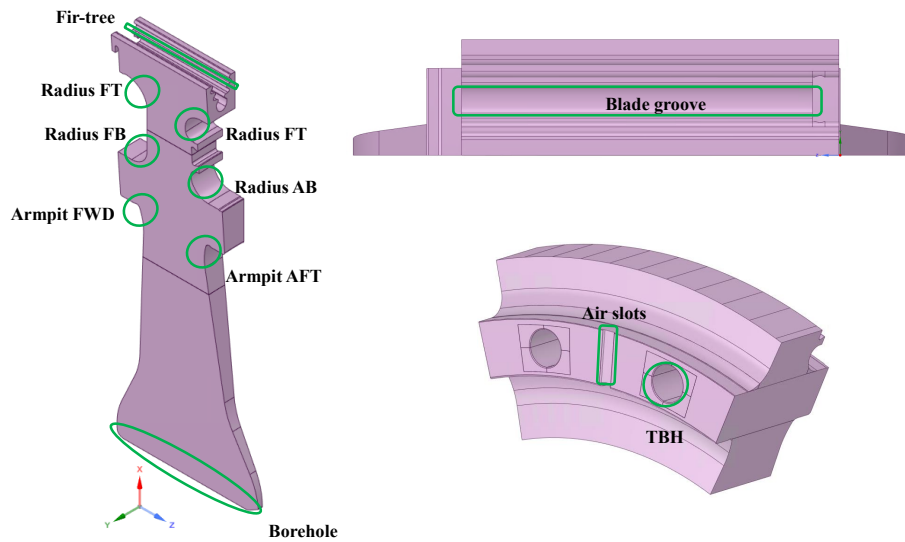


Figure 6.4: TW3 legend on 3D sub-models

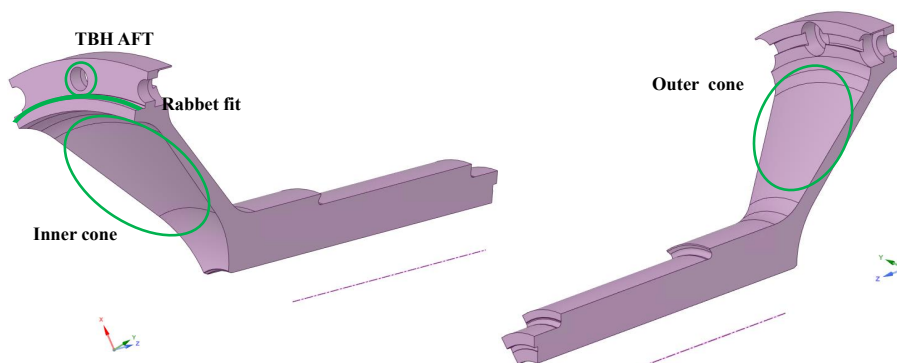


Figure 6.5: AS legend on 3D sub-model

# List of Figures

1.1	Schematic representation of the plant . . . . .	7
1.2	Thermodynamic cycle . . . . .	8
1.3	Global efficiency $\eta_g$ plotted against $\beta$ at different $T_3$ temperatures . .	10
1.4	Sketch of reference system . . . . .	11
1.5	Volume element [2] . . . . .	15
1.6	Velocity and Temperature distribution . . . . .	18
1.7	Hysteresis $\sigma - \varepsilon$ loop . . . . .	21
1.8	Manson-Basquin-Coffin log-log $\varepsilon - N_f$ plot . . . . .	21
1.9	Example of a 2D domain mesh grid . . . . .	25
2.1	FR1500 3D model and rotor section representation . . . . .	31
2.2	FR1500 section of compressor rotor assy . . . . .	32
2.3	C12 compressor wheel . . . . .	33
2.4	representation of C16 and C17 CW with cooling flow path sketch . .	34
2.5	representation of DP with cooling flow path sketch . . . . .	35
2.6	FR1500 section of turbine rotor assy . . . . .	35
2.7	TW2 whole disk and sub-model geometries . . . . .	37
2.8	Cooling scheme of turbine disks and blades . . . . .	39
2.9	SP1-2 Turbine spacer . . . . .	39

3.1	Non-axisymmetric geometrical features . . . . .	43
3.2	Point-mass sketch on turbine side . . . . .	45
3.3	TW1 example of mesh distribution . . . . .	46
3.4	TW1-SP1-2 connection example . . . . .	47
3.5	Rotor constraint and rotational speed . . . . .	48
3.6	Bolt-Part characteristic curves . . . . .	49
3.7	#1 stage bolt geometry example . . . . .	50
3.8	Pre-load algorithm calculation scheme . . . . .	50
3.9	#2 stage Tie bolt 3D model and 2D meshed cross section surface . . . . .	52
3.10	Iteration scheme . . . . .	52
3.11	bolt-part characteristic curves for each stage . . . . .	53
3.12	Bolt's lengths and total exerted coupling forces . . . . .	54
3.13	Vectors of bolt's pre-load forces . . . . .	55
3.14	Highlighted edges of components in contact with air cooling flow . . . . .	56
3.15	Dirchlet condition in air cooling channels . . . . .	58
3.16	Dirchlet condition in TW's Rim . . . . .	59
3.17	Dirchlet condition in CW's Rim . . . . .	59
3.18	Steady-state temperature distribution . . . . .	61
3.19	HvM and Max. Princ. Stress distribution . . . . .	62
3.20	Steady-state total deformation distribution . . . . .	63
3.21	Temperature and stress distribution of 2D and 3D plotted against WEB length of TW1 . . . . .	65
3.22	Temperature and stress distribution on TW1 cross section and along WEB path . . . . .	66

3.23	Temperature and stress distribution of 2D and 3D plotted against WEB length of TW2 . . . . .	67
3.24	Temperature and stress distribution of 2D and 3D plotted against WEB length of TW3 . . . . .	68
3.25	Temperature and stress distribution of 2D and 3D plotted against WEB length of SP1-2 . . . . .	68
3.26	Temperature and stress distribution of 2D and 3D plotted against WEB length of SP2-3 . . . . .	69
3.27	TW1 legend on 3D sub-models . . . . .	71
3.28	Equivalent Hencky von Mises stress distribution on TW1 . . . . .	71
3.29	Radius AB, AT and Borehole HvM stress distribution . . . . .	72
3.30	Fir tree HvM stress distribution . . . . .	73
3.31	Blade cooling slot HvM stress distribution . . . . .	74
3.32	Through Bolt Hole HvM stress distribution . . . . .	74
3.33	SP1-2 legend on 3D sub-model . . . . .	75
3.34	Equivalent Hencky von Mises stress distribution on SP1-2 . . . . .	75
3.35	TBH and Labyrinth seals HvM stress distribution . . . . .	76
3.36	Deformation shape sketch of right-end side of Labyrinth seals . . . . .	77
3.37	Neuber's rule . . . . .	80
3.38	Design criteria allowable stresses . . . . .	81
3.39	Membrane stress acceptance plot (All turbine disks) . . . . .	84
3.40	Summary table results (TW1) . . . . .	85
3.41	Primary stress acceptance plot (TW1) . . . . .	85
3.42	Primary + Secondary stress acceptance plot (TW1) . . . . .	86
3.43	Peak stress acceptance plot (TW1) . . . . .	86

3.44	Summary table results (SP1-2) . . . . .	87
3.45	Peak stress acceptance plot (SP1-2) . . . . .	87
3.46	Summary table results (all the rest) . . . . .	89
4.1	Parameters trends against time . . . . .	93
4.2	Pre-load trends for each turbine stage bolts kit . . . . .	94
4.3	Example of variable Robin boundary conditions, plotted against simulation time . . . . .	96
4.4	Example of variable Dirichlet boundary conditions, plotted against simulation time . . . . .	97
4.5	Temperature distribution of the whole rotor at different time laps . . . . .	99
4.6	Smith-Watson-Topper Fatigue curve at R.T. and 400°C as example . . . . .	101
4.7	Temperature distribution of the whole rotor at different time laps . . . . .	102
4.8	Maximum Principle stress distribution on most critical <i>Rabbit fit</i> radii . . . . .	103
4.9	<i>Rabbit fit</i> radius temperature trend on C9, C13, C14 FWD and C15 FWD . . . . .	104
4.10	<i>Rabbit fit</i> radius stress trend on C9, C13, C14 FWD and C15 FWD . . . . .	105
4.11	<i>Borehole</i> temperature trend on C1, C10, C11 FWD and C13 . . . . .	105
4.12	<i>Borehole</i> stress trend on C1, C10, C11 FWD and C13 . . . . .	106
4.13	<i>Rabbit fit</i> Max. Princ. stress and LCF prediction . . . . .	107
4.14	<i>Borehole</i> Max. Princ. stress and LCF prediction . . . . .	107
4.15	3D sub-models Max. Princ. stress results and LCF prediction . . . . .	109
4.16	2D transient <i>borehole</i> stress trends . . . . .	110
4.17	2D transient <i>armpits</i> stress trends . . . . .	111
4.18	2D transient <i>labyrinth seals</i> stress trend . . . . .	112

4.19	2D transient <i>rabbit fit</i> stress trends . . . . .	112
4.20	2D transient stress results and LCF prediction on TWs . . . . .	113
4.21	2D transient stress results and LCF prediction on SP . . . . .	113
5.1	Infinitesimal element equilibrium vector forces . . . . .	115
5.2	Infinitesimal element deformation shape . . . . .	116
5.3	Sketch of a rotating constant-thickness disk, subjected to a linear thermal gradient . . . . .	118
5.4	Disk cross section discretization in a series of N concentric rings . . . . .	119
5.5	Transversal cross section of the sample disks . . . . .	125
5.6	Hoop stress curves against radial length . . . . .	126
5.7	Radial stress curves against radial length . . . . .	127
5.8	Radial displacement curves against radial length . . . . .	127
5.9	Radial and hoop stress curves against radial length . . . . .	128
5.10	Grammel geometrical schematization of TW3 2D axisymmetric cross section model . . . . .	130
5.11	TW3 Thicknesses against radial coordinate . . . . .	130
5.12	TW3 radial stress curves against radial length . . . . .	132
5.13	TW3 hoop stress curves against radial length . . . . .	132
5.14	TW3 radial displacement curves against radial length . . . . .	133
6.1	DP legend on 3D sub-model . . . . .	137
6.2	TW2 legend on 3D sub-models . . . . .	138
6.3	SP2-3 legend on 3D sub-model . . . . .	138
6.4	TW3 legend on 3D sub-models . . . . .	139
6.5	AS legend on 3D sub-model . . . . .	139

# Bibliography

- [1] Meherwan P Boyce. *Gas turbine engineering handbook*. Elsevier, 2011.
- [2] Yunus Cengel. *Heat and mass transfer: fundamentals and applications*. McGraw-Hill Higher Education, 2014.
- [3] Canuto Claudio. *Notes of the Lecture Course NUMERICAL MODELS AND METHODS (Mechanical Engineering)*. 2019/20.
- [4] Brusa Eugenio. *Notes of Machine Design course, Bolts Section*. 2019/20.
- [5] Brusa Eugenio. *Notes of Machine Design course, Fatigue Section*. 2019/20.
- [6] R Giovanozzi. Studio delle sollecitazioni termiche in dischi conici, in dischi a spessore costante e in dischi a profilo arbitrario mediante scomposizione in tronchi parziali. *L'Aerotecnica*, 30(6):308–315, 1950.
- [7] Renato Giovanozzi. *Costruzione di macchine vol 1*. Casa editrice prof. riccardo patron, 1965.
- [8] A Ince and G Glinka. A modification of morrow and smith–watson–topper mean stress correction models. *Fatigue & Fracture of Engineering Materials & Structures*, 34(11):854–867, 2011.

- 
- [9] Scott Keller and David Day. Extending the life of f-class gas turbine rotors. In *ASME Turbo Expo 2018: Turbomachinery Technical Conference and Exposition*. American Society of Mechanical Engineers Digital Collection, 2018.
- [10] Yang Liu, Qi Yuan, Guangyu Zhu, and Pu Li. Transient analysis and design improvement of a gas turbine rotor based on thermal-mechanical method. *Shock and Vibration*, 2018, 2018.
- [11] Mauro Maccio, Adelmo Rebizzo, Laura Traversone, and Luca Bordo. Rotor components life evaluation validated by field operation data. In *Turbo Expo: Power for Land, Sea, and Air*, volume 44014, pages 539–548, 2010.
- [12] Tatjana Misic, Marina Najdanovic-Lukic, and Ljubisa Nesic. Dimensional analysis in physics and the buckingham theorem. *European Journal of Physics*, 31(4):893, 2010.
- [13] Anna Misul, Danilea. *Lecture notes of "Thermal and Hydraulic Machines" course*. 2019/20.
- [14] G Petrucci. *Lezioni di costruzione di macchine*. 2007.
- [15] Eliodoro Chiavazzo Pietro Asinari. *Selected lectures on engineering thermodynamics*. 2018/19.
- [16] KNua Smith. A stress-strain function for the fatigue of metals. *Journal of materials*, 5:767–778, 1970.
- [17] Francesco Vivio and Vincenzo Vullo. Elastic stress analysis of rotating converging conical disks subjected to thermal load and having variable density along the radius. *International Journal of Solids and Structures*, 44(24):7767–7784, 2007.